Development of Tip-enhanced Raman Spectroscopy and its Application to Heterogeneous Catalysis Research

Author: Naresh Kumar

Title: Development of Tip-enhanced Raman Spectroscopy and its Application to Heterogeneous Catalysis Research

ISBN: 978-94-9301-489-3

Printed by: Gildeprint, The Netherlands

Development of Tip-enhanced Raman Spectroscopy and its Application to Heterogeneous Catalysis Research

Ontwikkeling van Tip-verbeterde Raman Spectroscopie en de Toepassing ervan in Heterogene Katalyse Onderzoek

(*met een samenvatting in het Nederlands*)

Proefschrift

ter verkrijging van de graad van doctor aan de Universiteit Utrecht op gezag van de rector magnificus, prof. dr. H.R.B.M. Kummeling, ingevolge het besluit van het college voor promoties in het openbaar te verdedigen op maandag 26 november 2018 des middags te 4.15 uur

door

Naresh Kumar

geboren op 20 december 1982 te Panipat, India

Promotor: Prof. dr. ir. B. M. Weckhuysen

This research is supported by the National Measurement System of the UK Department of Business, Energy & Industry Strategy, a European Research Council (ERC) Advanced Grant (no. 321140) and a Gravitation Program MCEC (Multiscale Catalytic Energy Conversion) from the Netherlands Organization for Scientific Research (NWO).

"*Logic will get you from A to B. Imagination will take you everywhere*."

Albert Einstein, 1879 – 1955

Contents

Chapter 1

General Introduction

Abstract

Catalysis is at the forefront of many developments to make our society more sustainable and less dependent on fossil resources, such as coal, gas and crude oil. To make this possible, it is important to obtain detailed insights on the working principles of solid catalysts. In the past decades, many powerful characterisation techniques have been developed to investigate the reaction and deactivation mechanisms of various catalytic materials, ranging from supported metal nanoparticles to zeolites. Raman spectroscopy is one of these methods and has been seen as a complementary technique to the more generally used infrared spectroscopy. However, Raman spectroscopy suffers from a relatively low sensitivity, low spatial resolution and interference from an often intense fluorescence background. A way to counter this is to use tip-enhanced Raman spectroscopy (TERS), which is the topic of this PhD thesis. TERS combines high chemical sensitivity of surface-enhanced Raman spectroscopy with high spatial resolution of scanning probe microscopy enabling surface chemical imaging at nanometre length-scales. This Chapter introduces the fundamental principles and instrumentation of TERS and outlines the structure of the PhD thesis.

This Chapter is based on: N. Kumar, S. Mignuzzi, W. Su and D. Roy, *EPJ Tech. Instrum.*, 2015, **2**, 9; T. Hartman, C. S. Wondergem, N. Kumar, A. Berg and B. M. Weckhuysen, *J. Phys. Chem. Lett.*, 2016, **7**, 1570-1584; and N. Kumar, B. Stephanidis, R. Zenobi, A. J. Wain and D. Roy*, Nanoscale*, 2015, **7**, 7133-7137.

1.1 Heterogeneous Catalysis

Heterogeneous catalysis is the mainstay of modern chemical industry. It enables efficient chemical conversion in over 80% of all industrial processes, ranging from production of pharmaceuticals to energy generation, and contributes to over 35% of the global gross domestic product (GDP).[1] Catalysts are substances that facilitate chemical reactions without being consumed enabling industry to produce chemicals which would otherwise be uneconomic or even impossible. For a successful chemical reaction, reactants involved must collide with each other. Furthermore, the collision must be energetic enough to overcome the activation energy barrier, which is the minimum energy needed for the reaction to occur. A catalyst increases the rate of a chemical reaction by providing an alternative reaction pathway of lower activation energy as schematically illustrated in Fig. 1.1.[2]

In heterogeneous catalysis, catalysts are in a different phase than the reactants. Typically, catalysts are solid, whereas the reactants are in either gaseous or liquid phase. A catalytic reaction involves several additional steps compared to the uncatalysed reaction as shown in Fig. 1.1: (1) adsorption of reactant molecules on the catalyst surface, (2) reaction of adsorbed molecules, (3) desorption of the

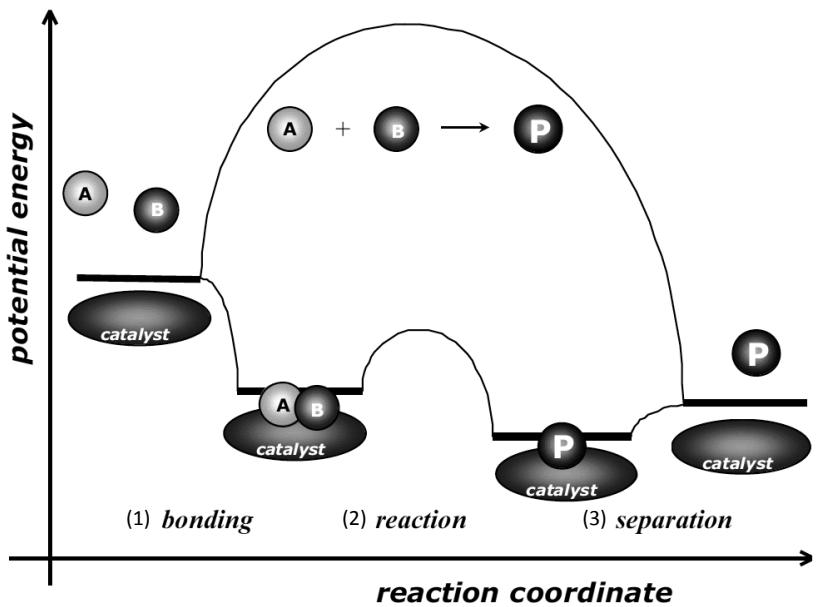

Fig. 1.1 Potential energy diagram of a typical heterogeneous catalytic reaction, A + B → P, involving gaseous reactants and products and a solid catalyst. The uncatalysed reaction has to overcome a substantial energy barrier, whereas the barriers in the catalytic route are much lower. Fig. adapted from Chorkendorff and Niemantsverdriet.[2]

molecules from the catalyst surface.[2, 3] Although a catalytic reaction pathway is more complex, it is energetically more favourable. Therefore, catalysts save energy as the reacting particles need less energy to react and lower temperatures and pressures are possible. Since the reaction happens at the active sites located on the surface of the heterogeneous catalyst, increasing its surface area increases the number of molecules that can react at the same time, thereby enhancing the rate of the reaction. Therefore, porous support mediums are employed to make the surface of the catalyst as large as possible and to further minimise the cost of the reaction because only a small amount of catalyst coating can provide a large surface area.[4]

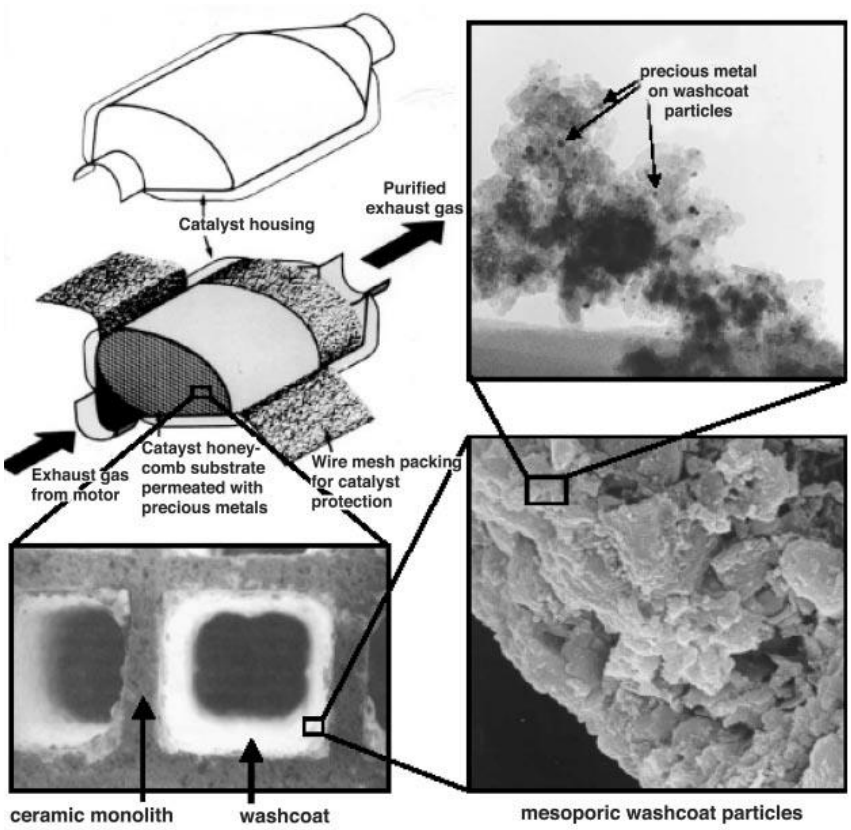

Fig. 1.2 Illustration of the placement of catalytic nanoparticles on a porous support in automotive catalytic converters. Fig. adapted from Bell.[4]

A well-known example of a porous support for the efficient dispersion of catalyst particles is the automobile catalytic converter, shown in Fig. 1.2.[4] The catalytic convertor has a honeycomb structure whose walls are covered with a thin

coating of porous alumina. The alumina washcoat is impregnated with nanoparticles of Pt, Rh, Ce, zirconia, lanthana, and baria, which perform different catalytic functions converting toxic exhaust gases to less toxic compounds through a reduction or oxidation reaction. Pt, Rh, Ce and zirconia oxidise hydrocarbons and CO and reduce NO_X; lanthana stabilises alumina against loss of surface area; whereas, baria acts as a poison for sulphur trioxide.[4]

Pressure for greener, cheaper and more sustainable chemistry in industry is driving the search for new catalysts with improved efficiency and selectivity. Rational design of catalytic materials with tailored properties relies on our ability to identify active sites at reacting surfaces in order to understand structure-performance relationships.[5, 6] However, conventional analytical techniques, such as Raman, infrared, ultraviolet-visible and fluorescence spectroscopies, often lack the required sensitivity and spatial resolution to achieve this ambitious goal.[7, 8] A prime example is Raman spectroscopy, which is a widely-used technique for *in situ* characterisation of heterogeneous catalysts and monitoring of chemical reactions,[7-9] but suffers from the above limitations. Albeit, sensitive analytical techniques like secondary ion mass spectrometry and atom probe tomography do provide valuable catalytic information with high spatial resolution, they are destructive in nature. Moreover, electron microscopy based techniques like transmission electron microscopy could be used for high-resolution investigation of catalyst samples in the gas and liquid phase, however they necessitate highly specialised apparatus and cannot be routinely used for *in situ* characterisation.[10] More recently, IR nano-spectroscopy has been used for mapping catalytic reactions on single particles, but strong IR absorption of water renders it unsuitable for monitoring reactions within an aqueous environment.[11] Consequently, *in situ* monitoring of a reaction at a single catalytically active nanoparticle remains a significant challenge.

In this PhD thesis, we have focussed on the development of a promising analytical technique called tip-enhanced Raman spectroscopy (TERS) as a novel tool for heterogeneous catalysis research. TERS combines high chemical sensitivity of surface-enhanced Raman spectroscopy (SERS) with high spatial resolution of scanning probe microscopy (SPM) enabling surface chemical imaging at nanometre length-scales. We begin with a brief discussion of the fundamental principles and instrumentation of TERS.

1.2 Tip-enhanced Raman Spectroscopy

The concept of TERS was first proposed by Wessel in 1985.[12] However, it wasn't until 2000 that TERS was experimentally demonstrated.[13-16] Since then, TERS has rapidly progressed to become an effective non-destructive SPM tool for surface chemical characterisation,[17] even opening up the opportunities to study

single molecules with sub-nm spatial resolution.[18] Over the last two decades, TERS has been used to address scientific problems in a wide range of research areas including biology,[19, 20] photovoltaics,[21, 22] catalysis,[23, 24] semiconductors,[25] single wall carbon nanotubes (SWCNT),[26] single molecule detection,[18] graphene[27-29] and other two-dimensional (2D) materials.[30, 31] Unlike electron spectroscopy and microscopy techniques, such as scanning electron microscopy (SEM), transmission electron microscopy and X-ray photoelectron spectroscopy (XPS), which require vacuum for their operation, TERS can be used in ambient as well as liquid envionments.[32-34] Although super-resolution fluorescence microscopy can be used for imaging of biological samples beyond diffraction limit, the fluorescent labels prevent observation of biomolecules in their native state.[35] However, being a label-free technique, TERS can be used to study the molecules directly, which is particularly useful for investigating chemical composition and molecular dynamics in biological samples. Consequently, application of TERS to biological samples such as pathogens,[36] lipid and cell membranes,[37] nucleic acids,[38] peptides[39] and proteins[40] has drawn a significant interest.

1.2.1 TERS Principle

Raman spectroscopy is a powerful technique for non-destructive and label-free chemical analysis under ambient conditions. However, if suffers from two major limitations: 1) low sensitivity, only 1 in 10^{10} photons is Raman scattered, and 2) diffraction limited spatial resolution, which depends on the excitation laser wavelength (λ) and numerical aperture (NA) of the objective lens according to the following Equation[41]

$$Spatial\ resolution = \frac{0.61\lambda}{NA} \tag{1.1}$$

The sensitivity and spatial resolution of Raman spectroscopy can be simultaneously improved using localised surface plasmon resonance (LSPR).[42] When A metal nanoparticle is placed in the field of an excitation laser, its conduction electrons oscillate with the frequency of the incident electromagnetic (EM) field. The coherent oscillation of conduction electrons is called localised surface plasmon (LSP), which is schematically illustrated in Fig. 1.3a. When the frequency of the excitation laser matches with the natural oscillation frequency of the conduction electrons, the oscillation amplitude of LSPs becomes extremely large due to resonance leading to a massive increase in the intensity of local EM field at the nanoparticle's surface, as shown in Fig. 1.3b.[43]

In TERS, the phenomenon of LSPR is exploited to obtain an enhanced EM field at the apex of a sharp metallic SPM tip positioned in the focal spot of an excitation laser as shown in Fig 1.3c. A combination of LSPR and lightning rod effect

(LRE) enhances the EM field at the TERS tip-apex by several orders of magnitude in a region similar to the size of the tip-apex (typically < 50 nm) as shown in the numerical simulation map of electric field enhancement at a TERS tip-apex in Fig. 1.3d.[44, 45] This intense local EM field enhances Raman signals from the molecules present in the vicinity of the tip-apex allowing TERS to overcome the diffraction limit of SERS and conventional Raman spectroscopy and provide non-destructive and label-free surface chemical imaging at the nanoscale.

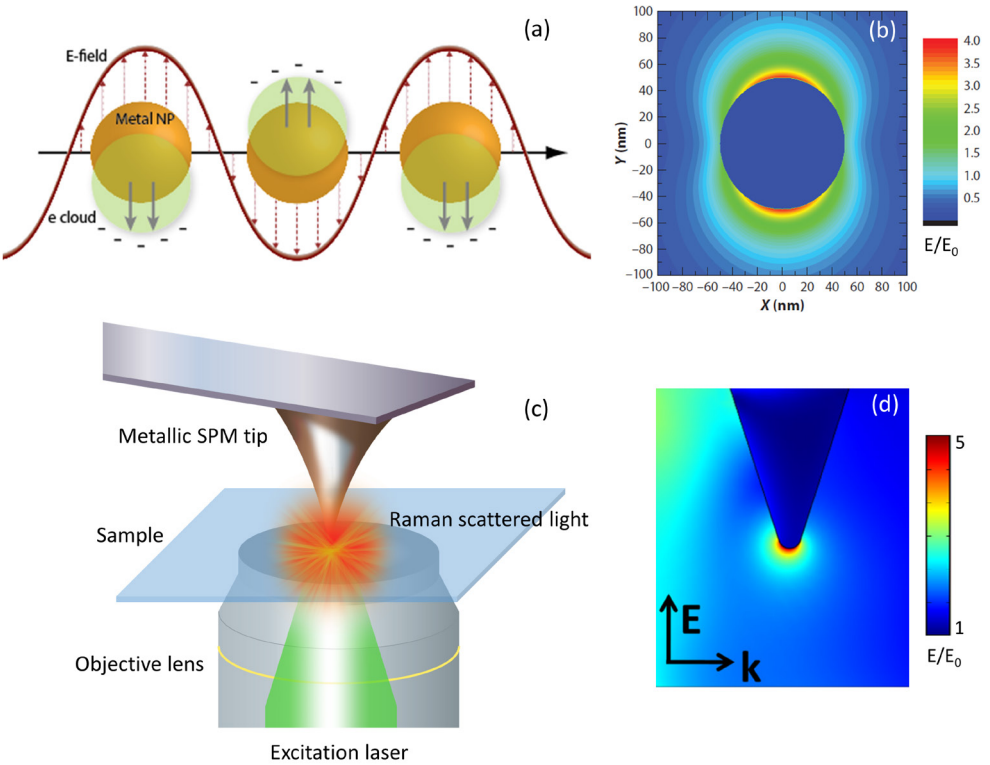

Fig. 1.3 (a) Schematic diagram showing LSP generated in metal nanoparticles *via* interaction of conduction electrons with the EM field of the excitation laser. Fig. adapted from Willets and Van Duyne.[42] (b) Simulated electric field amplitude (E) map of a 100 nm Ag sphere, irradiated with a laser of wavelength 514 nm along the Z-axis. The incident field amplitude (E_0) was set to 1. Fig. adapted from McLellan *et al.*[43] (c) Schematic diagram illustrating the principle of TERS. A metallic SPM tip is placed in the focal spot of an excitation laser. A combination of LSPR between the metallic tip-apex and laser-photons and LRE enhances the local EM field resulting in the enhancement of Raman signal from the analyte molecules in the immediate vicinity of the tip-apex. (d) Simulated electric field amplitude map of a Ag TERS tip irradiated with a laser of wavelength 532 nm with electric field parallel to the tip-axis (k indicates the wave vector of the excitation laser). Tip radius: 15 nm. This map is calculated using COMSOL Multiphysics®.

1.2.2 Signal Enhancement in TERS

The high chemical sensitivity and spatial resolution of TERS mainly result from the EM enhancement[46] as discussed in the previous section, although signal enhancement due to chemical interaction of a TERS tip with the sample has also been reported.[47] The observed EM enhancement at the tip-apex arises from a combination of LSPR and LRE resulting in a locally confined and enhanced electric field,[48] as shown in Fig. 1.3. The LSP wavelength of a TERS tip can be tuned by changing the material, radius or roughness of the tip-apex, and can be matched with the excitation laser wavelength. At resonance, the intensity of observed electrical field at the tip-apex is several orders of magnitude higher compared to off-resonance. Although LSPR has been observed for many metal nanoparticles, only Ag and Au are resonant with lasers in the visible light regime. Generally, LSP wavelength of a Ag TERS tip falls in the blue and green light region, whereas for a Au TERS tip, it falls in the yellow and red light region, as shown in Fig. 1.4.[49] LSP wavelength also depends on the radius of the tip-apex. For example, for a Ag tip with < 10 nm radius, the LSP wavelength may be shifted to the ultraviolet (UV) region. Such TERS tips could potentially be used to conduct UV-TERS with a lower background signal from the substrate due to the low penetration depth of UV photons.[50]

In the near-field (plasmonically enhanced EM field at the TERS tip-apex), the intensity of Raman signal from analyte molecules is proportional to the fourth power of the local electric field.[51] Hence, for near-field and far-field (EM field in the focal spot of an excitation laser with the TERS tip retracted from the sample) intensity E_{NF} and E_{FF}, respectively, plasmonic enhancement of a Raman signal (ρ) is proportional to[46, 52]

$$\rho \propto \left(\frac{E_{NF}}{E_{FF}} \right)^4 \tag{1.2}$$

Enhancement factor (EF) of a TERS signal is defined as[53]

$$EF = \left(\frac{I_{TERS}}{I_{Far-field}} - 1 \right) \frac{V_{FF}}{V_{NF}} \tag{1.3}$$

where, I_{TERS} and $I_{Far-field}$ are the intensity of a Raman band measured with the TERS tip in contact and retracted from the sample, respectively; V_{NF} and V_{FF} are the probe volumes contributing to the near-field and far-field Raman signals,

respectively. For a thin film sample, V_{NF} and V_{FF} could be approximated by A_{NF} and A_{FF}, which are the areas of the sample contributing to the near-field and far-field Raman signals, respectively. Therefore, for thin film samples, the EF can be estimated using the following Equation

$$EF = \left(\frac{I_{TERS}}{I_{Far-field}} - 1 \right) \frac{A_{FF}}{A_{NF}} \tag{1.4}$$

In Equation 1.4, A_{NF} and A_{FF} could be estimated from the geometric diameter of the TERS tip-apex and size of the diffraction-limited excitation laser spot, respectively. However, for thick samples, enhancement of TERS signals is estimated more conveniently using "contrast", which is defined as[53]

$$Contrast = \frac{I_{TERS}}{I_{Far-field}} - 1 \tag{1.5}$$

Usually, contrast provides a better indication of the capability of a TERS probe for high-resolution Raman imaging compared to the EF.

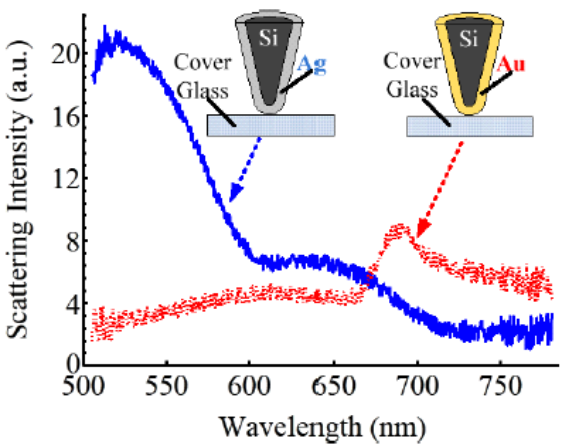

Fig. 1.4 Spectra showing scattering of visible light from Ag and Au coated Si atomic force microscopy (AFM) tips. Fig. is adapted from Zhang *et al.*[49]

1.2.3 TERS Experimental Set-ups

Optical geometries of a TERS set-up can be classified into three types: (a) bottom (transmission mode), (b) side, and (c) top illumination, as shown schematically in Fig. 1.5. Side and top illumination are also referred to as reflection modes. In bottom illumination (Fig. 1.5a), a laser beam is focussed onto the sample through a transparent substrate using a high NA (typically > 1) objective lens.[53] In this geometry, a radially polarised beam provides a tighter focal spot along with a stronger longitudinal electric field along the tip-shaft compared to a linearly polarised beam. Theoretical calculations and experimental results have shown that the EM enhancement using the radially polarised laser beam can be > 4× stronger compared to a linearly polarised beam.[54, 55] Although engineering implementation of the transmission TERS mode set-up is relatively simpler, it is limited by the essential requirement of a transparent sample and substrate.

In the side illumination set-up (Fig. 1.5b), a linearly polarised beam (p-polarisation)[18] is focussed onto the tip-apex from the side of the tip *via* a long working distance objective lens. Because the laser polarisation can be aligned with the TERS tip axis, a strong EM enhancement at the tip-apex could be achieved even with a relatively low NA objective lens. In the top illumination set-up (Fig. 1.5c), the laser is focussed from the top onto the end of a tilted scanning tunnelling microscopy (STM) tip[56] or a nose type AFM tip.[57] Top illumination TERS set-up is comparatively easier to implement compared to the side illumination. The side and top illumination based reflection mode TERS set-ups are especially beneficial for the nanoscale chemical characterisation of opaque samples such as nano-electronic devices, where substrates are generally non-transparent.

Zhang *et al.*[58] have demonstrated a different type of reflection mode set-up in which the excitation laser is focussed onto the apex of a TERS tip *via* a parabolic mirror. The parabolic mirror based reflection mode set-up has the advantages of being free from chromatic aberration, having a high NA (≈1) and a tight laser focus.

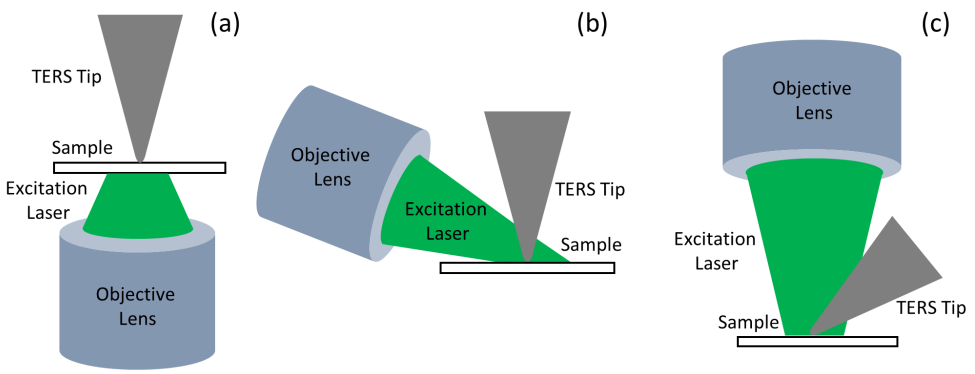

Fig. 1.5 Schematic diagrams of the most commonly used TERS configurations. (a) Bottom illumination set-up. (b) Side illumination set-up. (c) Top illumination set-up.

1.2.4 TERS Probes

1.2.4.1 Metal Coating

Nearly two decades ago, Zenobi and co-workers used Ag coated Si AFM tips to conduct the first TERS measurements.[13] Since then, Ag and Au coated TERS tips prepared using thermal evaporation under low pressure (10^{-5} - 10^{-6} mbar) in a vacuum chamber as shown in Fig. 1.6a have been commonly used for performing TERS measurements. However, the yield of TERS tips showing large signal enhancement is usually quite low due to the random nucleation and growth process of metal nanoparticles around the tip-apex as evident from the SEM images of a typical Ag coated TERS tip shown in Fig. 1.6b. The issue of low yield has been addressed by modifying the refractive index of an AFM tip prior to metal deposition, which improves the plasmon resonance characteristics of the TERS tips. For example, Yeo *et al.* prepared TERS tips by applying a thin SiO_2, SiO_x or AlF_3 film to an AFM tip prior to Ag deposition[59] and obtained a yield close to 100 % with high EF. Furthermore, Taguchi *et al.* also obtained almost 100 % yield of TERS tips by oxidising the Si AFM tips to a thin layer of SiO_2 (≈ 300 nm) before Ag deposition.[60]

However, despite the improvement in the yield of Ag coated TERS tips, TERS measurements remain challenging due to the limited lifetime of such probes. TERS probes undergo rapid degradation in ambient environment typically losing their plasmonic enhancement within a few hours.[32, 61-63] Moreover, the degradation mechanism of the TERS tips has been poorly understood precluding development of effective solutions to address this problem. Furthermore, metal coated TERS probes undergo rapid delamination when exposed to a liquid envrionment.[33] Because of the instability of TERS tips, TERS experiments in liquids have been mostly restricted to point spectroscopy measurements[33, 64-71] and nanoscale 2D chemical mapping in a liquid environment using TERS has not been possible.[72]

1.2.4.2 Electrochemical Etching

Electrochemical etching methods have been implemented by different research groups to obtain sharp and smooth metal TERS tips.[73-75] For example, electrochemical etching of a Au wire could be performed using the set-up shown in Fig. 1.6c, where the Au wire acts as the anode and a second electrode (Au or Pt) acts as the cathode. Both electrodes are immersed in an etchant and current is passed to etch away the Au wire until the meniscus drops off. Williams and Roy[73, 74] used HCl as the etchant for etching Au wires according to the following Equations

$$Au + 4Cl^- \rightarrow AuCl_4^- + 3e^- \quad (1.6)$$

$$Au + 2Cl^- \rightarrow AuCl_2^- + e^- \quad (1.7)$$

$$AuCl_2^- + 2Cl^- \rightarrow AuCl_4^- + 2e^- \quad (1.8)$$

Sharp Au TERS tips with < 10 nm radius (Fig. 1.6d) could be reproducibility prepared using this method.

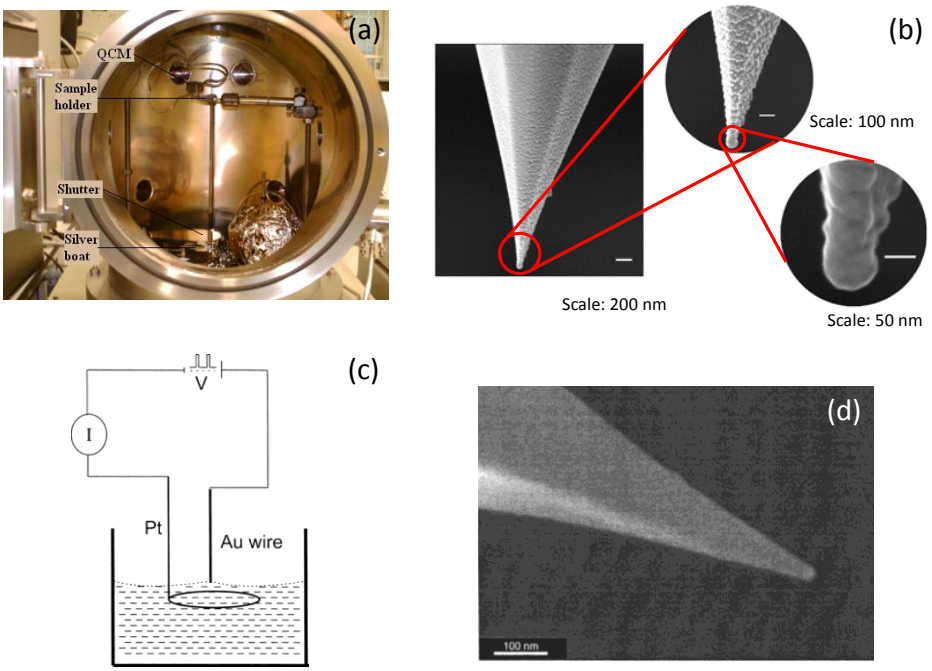

Fig. 1.6. (a) Picture of a typical vacuum chamber for thermal evaporation of Ag or Au on commercial AFM tips to prepare TERS probes. (b) SEM images of a typical Ag coated TERS tip prepared using the thermal evaporation set-up shown in Fig. 1.6a. (c) Schematic diagram of the set-up to prepare Au TERS tips *via* electrochemical etching. (d) SEM image of an etched Au TERS tip prepared using the set-up shown in Fig. 1.6c. Fig. 1.6c and d are adapted from William and Roy.[73]

1.2.5 SPM Feedback

TERS systems can be classified into three types according to the feedback mechanism used to keep TERS tip in contact with the sample surface: contact/tapping mode AFM, shear force AFM and STM, shown schematically in Fig. 1.7a - c, respectively. Since AFM is relatively more versatile in terms of usage on both non-conductive and conductive samples, many home-made and commercial TERS systems have adopted the AFM based TERS set-up, first reported by Stockle *et al.*[13] In AFM, a constant force of interaction is maintained between a cantilever and the sample using a feedback loop. Any deflection of the cantilever due to

changes in the force of interaction is measured using a semiconductor laser, which is reflected from the back of the cantilever onto a quadruple photodetector, as shown in Fig. 1.7a. The Ag or Au coated AFM tips can typically provide a spatial resolution of ≈ 20 nm in the TERS images.[27, 76] However, rapid oxidation of Ag in ambient air makes the tips lose their enhancing capability within a few hours. Although contact mode is the most commonly used AFM feedback in TERS so far, some groups have also reported strong plasmonic enhancement of Raman signals using tapping mode AFM feedback.[77-79] In shear force mode AFM feedback, a metal tip is mounted onto the prong of a quartz tuning fork as shown in Fig. 1.7b. TERS measurements are conducted by positioning the tip at the centre of the laser focus, and accurately controlling the tip-sample distance using shear force as the feedback loop parameter.[80, 81] In case of STM-TERS, the tip-sample distance is controlled *via* a feedback loop using the tunnelling current between the tip and sample, as shown schematically in Fig. 1.7c. The substrate needs to be conductive; consequently, only

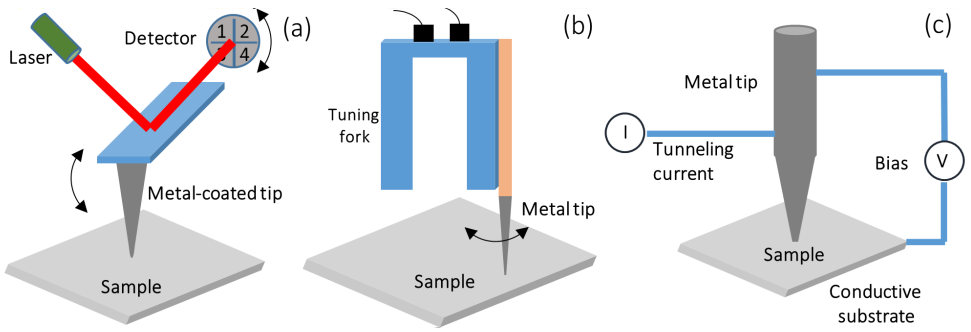

Fig. 1.7 Schematic diagrams of SPM feedback mechanisms used in TERS. (a) Contact/tapping mode AFM feedback mechanism. (b) Shear force mode AFM feedback mechanism. (c) STM feedback mechanism.

reflection mode geometry is viable in an STM-TERS system. TERS maps with ultrahigh spatial resolution of 0.5 nm and 1.7 nm have been reported using STM-TERS set-ups.[18, 82]

1.3 Applications of TERS in Catalysis

In order to directly correlate catalyst morphology with activity, we need to monitor and map catalytic activity on single catalyst particles. Analytical techniques with a very high sensitivity and spatial resolution are required to reach this goal.[5] A direct method to correlate catalyst structure to activity is by combining high chemical sensitivity of SERS with nanoscale spatial resolution of SPM. To showcase this,

catalytic activity of Ag nanocubes in rhodamine 6G degradation was linked to their distribution, which demonstrated the potential of a combined AFM-SERS approach.[83] However, the diffraction limited spatial resolution of SERS (typically 200 nm - 300 nm) is not overcome simply by combining SERS with SPM.

The spatial resolution Raman mapping can be significantly improved using TERS.[84, 85] Compared to SERS, where hot spots are randomly distributed over the entire substrate, EM enhancement in TERS occurs only at a single point at the TERS tip-apex, which can be scanned over a surface using sensitive SPM feedback described above to obtain a nanoscale map of surface chemistry and catalytic activity simultaneously with topography. The potential of TERS for catalysis research was first demonstrated by Domke and Pettinger,[86] who studied the organometallic catalyst cobalt meso-tetraphenylporphyrin (CoTPP) on Au (111) substrate using STM-TERS. From TERS measurements, the authors could spectroscopically discriminate between axially-complexed and ligand-free CoTPP regions on the Ag substrate and identify chemical species complexed with CoTPP. TERS spectra from well-ordered CoTPP regions identified in the STM topography images showed vibrational bands characteristic of linker-modified CoTPP sandwiched between two Au layers. Whereas, TERS spectra from the disordered regions showed vibrational features of CoTPP axially complexed with CO and NO species formed by catalytic reduction of CO_2 and NO_2 from ambient air. This study showed that TERS could be successfully used to correlate structure with catalytic activity in heterogeneous catalysis.

The first *in situ* TERS study in catalysis was carried out by Weckhuysen and Deckert *et al.*[23] using plasmon-driven photo-catalytic reaction, *p*-nitrothiophenol (pNTP) → *p,p'*-dimercaptoazobenzene (DMAB), as a showcase. This reaction was triggered using a 532 nm laser and monitored using a 633 nm laser. Time-series TERS spectra measured before and after the reaction at the tip-apex clearly showed Raman bands associated with pNTP decrease and DMAB increase in intensity over time. This demonstrated the capability of TERS to monitor reactions on a single catalytic particle (present at the TERS tip-apex) over time. Not much later, Xu *et al.* performed a similar experiment using high vacuum (HV) STM-TERS to demonstrate that pNTP → DMAB photocatalytic reaction is driven by "hot electrons" produced during surface plasmon resonance.[87] The authors showed that the reaction can be controlled by plasmon intensity, which depends on laser power or the tip-substrate distance. An additional report using HV STM-TERS showed that the reaction was indeed the result of the plasmon resonance in the nanogap between a Au tip and a Ag substrate and any thermal effects could be neglected.[88]

Potential of TERS to map activity on a heterogeneous catalyst substrate was realised by Kumar *et al.* using AFM-TERS.[24] Plasmon driven photocatalytic dimerisation of *p*-aminothiophenol (pATP) → DMAB was used as the model reaction

to demonstrate spatially resolved imaging of catalytic activity over a heterogeneous catalyst substrate using TERS. The authors first showed mapping of pATP → DMAB at a single point of contact of the Ag coated TERS tip with a reactant substrate. Since both the Ag particles and the Ag coated TERS tip were catalytically active in the reaction, the tip was made inert by applying a 3 nm - 5 nm thick Al_2O_3 layer while preserving its plasmonic enhancement. Using the alumina-protected TERS tip, the authors showed mapping of catalytically active sites on a heterogeneous Ag substrate with ≈ 20 nm spatial resolution as shown in Fig. 1.8.

However, despite the progress made in the application of TERS to catalysis research, 2D nanoscale mapping of a catalytic reaction in a liquid environment using TERS has not been achieved to date primarily due to the limitations of chemical reactivity,[23, 89] short lifetime[32, 61-63] and/or instability of TERS probes in a liquid environment.[33, 34] Furthermore, the application of plasmon-enhanced optical spectroscopy to study a real life catalyst has not been demonstrated yet.

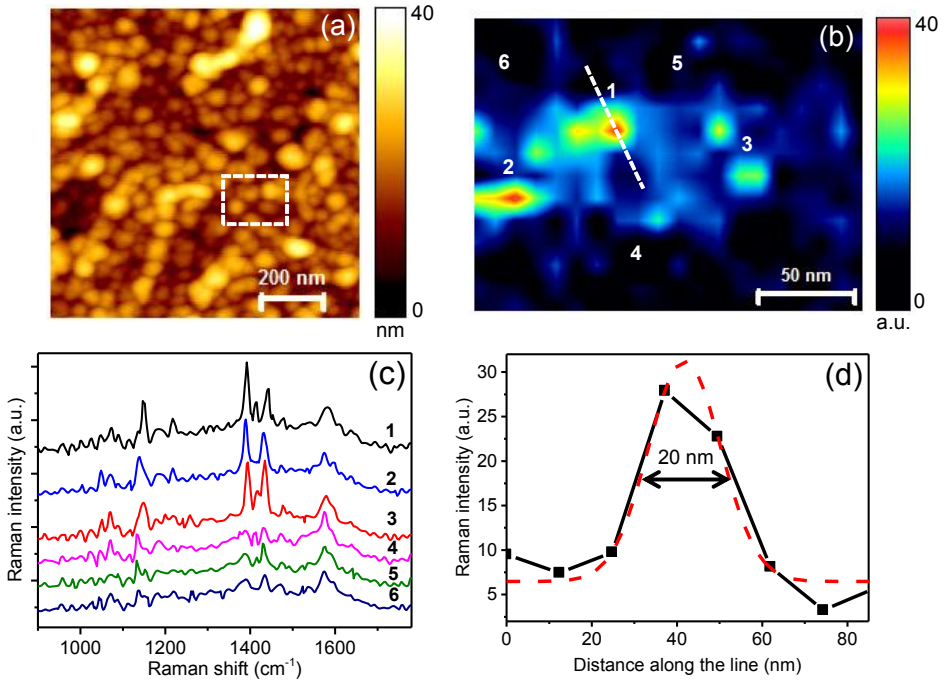

Fig. 1.8 (a) AFM topography image of a heterogeneous Ag catalyst substrate. (b) TERS map of pATP → DMAB showing signal intensity of DMAB Raman band at 1142 cm^{-1}, in the area marked using dashed rectangle in Fig. 1.8a. (c) TERS spectra measured at the positions marked in Fig. 1.8b. DMAB bands at 1142 cm^{-1}, 1390 cm^{-1} and 1437 cm^{-1} are clearly observed in the TERS spectra from positions 1-3, whereas they are absent in the spectra from positions 4-6. (d) Intensity profile along the dotted line marked in Fig. 1.8b. Spatial resolution of the TERS map is estimated from the full width at half maximum (FWHM) of a fitted Gaussian curve (red) to be ≈ 20 nm.[24]

1.4 Scope of This PhD Thesis

The goals of this PhD thesis have been two-fold: 1) development of TERS and 2) application of TERS to heterogeneous catalysis research. Consequently, the thesis is organised in two parts. In part 1, Chapters 2 and 3 primarily deal with the further understanding and development of TERS as a robust analytical tool for heterogeneous catalysis research. In part 2, Chapters 4 and 5 demonstrate the application of TERS and tip-enhanced fluorescence (TEFL) microscopy to heterogeneous catalysis research using case studies of two different catalytic systems.

Chapter 2 addresses the problem of rapid degradation of TERS probes in ambient environment, which severely prohibits the success of many TERS experiments. A systematic time series investigation of the plasmonic degradation of Ag coated TERS probes is carried out under different environmental conditions. A significant improvement in the plasmonic lifetime of TERS probes, from a few hours to a few months, is demonstrated under a low oxygen (< 1 ppm) and a low moisture (< 1 ppm) environment. Rapid plasmonic degradation of Ag coated TERS probes is correlated to surface oxide formation using XPS measurements on Ag nanoparticles. Based on the results of the study, practical strategies are proposed for the effective use and storage of TERS probes to extend their plasmonic lifetime.

Chapter 3 addresses the problem of lack of stability of TERS probes in a liquid environment, which to date has precluded nanoscale resolution chemical imaging in a liquid environment using TERS. Plasmonically active TERS probes with a multilayer metal coating structure with high stability within a liquid environment are developed. Using these novel TERS probes, successful TERS measurements are carried out in air and water environments in both gap mode and non-gap mode TERS configurations. Plasmonic enhancement of TERS signals is compared in air and water environments for both TERS configurations and in both cases the plasmonic enhancement is found to decrease in water. To understand the attenuation of TERS enhancement in water, numerical simulations are performed, which reveal a negative correlation between the electric field enhancement at the TERS probe-apex and the refractive index of the surrounding medium. Finally, chemical imaging with a nanoscale spatial resolution is demonstrated in an aqueous environment using TERS for the first time by employing SWCNTs as a model sample.

Chapter 4 addresses the problems of chemical inertness and durability of TERS probes for studying catalytic reactions in liquid phase. Novel TERS probes protected using an ultrathin layer of zirconia are developed, which extend the lifetime of TERS probes by more than 850× under ambient conditions together with a drastic improvement of their stability inside a liquid environment. Furthermore, zirconia coating renders the TERS probes chemically inert for the investigation of catalytic

reactions at the nanoscale. Using novel zirconia-protected TERS probes, spatially resolved characterisation of a photocatalytic reaction on a heterogeneous catalyst substrate is demonstrated within an aqueous environment employing plasmon-catalysed oxidation of pATP → DMAB as a model reaction. The reaction products are mapped *in situ* with a nanoscale spatial resolution. This work paves the way for using AFM-TERS for non-destructive, label-free and nanoscale chemical characterisation on a wide range of samples in both air and liquid environments.

Chapter 5 introduces TEFL microscopy as a new tool for catalysis research using a real-life fluid catalytic cracking (FCC) catalyst as a showcase. Sectioning of the industrially used multi-component FCC particles into thin layers is carried out together with selective staining of Brønsted acidity, which enables high-resolution TEFL mapping of different regions. Hyperspectral information gained *via* TEFL microscopy reveals a hierarchical distribution of Brønsted acidity within individual zeolite domains in different regions of a single FCC catalyst particle. Comparison of TEFL measurements from different FCC particles show a significant intra- and inter-particle heterogeneities in zeolite domain size and activity.

The PhD thesis ends with concluding remarks and future outlook on further development of TERS for application to heterogeneous catalysis research.

References

1. J. Hagen, *Industrial Catalysis: A Practical Approach, 2nd Ed.*, Wiley-VCH, Weinheim, 2015.
2. I. Chorkendorff and J. W. Niemantsverdriet, *Concepts of Modern Catalysis and Kinetics*, Wiley-VCH, Weinheim, 2017.
3. N. Mizuno and M. Misono, *Chem. Rev.*, 1998, **98**, 199-218.
4. A. T. Bell, *Science*, 2003, **299**, 1688-1691.
5. I. L. C. Buurmans and B. M. Weckhuysen, *Nat. Chem.*, 2012, **4**, 873-886.
6. G. Rothenberg, *Catalysis: Concepts and Green Applications, 2nd Ed.*, Wiley-VCH, Weinheim, 2017.
7. B. M. Weckhuysen, *In-situ Spectroscopy of Catalysts*, American Scientific Publishers, Stevenson Ranch, 2004.
8. G. Mestl, *J. Mol. Catal. A-Chem.*, 2000, **158**, 45-65.
9. B. M. Weckhuysen, *Chem. Commun.*, 2002, **2**, 97-110.
10. N. De Jonge and F. M. Ross, *Nat. Nanotechnol.*, 2011, **6**, 695-704.
11. C.-Y. Wu, W. J. Wolf, Y. Levartovsky, H. A. Bechtel, M. C. Martin, F. D. Toste and E. Gross, *Nature*, 2017, **541**, 511-515.
12. J. Wessel, *J. Opt. Soc. Am. B*, 1985, **2**, 1538-1541.
13. R. M. Stockle, Y. D. Suh, V. Deckert and R. Zenobi, *Chem. Phys. Lett.*, 2000, **318**, 131-136.
14. N. Hayazawa, Y. Inouye, Z. Sekkat and S. Kawata, *Opt. Commun.*, 2000, **183**, 333-336.
15. M. S. Anderson, *Appl. Phys. Lett.*, 2000, **76**, 3130-3132.
16. B. Pettinger, G. Picardi, R. Schuster and G. Ertl, *Electrochemistry*, 2000, **68**, 942-949.
17. C. Blum, L. Opilik, J. M. Atkin, K. Braun, S. B. Kammer, V. Kravtsov, N. Kumar, S. Lemeshko, J. F. Li, K. Luszcz, T. Maleki, A. J. Meixner, S. Minne, M. B. Raschke, B. Ren, J. Rogalski, D. Roy, B. Stephanidis, X. Wang, D. Zhang, J. H. Zhong and R. Zenobi, *J. Raman Spectrosc.*, 2014, **45**, 22-31.
18. R. Zhang, Y. Zhang, Z. C. Dong, S. Jiang, C. Zhang, L. G. Chen, L. Zhang, Y. Liao, J. Aizpurua, Y. Luo, J. L. Yang and J. G. Hou, *Nature*, 2013, **498**, 82-86.

19. S. Najjar, D. Talaga, L. Schue, Y. Coffinier, S. Szunerits, R. Boukherroub, L. Servant, V. Rodriguez and S. Bonhommeau, *J. Phys. Chem. C*, 2014, **118**, 1174-1181.
20. N. Kumar, M. M. Drozdz, H. Jiang, D. M. Santos and D. J. Vaux, *Chem. Commun.*, 2017, **53**, 2451-2454.
21. X. Wang, D. Zhang, K. Braun, H. J. Egelhaaf, C. J. Brabec and A. J. Meixner, *Adv. Funct. Mater.*, 2010, **20**, 492-499.
22. N. Kumar, A. Zoladek-Lemanczyk, A. A. Guilbert, W. Su, S. M. Tuladhar, T. Kirchartz, B. C. Schroeder, I. McCulloch, J. Nelson and D. Roy, *Nanoscale*, 2017, **9**, 2723-2731.
23. E. M. van Schrojenstein Lantman, T. Deckert-Gaudig, A. J. G. Mank, V. Deckert and B. M. Weckhuysen, *Nat. Nanotechnol.*, 2012, **7**, 583-586.
24. N. Kumar, B. Stephanidis, R. Zenobi, A. Wain and D. Roy, *Nanoscale*, 2015, **7**, 7133-7137.
25. N. Lee, R. D. Hartschuh, D. Mehtani, A. Kisliuk, J. F. Maguire, M. Green, M. D. Foster and A. P. Sokolov, *J. Raman Spectrosc.*, 2007, **38**, 789-796.
26. Y. Okuno, Y. Saito, S. Kawata and P. Verma, *Phys. Rev. Lett.*, 2013, **111**, 216101.
27. W. Su and D. Roy, *J. Vac. Sci. Technol. B*, 2013, **31**, 041808.
28. S. Mignuzzi, N. Kumar, B. Brennan, I. S. Gilmore, D. Richards, A. J. Pollard and D. Roy, *Nanoscale*, 2015, **7**, 19413-19418.
29. W. Su, N. Kumar, N. Dai and D. Roy, *Chem. Commun.*, 2016, **52**, 8227-8230.
30. W. Su, N. Kumar, S. J. Spencer, N. Dai and D. Roy, *Nano Res.*, 2015, **8**, 3878-3886.
31. W. Su, N. Kumar, S. Mignuzzi, J. Crain and D. Roy, *Nanoscale*, 2016, **8**, 10564-10569.
32. B. S. Yeo, J. Stadler, T. Schmid, R. Zenobi and W. H. Zhang, *Chem. Phys. Lett.*, 2009, **472**, 1-13.
33. T. Schmid, B. S. Yeo, G. Leong, J. Stadler and R. Zenobi, *J. Raman Spectrosc.*, 2009, **40**, 1392-1399.
34. N. Kumar, W. Su, M. Vesely, B. M. Weckhuysen, A. J. Pollard and A. J. Wain, *Nanoscale*, 2018, **10**, 1815-1824.
35. B. Huang, M. Bates and X. W. Zhuang, *Annu. Rev. Biochem.*, 2009, **78**, 993-1016.
36. B. R. Wood, E. Bailo, M. A. Khiavi, L. Tilley, S. Deed, T. Deckert-Gaudig, D. McNaughton and V. Deckert, *Nano Lett.*, 2011, **11**, 1868-1873.
37. R. Bohme, M. Richter, D. Cialla, P. Rosch, V. Deckert and J. Popp, *J. Raman Spectrosc.*, 2009, **40**, 1452-1457.
38. E. Lipiec, R. Sekine, J. Bielecki, W. M. Kwiatek and B. R. Wood, *Angew. Chem. Int. Ed.*, 2014, **53**, 169-172.
39. T. Deckert-Gaudig, E. Bailo and V. Deckert, *Phys. Chem. Chem. Phys.*, 2009, **11**, 7360-7362.
40. D. Kurouski, T. Deckert-Gaudig, V. Deckert and I. K. Lednev, *Biophys. J.*, 2014, **106**, 263-271.
41. R. H. Webb, *Rep. Prog. Phys.*, 1996, **59**, 427-471.
42. K. A. Willets and R. P. Van Duyne, *Annu. Rev. Phys. Chem.*, 2007, **58**, 267-297.
43. J. M. McLellan, Z.-Y. Li, A. R. Siekkinen and Y. Xia, *Nano Lett.*, 2007, **7**, 1013-1017.
44. S. Kawata and V. M. Shalaev, *Tip Enhancement*, Elsevier, Amsterdam, 2007.
45. N. Kumar, S. Mignuzzi, W. Su and D. Roy, *EPJ Tech. Instrum.*, 2015, **2**, 9.
46. D. Richards, R. G. Milner, F. Huang and F. Festy, *J. Raman Spectrosc.*, 2003, **34**, 663-667.
47. N. Hayazawa, H. Watanabe, Y. Saito and S. Kawata, *J. Chem. Phys.*, 2006, **125**, 244706.
48. M. Asghari-Khiavi, B. R. Wood, P. Hojati-Talemi, A. Downes, D. McNaughton and A. Mechler, *J. Raman Spectrosc.*, 2012, **43**, 173-180.
49. M. Zhang, R. Wang, Z. Zhu, J. Wang and Q. Tian, *J. Opt.*, 2013, **15**, 055006.
50. K. D. Park, Y. H. Kim, J. H. Park, J. S. Park, H. S. Lee, S. Y. Yim, Y. H. Lee and M. S. Jeong, *J. Raman Spectrosc.*, 2012, **43**, 1931-1934.
51. N. Mauser and A. Hartschuh, *Chem. Soc. Rev.*, 2014, **43**, 1248-1262.
52. F. J. GarciaVidal and J. B. Pendry, *Phys. Rev. Lett.*, 1996, **77**, 1163-1166.
53. N. Kumar, A. Rae and D. Roy, *Appl. Phys. Lett.*, 2014, **104**, 123106.
54. G. M. Lerman and U. Levy, *Opt. Express*, 2008, **16**, 4567-4581.

55. J. Wang, X. Wu, R. Wang and M. Zhang, *Detection of Carbon Nanotubes Using Tip-Enhanced Raman Spectroscopy*, InTech, London, 2011.
56. J. Stadler, T. Schmid and R. Zenobi, *Nano Lett.*, 2010, **10**, 4514-4520.
57. P. Wang, D. Zhang, L. Li, Z. Li, L. Zhang and Y. Fang, *Plasmonics*, 2012, **7**, 555-561.
58. D. Zhang, U. Heinemeyer, C. Stanciu, M. Sackrow, K. Braun, L. E. Hennemann, X. Wang, R. Scholz, F. Schreiber and A. J. Meixner, *Phys. Rev. Lett.*, 2010, **104**, 056601.
59. B. S. Yeo, T. Schmid, W. Zhang and R. Zenobi, *Anal. Bioanal. Chem.*, 2007, **387**, 2655-2662.
60. A. Taguchi, N. Hayazawa, Y. Saito, H. Ishitobi, A. Tarun and S. Kawata, *Opt. Express*, 2009, **17**, 6509-6518.
61. N. Kumar, S. J. Spencer, D. Imbraguglio, A. M. Rossi, A. J. Wain, B. M. Weckhuysen and D. Roy, *Phys. Chem. Chem. Phys.*, 2016, **18**, 13710-13716.
62. J. Kalbacova, R. D. Rodriguez, V. Desale, M. Schneider, I. Amin, R. Jordan and D. R. Zahn, *Nanospectroscopy*, 2014, **1**, 12-18.
63. L. Opilik, Ü. Dogan, J. Szczerbiński and R. Zenobi, *Appl. Phys. Lett.*, 2015, **107**, 091109.
64. A. Nakata, T. Nomoto, T. Toyota and M. Fujinami, *Anal. Sci.*, 2013, **29**, 865-869.
65. J. D. Scherger and M. D. Foster, *Langmuir*, 2017, **33**, 7818-7825.
66. N. Martín Sabanés, L. M. Driessen and K. F. Domke, *Anal. Chem.*, 2016, **88**, 7108-7114.
67. Z.-C. Zeng, S.-C. Huang, D.-Y. Wu, L.-Y. Meng, M.-H. Li, T.-X. Huang, J.-H. Zhong, X. Wang, Z.-L. Yang and B. Ren, *J. Am. Chem. Soc.*, 2015, **137**, 11928-11931.
68. D. Kurouski, M. Mattei and R. P. Van Duyne, *Nano Lett.*, 2015, **15**, 7956-7962.
69. X. Wang, J.-H. Zhong, M. Zhang, Z. Liu, D.-Y. Wu and B. Ren, *Anal. Chem.*, 2015, **88**, 915-921.
70. T. Touzalin, S. Joiret, E. Maisonhaute and I. T. Lucas, *Anal. Chem.*, 2017, **89**, 8974-8980.
71. M. Mattei, G. Kang, G. Goubert, D. V. Chulhai, G. C. Schatz, L. Jensen and R. P. Van Duyne, *Nano Lett.*, 2016, **17**, 590-596.
72. T. Touzalin, A. L. Dauphin, S. Joiret, I. T. Lucas and E. Maisonhaute, *Phys. Chem. Chem. Phys.*, 2016, **18**, 15510-15513.
73. C. Williams and D. Roy, *J. Vac. Sci. Technol. B*, 2008, **26**, 1761-1764.
74. C. C. Neacsu, S. Berweger and M. B. Raschke, *Nanobiotechnology*, 2007, **3**, 172-196.
75. J. S. Lloyd, A. Williams, R. H. Rickman, A. McCowen and P. R. Dunstan, *Appl. Phys. Lett.*, 2011, **99**, 143108.
76. T. W. Johnson, Z. J. Lapin, R. Beams, N. C. Lindquist, S. G. Rodrigo, L. Novotny and S. H. Oh, *ACS Nano*, 2012, **6**, 9168-9174.
77. J. Yu, Y. Saito, T. Ichimura, S. Kawata and P. Verma, *Appl. Phys. Lett.*, 2013, **102**, 123110.
78. U. Neugebauer, P. Rosch, M. Schmitt, J. Popp, C. Julien, A. Rasmussen, C. Budich and V. Deckert, *ChemPhysChem*, 2006, **7**, 1428-1430.
79. E. Bailo and V. Deckert, *Angew. Chem. Int. Ed.*, 2008, **47**, 1658-1661.
80. R. H. Rickman and P. R. Dunstan, *J. Raman Spectrosc.*, 2014, **45**, 15-21.
81. M. Ghislandi, G. G. Hoffmann, E. Tkalya, L. Xue and G. De With, *Appl. Spectrosc. Rev.*, 2012, **47**, 371-381.
82. C. Chen, N. Hayazawa and S. Kawata, *Nat. Commun.*, 2014, **5**, 3312.
83. C. E. Harvey, E. M. van Schrojenstein Lantman, A. J. G. Mank and B. M. Weckhuysen, *Chem. Commun.*, 2012, **48**, 1742-1744.
84. T. Hartman, C. S. Wondergem, N. Kumar, A. van den Berg and B. M. Weckhuysen, *J. Phys. Chem. Lett.*, 2016, **7**, 1570-1584.
85. H. Kim, K. M. Kosuda, R. P. Van Duyne and P. C. Stair, *Chem. Soc. Rev.*, 2010, **39**, 4820-4844.
86. K. F. Domke and B. Pettinger, *ChemPhysChem*, 2009, **10**, 1794-1798.
87. M. Sun, Z. Zhang, H. Zheng and H. Xu, *Sci. Rep.*, 2012, **2**, 647.
88. Z. Zhang, L. Chen, M. Sun, P. Ruan, H. Zheng and H. Xu, *Nanoscale*, 2013, **5**, 3249-3252.
89. W. Su, N. Kumar, S. Mignuzzi, J. Crain and D. Roy, *Nanoscale*, 2016, **8**, 10564-10569.

Chapter 2

Extending the Plasmonic Lifetime of Tip-enhanced Raman Spectroscopy Probes

Abstract

Tip-enhanced Raman spectroscopy (TERS) is an emerging technique for simultaneous mapping of chemical composition and topography of a surface at the nanoscale. However, rapid degradation of TERS probes, especially those coated with Ag, is a major bottleneck to the widespread uptake of this technique and severely prohibits the success of many TERS experiments. In this Chapter, we carry out a systematic time-series study of the plasmonic degradation of Ag coated TERS probes under different environmental conditions and demonstrate that a low oxygen (< 1 ppm) and a low moisture (< 1 ppm) environment can significantly improve the plasmonic lifetime of TERS probes from a few hours to > 5 months. Furthermore, using X-ray photoelectron spectroscopy measurements on Ag nanoparticles we show that the rapid plasmonic degradation of Ag coated TERS probes can be correlated to surface oxide formation. Finally, based on the results of this study, we present practical guidelines for the effective use and storage of TERS probes to extend their plasmonic lifetime.

This Chapter is based on: N. Kumar, S. J. Spencer, A. J. Wain, D. Imbraguglio, A. Rossi, B. M. Weckhuysen and D. Roy, *Phys. Chem. Chem. Phys.*, 2016, **18**, 13710-13716.

2.1 Introduction

As discussed in Chapter 1, over the last two decades, tip-enhanced Raman spectroscopy (TERS)[1] has emerged as an advanced nano-analytical technique[2] for simultaneous chemical and topographical surface characterisation at the nanoscale in diverse areas of scientific research[3] such as biology,[4] material science,[5] polymer-blends,[6] solar cells,[7] single wall carbon nanotubes,[8] graphene and other two-dimensional materials,[9-11] catalysis[12-14] and single molecule detection.[15] The principle of TERS is based on the enhancement and confinement of an electromagnetic (EM) field at the apex of a metallic scanning probe microscopy tip when exposed to laser excitation matching its surface plasmon resonance wavelength (λ_{SPR}). This plasmonic enhancement of the EM field underpins the high chemical sensitivity and nanoscale spatial resolution obtained in TERS maps, enabling observation of molecular phenomena far below the optical diffraction limit.

Due to plasmonic resonances in the visible light regime, Ag and Au are the most commonly used metals for preparing TERS probes with λ_{SPR} of typical Ag and Au coated TERS tips falling in the blue-green and yellow-red regions, respectively.[16] Although Au coated tips are chemically more stable, there is weak adhesion of Au to the surface of typical atomic force microscopy (AFM) tips, resulting in metal delamination during TERS imaging[17] and hence significant losses in the plasmonic signal enhancement.[18-20] In contrast, solid Ag and Ag coated TERS tips typically show a much higher EM field enhancement due to the lower imaginary part of the dielectric function compared to Au in the visible light regime, which reduces losses arising from optical absorption.[18-20] However, although plasmonically superior, Ag TERS tips are chemically less stable and rapidly lose their plasmonic signal enhancement in the ambient environment.[21, 22] Opilik *et al.* showed that solid Ag TERS tips become unusable for TERS measurements after 48 hours.[22] Compared to the solid Ag tips, Ag coated tips are more commonly used because of the ease of preparation *via* thermal evaporation from commercial AFM probes that are available in a wide variety of shapes and sizes, as well as ease of use during TERS measurements.[23] However, Ag coated tips are even more susceptible to plasmonic degradation due to atmospheric corrosion of a much thinner (typically 20 nm – 100 nm) Ag layer. This represents a major bottleneck for the adoption of the technique and will ultimately prohibit the success of many TERS experiments, which often require careful optimisation of experimental conditions prior to the measurement, including the time-consuming procedure of precisely aligning the TERS tip with the laser spot. In practice, by the time the actual TERS imaging commences, the Ag coated tips may already exhibit a significantly reduced capability for the plasmonic enhancement of local EM field. Consequently, Ag probes must typically be used on the same day of preparation and cannot be stored for long periods of time.[24]

In this Chapter, we have addressed three basic questions: 1) How quickly do Ag coated tips undergo plasmonic degradation? 2) Can this degradation be controlled? 3) What is the mechanism of degradation? Herein, we have carried out a systematic set of time-series measurements of the plasmonic lifetime of TERS probes under different environmental conditions in order to gain insights into their plasmonic degradation. We demonstrate that the preservation of the plasmonic enhancement of TERS tips critically depends upon the oxygen and moisture content of the environment in which the probes are stored. To the best of our knowledge, this is the first systematic study of the impact of different environmental conditions on the plasmonic lifetime of Ag coated TERS tips. Furthermore, to understand the surface chemistry of Ag nanostructures exposed to the ambient environment we have also performed a time-series investigation of Ag nanoparticles (NPs) using X-ray photoelectron spectroscopy (XPS). Finally, based on the results of this study, we propose strategies for extending the plasmonic lifetime of TERS probes during their storage and use.

2.2 Experimental

2.2.1 TERS System

A bespoke transmission mode TERS system was used for this work that consisted of an inverted confocal microscope (Nikon, Japan) coupled with an AFM (AIST-NT, USA) on top. A schematic diagram of the TERS set-up is shown in Fig. 2.1. A Raman spectrometer (Horiba Scientific, France) with a charged coupled device detector (Andor Technology, UK) was used to measure the Raman spectra in the 300 cm^{-1} – 3700 cm^{-1} spectral range. A frequency doubled Nd:YAG laser (Coherent, USA) with 532 nm wavelength was radially polarised using a liquid crystal polariser (ARCoptix, Switzerland) and focussed onto the sample using a 100×, 1.49 NA oil immersion objective lens (Nikon, Japan). All measurements were conducted in contact mode AFM with 100 μW laser power incident at the sample. A detailed schematic diagram of the optical set-up is presented in Fig. 2.2.

2.2.2 Measurement of Plasmonic Enhancement

The plasmonic signal enhancement of the Ag coated tips was monitored over time by measuring the “contrast” of TERS signals, which is defined as[23]

$$\text{Contrast} = \frac{I_{TERS}}{I_{Far\text{-}field}} - 1 \tag{2.1}$$

where, I_{TERS} and $I_{Far\text{-}field}$ are the intensity of a Raman band when the TERS tip is in contact (Tip-in) and retracted from the sample (Tip-out), respectively. However, in this work the TERS contrast was measured on a bilayer sample using the

methodology reported by Kumar *et al.*[25], which provides a more accurate measurement of the contrast of TERS signals by eliminating the possible far-field artefacts arising from the reflections of excitation laser between the TERS tip and the sample.

2.2.3 TERS Tips and Time-series Measurements

For this study, TERS tips were prepared by first oxidising Si AFM tips (Mikromasch, USA) to a thickness of 300 nm SiO_2 in a tube furnace, and then coating them with a nominal thickness of 60 nm Ag. Thermal evaporation of Ag onto the AFM tips was carried out in a vacuum chamber at 10^{-6} mbar pressure with a slow deposition rate of 0.05 nms^{-1}. A scanning electron microscopy (SEM) image of a representative TERS tip is shown in the inset of Fig. 2.1. In this work, effect of three different environments on the plasmonic lifetime of TERS tips was investigated. (1) Ambient environment: The effect of ambient environment was tested on 5 freshly prepared TERS tips stored in the laboratory immediately after thermal deposition of Ag. For each probe, time-series TERS measurements were performed at an interval

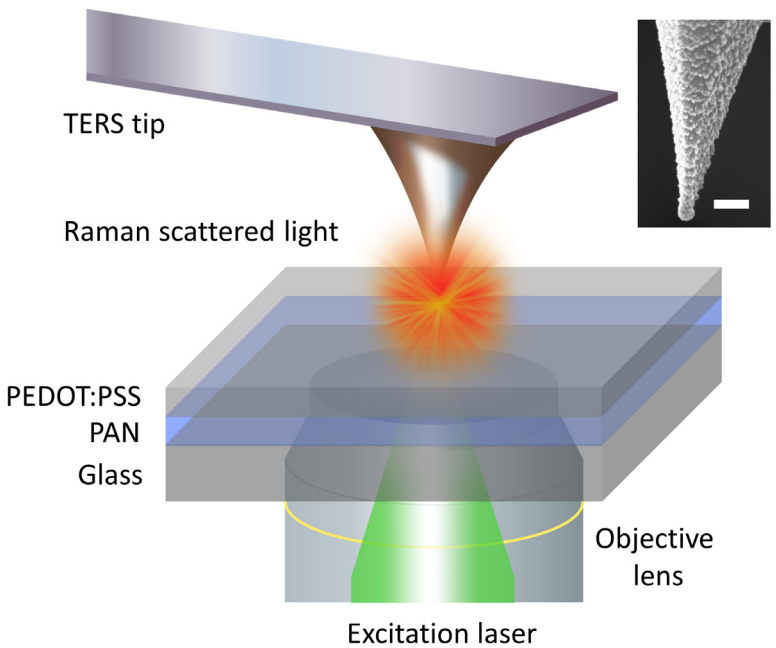

Fig. 2.1 Schematic diagram of the transmission mode TERS apparatus used in this work. TERS and far-field Raman measurements were conducted on a bilayer sample (Top layer – poly (3, 4 ethylenedioxythiophene):poly (styrenesulfonate) (PEDOT:PSS); Bottom layer – polyacrylonitrile (PAN)) developed by Kumar *et al.*[25] A SEM image of a representative TERS tip is shown in the inset. Scale bar: 100 nm.

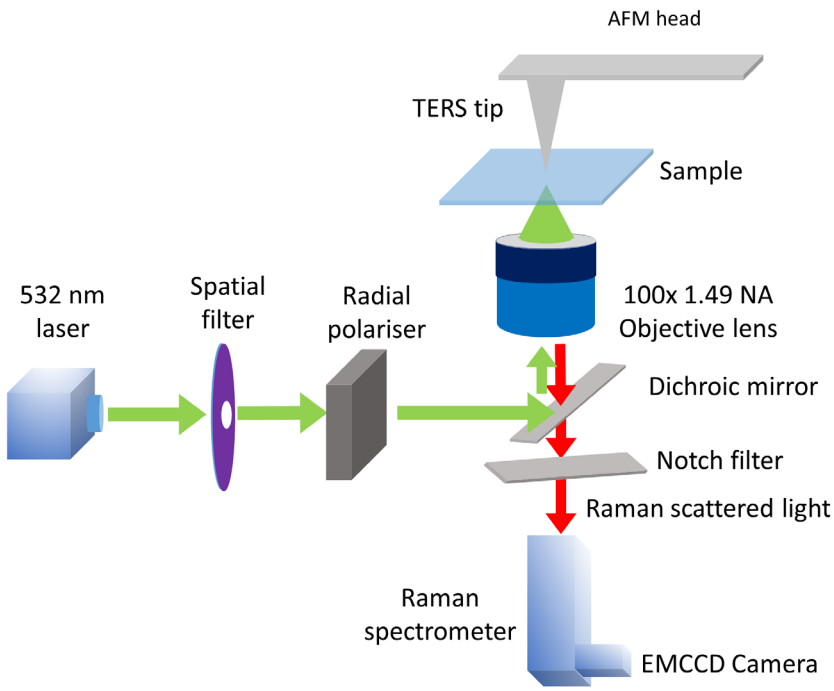

Fig. 2.2 Schematic diagram showing the detailed optical set-up of the bespoke TERS system used in this work.

of 4 hours (h) until the probe lost its plasmonic signal enhancement completely. (2) Vacuum desiccator environment: The effect of environment inside a vacuum desiccator (Duran®, Germany) was tested on 3 sets of 5 TERS tips. TERS measurements were performed using the three different sets of TRES tips after storage times of 3 days, 6 days and 9 days. A pressure of 25 mbar was maintained inside the desiccator using an oil free diaphragm pump (KNF Neuberger Ltd., UK). The contrast of TERS signals measured using the tips was calculated at the end of each storage time using Equation 2.1. (3) Nitrogen glovebox: Finally, effect of a nitrogen-filled glovebox environment (MBRAUN, Germany), was tested on 3 sets of 5 TERS tips, with the plasmonic signal enhancement of three different sets measured after storage times of 1 month, 3 months and 5 months. Sub - parts per million (ppm) concentration of oxygen and moisture was maintained in the glovebox by continuous recirculation of high purity nitrogen gas. The average values of temperature, relative humidity and oxygen in the ambient, vacuum desiccator and nitrogen glovebox environments are listed in Table 2.1. Relative oxygen concentration is calculated as the % of oxygen relative to ambient (21% of the air). Out of the three environments, nitrogen glovebox contained the lowest moisture and

Table 2.1 Storage conditions of ambient, vacuum desiccator and nitrogen glovebox environments.

Environment	Temperature (° C)	Relative humidity (%)	Relative oxygen (%)
Ambient	22.0 ± 0.1	38.7 ± 1.0	100
Vacuum Desiccator	22.0 ± 0.1	15.6 ± 1.0	2.5
Nitrogen Glovebox	18.8 ± 0.1	0.0 (< 1 ppm)	0.0005 (< 1 ppm)

oxygen concentration.

2.2.4 XPS Measurements

To understand changes in the surface chemistry of Ag NPs exposed to ambient conditions we carried out time-series XPS measurements on Ag NPs on a Si substrate. This sample was prepared by thermal deposition of a 10 nm thick Ag film on a Si wafer using exactly the same conditions employed for preparing TERS tips. Topography of the sample was measured using tapping mode AFM. XPS measurements were conducted over time intervals of 0 h (immediately after Ag deposition), 4 h and 17 h under ultrahigh vacuum using a Kratos AXIS Ultra DLD with monochromatic Al Kα excitation. The sample was exposed to the ambient environment in between the XPS measurements similar to the time-series study of TERS tips under ambient conditions. All time-series XPS spectra were acquired from the same location on the Ag NP sample without removing the sample from the sample holder. XPS survey spectra in the 10 eV - 1300 eV binding energy range were acquired at an emission angle of 0^{o} to the surface normal. Analysis area was approximately 700 μm × 300 μm with a sampling depth of < 10 nm. The following analysis conditions were used: 160 eV pass energy, 1 eV steps, 0.2 s dwell per step and 2 sweeps. High resolution O 1s spectra were acquired using 40 eV pass energy, 0.1 eV steps, 0.5 s dwell per step and 2 sweeps. The charge neutraliser was used and charge correction later applied by referencing to the C 1s hydrocarbon peak at 285 eV either in the survey spectra or from associated C 1s high-resolution spectra, as appropriate. CasaXPS software was used to measure the peak areas of the survey spectra using a linear or Tougaard background subtraction. The concentration of the detectable elements present was determined using NPL transmission function (intensity) calibration[26] and average matrix relative sensitivity factors.

2.3 Results and Discussion

2.3.1 Plasmonic Lifetime of TERS Tips under Different Environments

Since most TERS studies are carried out in an ambient environment, we first investigated the plasmonic lifetime of TERS tips under standard laboratory conditions. Plasmonic signal enhancement of TERS tips is known to vary from tip to tip.[27, 28] Therefore, for a more relevant comparison of the degradation of plasmonic signal enhancement under different environmental conditions, all time-series TERS measurements were conducted using sets of 5 TERS tips prepared under same conditions. In the ambient environment, time-series TERS (tip-in) and far-field (tip-out) spectra of 5 freshly prepared TERS tips were measured at intervals of 4 h i.e. at 0 h, 4 h and 8 h. After each TERS measurement, tips were stored in the ambient environment before the next set of measurements. Time-series TERS and far-field spectra of a representative TERS tip are shown in Fig. 2.3. For the fresh Ag coated tip (0 h), clear signal enhancement of the characteristic PEDOT Raman bands (spectral region: 400 cm^{-1} - 1600 cm^{-1})[29] can be observed in the TERS spectrum. The PAN peak at 2247 cm^{-1} is not significantly enhanced in the TERS spectrum indicating no significant increase in the undesirable far-field resulting from the reflection of excitation laser between the TERS tip and the sample. The contrast of

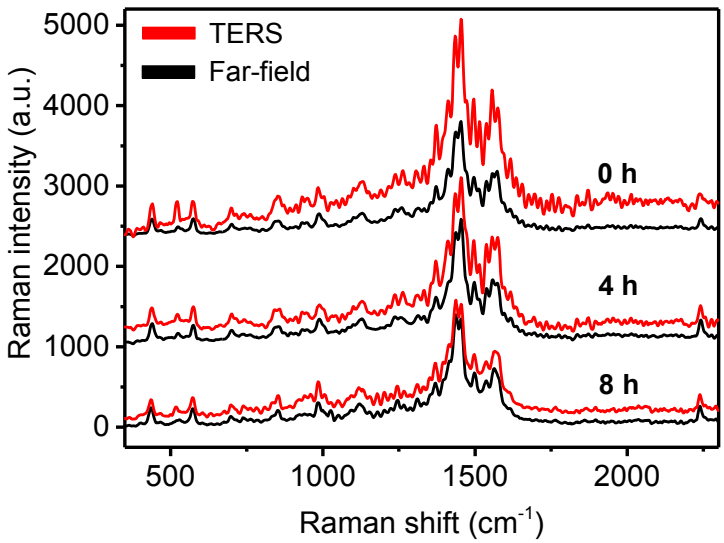

Fig. 2.3 Time-series TERS (red) and far-field (black) spectra of a representative TERS tip measured at intervals of 4 h under ambient laboratory conditions. The plasmonic enhancement of TERS signals rapidly decreases after 4 h and completely disappears after 8 h of exposure to the ambient environment. Laser power at the sample: 100 µW. Integration time: 60 s.

TERS and far-field spectra for the fresh Ag coated tip calculated using Equation 2.1 is ≈ 1. However, after 4 h of exposure to the ambient environment the contrast decreased quite rapidly to ≈ 0.2 indicating an approximately 80% decrease in the plasmonic signal enhancement of the tip. Finally, after 8 h of exposure to the ambient environment, the plasmonic signal enhancement of the TERS tip vanished completely with a contrast of ≈ 0. Time-series measurements of the average contrast of 1454 cm^{-1} PEDOT Raman band from 5 TERS tips are plotted in Fig. 2.4a that show an exponential decay in the degradation of plasmonic signal enhancement over time. From this plot, the average lifetime of these TERS tips, defined as the time after which the TERS contrast reduces to 1/e times or ≈ 37% of their initial value, is estimated to be 2.8 h.

Next, we investigated the plasmonic lifetime of TERS tips stored in a vacuum desiccator, which is a commonly used method to preserve TERS tips. Compared to the ambient environment, both relative humidity and oxygen concentration were lower in the vacuum desiccator by 60% and 97.5%, respectively, as shown in Table 2.1. The average TERS contrast of 3 different sets of 5 TERS tips measured after storage times of 3 days, 6 days and 9 days in a vacuum desiccator is shown in Fig. 2.4b. Comparing Fig. 2.4a and 2.4b, it can be noted that the TERS contrast of freshly prepared tips and the tips stored in the vacuum desiccator for 3 days was similar (≈ 1) indicating that the vacuum desiccator successfully preserves the plasmonic signal

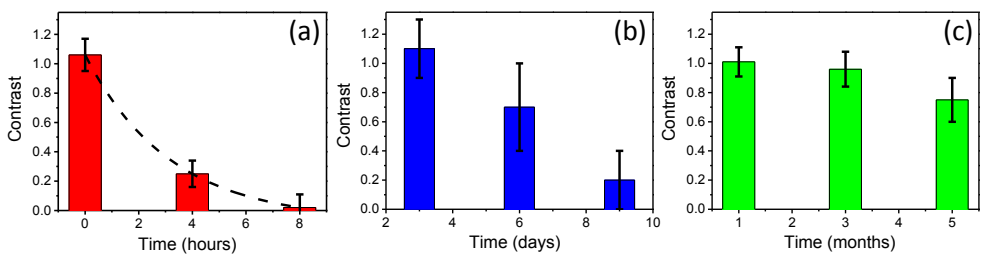

Fig. 2.4 Time-series measurement of plasmonic signal enhancement estimated *via* TERS contrast (Equation 2.1) of tips stored in (a) ambient (b) vacuum desiccator (c) nitrogen glovebox environments. Under ambient conditions, the plasmonic signal enhancement decreases rapidly within the first 4 h disappearing completely within 8 h. An exponential decay trend is observed in the plasmonic signal enhancement within the 8 h period with an average plasmonic lifetime of 2.8 h. The vacuum desiccator environment increases the plasmonic lifetime of TERS tips to a few days. However, the extremely low (< 1 ppm) humidity and oxygen concentration of a nitrogen glovebox provides the best preservation of plasmonic lifetime extending it up to 5 months.

enhancement capability of TERS tips for a few days. However, after 6 days of storage, the plasmonic enhancement decreased by 36%. Finally, after 9 days of storage, the plasmonic signal enhancement decreased by 80% effectively rendering

the TERS tips unusable for TERS measurements. The decrease in the oxygen and moisture content inside a vacuum desiccator compared to the ambient environment (Table 2.1) correlates inversely with the average plasmonic lifetime of TERS tips, increasing it from a few h to a few days. Interestingly, unlike the ambient environment, the degradation of plasmonic signal enhancement of the TERS tips stored in the vacuum desiccator did not exhibit an exponential trend.

Finally, we investigated the effect of an extremely low moisture and oxygen concentration on the plasmonic lifetime of TERS tips. 3 different sets of 5 TERS tips were stored in a nitrogen glovebox with a < 1 ppm concentration of oxygen and moisture for periods of 1 month, 3 months or 5 months, prior to the measurement of their plasmonic signal enhancement. Results of these time-series measurements are shown in Fig. 2.4c. Remarkably, even after a storage time of 1 month in the nitrogen glovebox, the tips showed a TERS contrast (≈ 1) similar to the freshly prepared tips displaying almost no loss of plasmonic signal enhancement. Furthermore, plasmonic signal enhancement decreased only marginally by < 5% for the tips stored for 3 months. Even after 5 months of storage time, the TERS contrast decreased by < 20% indicating that the tips were still usable for TERS measurements. This dramatic increase in the plasmonic lifetime of the TERS tips stored in the nitrogen glovebox highlights the critical role of oxygen and moisture in the degradation of Ag coated TERS tips. Whilst the TERS tips last for only a few h in the ambient environment, the extremely low concentration of oxygen and moisture inside a nitrogen glovebox extends their plasmonic lifetime by up to 5 months.

2.3.2 Time-series XPS Investigation of Ag Nanoparticles

To understand the cause of rapid plasmonic degradation of Ag nanostructures under ambient conditions we carried out time-series XPS measurements of Ag NPs on a Si substrate. The Ag NP sample was prepared using similar conditions employed for preparing TERS tips. An AFM topography image of the Ag NPs is shown in Fig. 2.5a. The typical size of Ag NPs ranged from 11 nm – 17 nm as indicated by the height profile presented in Fig. 2.5b. Ag NPs are similar in size to the Ag grains on the surface of Ag coated tips as shown in Fig. 2.5c. For time-series XPS measurements, Ag NPs were exposed to the ambient laboratory environment for 0 h (immediately after Ag deposition), 4 h and 17 h. The O1s spectra of the Ag NPs showed three kinds of oxygen bonding: oxygen bonded to Si (from thermal SiO_2 present on the Si wafer), C (from environmental contaminants) and Ag. The binding energies of oxygen in these bonds are listed in Table 2.2. The percentage of oxygen bonded to Si, C and Ag can be determined from the O1s spectra by fitting with 3 Gaussian-Lorentzian curves as shown in Fig. 2.6a for the Ag NPs spectrum measured after 0 h of exposure to the ambient environment.

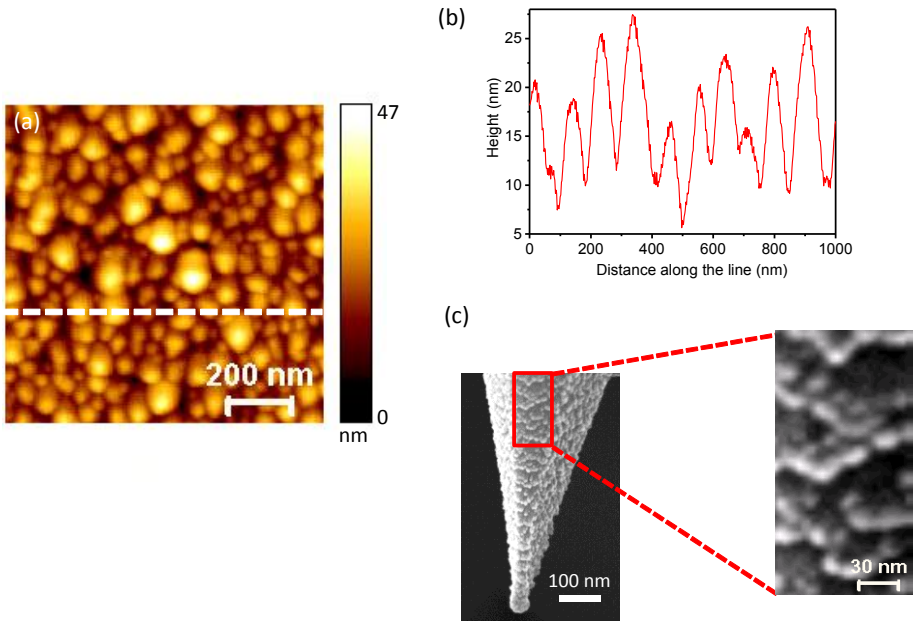

Fig. 2.5 (a) Topography image of Ag NPs on a Si substrate measured using tapping mode AFM. (b) A representative height profile along the dashed line marked in Fig. 2.5a. The height of the Ag NPs along the line ranges from 11 nm – 17 nm. (c) SEM image of a representative Ag coated TERS tip shown in Fig. 1. Zoomed in image of the area marked with red rectangle is shown in the inset. Size of Ag grains on the TERS tip is similar to the Ag NPs in Fig. 2.5a.

The O1s spectrum measured at 0 h showed only a negligible amount (0.1 atomic % of the total elemental composition within the XPS sampling depth) of Ag_XO (x = 1 or 2) oxygen, which rapidly increased to 1.5 % after 4 h of exposure to the ambient environment (Fig. 2.6b). However, subsequently the percentage of Ag_XO oxygen on Ag NPs changed only gradually, increasing by only 0.6 % in the next 13 h (Fig. 2.6c). In the time series O1s spectra, SiO_2 peak was observed to shift due to differential charging during XPS measurements. However, the large binding energy difference between SiO_2 and Ag_xO and careful fitting of the spectra allowed us to reliably calculate the increase in percentage of Ag_xO oxygen over time, which is plotted in Fig. 2.6d. The rapid increase in the oxidation of Ag in the first 4 h correlates well with the rapid decrease in plasmonic signal enhancement of Ag coated TERS tips when exposed to the ambient environment. Interestingly, no sulphur could be detected on the Ag NP surface either in the XPS survey spectrum or high resolution S2p spectrum measured after 17 h of exposure to the ambient environment as shown in Fig. 2.6e and 2.6f. This indicates that for Ag coated TERS tips, surface oxide formation rather than sulphide tarnishing is the dominant cause of the rapid plasmonic degradation, albeit such tarnishing of Ag has been observed on solid Ag

Table 2.2 Binding energy of oxygen bonded to Ag, C and Si.

Oxygen bonding	Binding energy (eV)
AgO	528.6[30]
Ag_2O	529.2[30]
C=O	531.3 – 532.4[31]
C-O	532.5 – 533.5[31]
SiO_2	532.5 – 534.3[30]

probes after longer duration of exposure to the ambient environment.[21, 22]

Since the binding energies of AgO (528.6 eV)[30] and Ag_2O (529.2 eV)[30] are very similar, it is difficult to evaluate the exact contribution of two Ag oxides to the total surface oxidation of Ag NPs over time. However, from the XPS measurements it is possible to calculate atomic % range of Ag bonded to oxygen at the surface of Ag NPs after different time intervals. It can be shown that 95% of the XPS signal is collected from within an estimated sampling depth of ≈ 3.3 nm from the surface of Ag NPs. The universal Equation for the energy dependent effective electron attenuation length (*L*) for a material in XPS is[32]

$$\lambda = \frac{0.65+0.007\mathrm{E}^{0.93}}{\mathrm{Z}^{0.38}} \tag{2.2}$$

where, λ is the electron attenuation length in nm, *E* is the kinetic energy of O1s electrons (957.4 eV for Al monochromatic source) and *Z* is the average atomic number (47, 27.5 and 34 for Ag, AgO and Ag_2O, respectively). Using Equation 2.2, λ for Ag, AgO and Ag_2O is calculated to be 1.1 nm, 1.4 nm and 1.3 nm, respectively.

The sampling depth (*S*) of XPS measurements, where 95% of the detected electrons come from, is represented by the Equation[33]

$$S = 3 \times \lambda \tag{2.3}$$

From Equations 2.2 and 2.3, S is estimated to be 3.3 nm, 4.2 nm and 3.9 nm for Ag, AgO and Ag_2O, respectively.

The calculation of time-series oxidation of Ag NPs is shown in Table 2.3. The second column of Table 2.3 shows Ag_XO oxygen as a percentage of total oxygen estimated from the fitted O1s spectra in Fig. 2.6a, 2.6b and 2.6c. The third column shows Ag_xO oxygen as a percentage of total elemental content, estimated by multiplying the total atomic percentage of oxygen in the XPS survey spectra by column 2. The fourth column shows the Ag atomic percentage calculated from the

XPS survey spectra. Finally, the fifth column shows the estimated percentage range of Ag atoms oxidised at the Ag NPs surface assuming Ag_xO oxygen is distributed uniformly within the XPS sampling depth of ≈ 3.3 nm. For the freshly prepared Ag

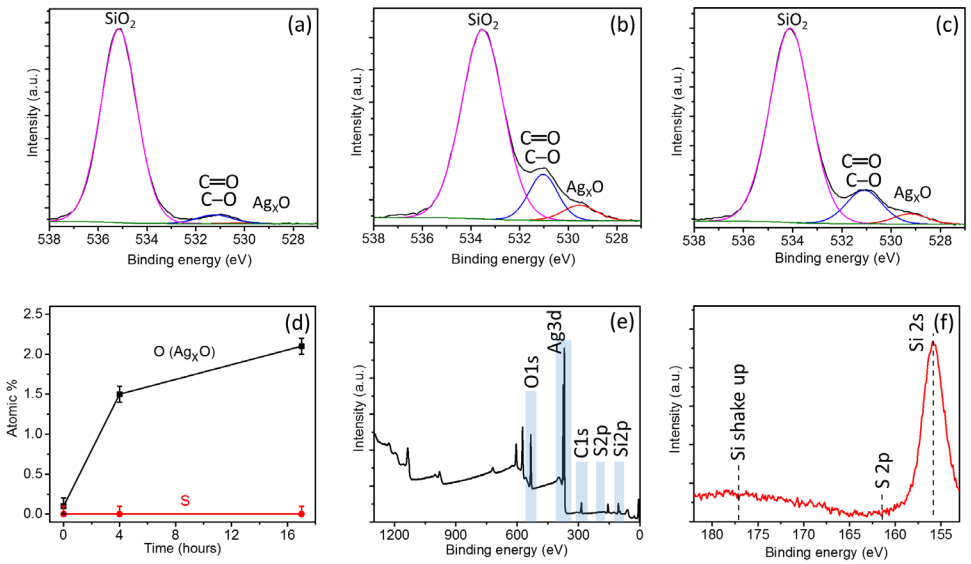

Fig. 2.6 O1s spectra of the Ag NPs after (a) 0 h, (b) 4 h and (c) 17 h of exposure to the ambient environment. Three distinct bands corresponding to the oxygen bonded to Si, C and Ag are fitted with pink, blue and red Gaussian-Lorentzian curves, respectively. (d) Time-series plot of atomic percentage of Ag_xO oxygen and sulphur after 0 h, 4 h and 17 h of exposure to ambient environment. A rapid oxidation of Ag NPs is observed during the first 4 h. (e) XPS survey spectrum and (f) high-resolution S2p spectrum of Ag NPs measured after 17 h of exposure to the ambient environment showed no evidence of S.

NPs, the percentage of Ag atoms bonded to oxygen at the surface lies between 0.4 % – 0.8 %, considering oxidation of all Ag atoms to either AgO or Ag_2O, respectively. Therefore, the actual percentage of oxidised Ag atoms on the surface of Ag NPs would lie within this range. After 4 h of exposure to the ambient environment the oxidation rapidly rises to 6.4 % – 12.8 %. However, in the next 13 h the percentage of Ag atoms bonded to oxygen increases rather gradually to 8.8 % – 17.6 %.

For further confirmation of the oxide formation on Ag NPs, XPS measurements were repeated at 0 h and 17 h on 2 more Ag NP samples with a thin (2 nm) and a thick (19 nm) layer of SiO_2 on Si substrate. Similar results of Ag_xO formation and absence of Sulphur were observed at the surface of both samples. A summary of these results is presented in Table 2.4.

Although similar results of oxide formation on the surface of Ag NPs exposed

to the ambient environment and absence of sulphide formation have been reported in the past,[34] the mechanism of oxide formation is rather unclear. However, a clear correlation between tarnishing of Ag with increasing relative humidity has been

Table 2.3 Time-series surface oxidation of Ag NPs in ambient environment.

Time (h)	Ag_xO oxygen %	Ag_xO oxygen atomic %	Ag atomic %	Oxidised Ag atom %
0	0.3	0.1	25.2	0.4 – 0.8
4	3.6	1.5	23.3	6.4 – 12.8
17	5.3	2.1	24.0	8.8 – 17.6

Table 2.4 Summary of time-series XPS results on Ag NP samples with a thin and thick SiO_2 layer on Si substrate.

Time (h)	Sample 1 (Thin SiO_2)	Sample 2 (Thick SiO_2)
	Ag_XO atomic %	Ag_XO atomic %
0	0.0	0.18
17	5.17	3.58
	S atomic %	S atomic %
0	0.0	0.0
17	0.0	0.0

observed.[35, 36] Time series XPS measurements on Ag NPs clearly indicate a rapid surface oxidation in the first few hours of exposure to the ambient environment. Since silver oxide is non-plasmonic, it appears to be the dominant cause of the plasmonic degradation of Ag coated TERS probes. Therefore, the following strategies are proposed to enhance the plasmonic lifetime of Ag coated TERS tips during storage and use:

- Firstly, any long term storage (> 1 week) or long distance shipping of Ag coated probes must be done in a low (ideally with < 1 ppm) oxygen and moisture environment, to effectively preserve their plasmonic lifetime. For transporting Ag coated TERS tips over long distances, specialised sealed containers could be designed that would maintain the oxygen and moisture at < 1 ppm level.
- Secondly, TERS measurements should be conducted in an inert (nitrogen or argon) environment with a low oxygen and moisture concentration, where

possible. This could be achieved either by enclosing the sample and AFM parts of the TERS system within a sealed box, which can be filled with nitrogen or argon during TERS measurements or by placing the AFM and Raman microscope parts of TERS system inside a nitrogen or argon glovebox.

- However, if it is absolutely necessary to perform TERS measurements in ambient environment, Ag coated TERS tips could be coated with a thin dielectric layer, for example, an ultrathin (< 3 nm) layer of alumina[37] or silica. Although such a coating would slightly decrease plasmonic enhancement,[12] it would block the contact of ambient oxygen and moisture with the Ag thereby enhancing the plasmonic lifetime of the tips. However, the dielectric coating should be pinhole free in order to be most effective.

- Finally, if it is not possible to carry out the TERS measurements in an inert environment or protect TERS probes with a thin dielectric coating, then the TERS measurement time, especially when using a Ag coated probe should be kept to a minimum (preferably < 1 h). Furthermore, for analysing TERS maps that require more than a few hours of acquisition, the exponential trend of the plasmonic degradation of TERS tip should be taken into account. For such long acquisition TERS maps, the plasmonic enhancement of the TERS tip could be measured at the beginning and end of the measurement on a reference sample and TERS data should be appropriately normalised in case of a significant plasmonic degradation.

2.4 Conclusions

In this Chapter, we have investigated the rapid loss of plasmonic signal enhancement of Ag coated TERS probes, which has been one of the longstanding hurdles in the widespread use of TERS technique so far. We have carried out the first systematic time-series investigation of the plasmonic lifetime of Ag coated TERS tips under different environmental conditions and shown that the plasmonic signal enhancement of TERS tips decreases rapidly within the first 4 h of exposure to the ambient environment and disappears completely within 8 h. Storage in a vacuum desiccator improves the plasmonic lifetime of TERS tips from a few hours to a few days. However, a glovebox environment with sub-ppm oxygen and moisture concentration offers the best preservation of plasmonic signal enhancement, extending the plasmonic lifetime of the TERS probes up to 5 months. Furthermore, using time-series XPS measurements on Ag NPs we have demonstrated that a rapid surface oxidation takes place within 4 h of exposure to the ambient environment, which correlates negatively with the plasmonic signal enhancement of TERS tips under similar conditions. Interestingly, no sulphur was detected in any of the XPS

spectra indicating that oxide formation is the dominant cause of rapid plasmonic degradation of Ag coated TERS probes. Finally, based on the results of these studies, guidelines for effective use and storage of Ag coated TERS probes for maximum preservation of their plasmonic lifetime have been proposed. The results of this work are applicable not only to TERS, but also for tip-enhanced fluorescence microscopy and surface-enhanced Raman spectroscopy, which rely on plasmonic Ag nanostructures for signal enhancement. Therefore, the results presented here are expected pave the way for a better preservation and transport of Ag coated probes and improved experimental design, thereby moving TERS and related plasmonic spectroscopies a step closer to becoming routine analytical techniques.

References

1. N. Mauser and A. Hartschuh, *Chem. Soc. Rev.*, 2014, **43**, 1248-1262.
2. C. Blum, L. Opilik, J. M. Atkin, K. Braun, S. B. Kammer, V. Kravtsov, N. Kumar, S. Lemeshko, J. F. Li, K. Luszcz, T. Maleki, A. J. Meixner, S. Minne, M. B. Raschke, B. Ren, J. Rogalski, D. Roy, B. Stephanidis, X. Wang, D. Zhang, J. H. Zhong and R. Zenobi, *J. Raman Spectrosc.*, 2014, **45**, 22-31.
3. N. Kumar, S. Mignuzzi, W. Su and D. Roy, *EPJ Tech. Instrum.*, 2015, **2**, 9.
4. S. Najjar, D. Talaga, L. Schue, Y. Coffinier, S. Szunerits, R. Boukherroub, L. Servant, V. Rodriguez and S. Bonhommeau, *J. Phys. Chem. C*, 2014, **118**, 1174-1181.
5. S. Berweger, C. C. Neacsu, Y. Mao, H. Zhou, S. S. Wong and M. B. Raschke, *Nat. Nanotechnol.*, 2009, **4**, 496-499.
6. L. Xue, W. Li, G. G. Hoffmann, J. G. P. Goossens, J. Loos and G. de With, *Macromolecules*, 2011, **44**, 2852-2858.
7. X. Wang, D. Zhang, K. Braun, H. J. Egelhaaf, C. J. Brabec and A. J. Meixner, *Adv. Funct. Mater.*, 2010, **20**, 492-499.
8. Y. Okuno, Y. Saito, S. Kawata and P. Verma, *Phys. Rev. Lett.*, 2013, **111**, 216101.
9. S. Mignuzzi, N. Kumar, B. Brennan, I. S. Gilmore, D. Richards, A. J. Pollard and D. Roy, *Nanoscale*, 2015, **7**, 19413-19418.
10. A. J. Pollard, N. Kumar, A. Rae, S. Mignuzzi, W. Su and D. Roy, *J. Mater. Nanosci.*, 2014, **1**, 39-49.
11. W. Su, N. Kumar, S. J. Spencer, N. Dai and D. Roy, *Nano Res.*, 2015, **8**, 3878-3886.
12. N. Kumar, B. Stephanidis, R. Zenobi, A. Wain and D. Roy, *Nanoscale*, 2015, **7**, 7133-7137.
13. E. M. van Schrojenstein Lantman, T. Deckert-Gaudig, A. J. G. Mank, V. Deckert and B. M. Weckhuysen, *Nat. Nanotechnol.*, 2012, **7**, 583-586.
14. T. Hartman, C. S. Wondergem, N. Kumar, A. van den Berg and B. M. Weckhuysen, *J. Phys. Chem. Lett.*, 2016, **7**, 1570-1584.
15. R. Zhang, Y. Zhang, Z. C. Dong, S. Jiang, C. Zhang, L. G. Chen, L. Zhang, Y. Liao, J. Aizpurua, Y. Luo, J. L. Yang and J. G. Hou, *Nature*, 2013, **498**, 82-86.
16. M. Zhang, R. Wang, Z. Zhu, J. Wang and Q. Tian, *J. Opt.*, 2013, **15**, 055006.
17. L. T. Nieman, G. M. Krampert and R. E. Martinez, *Rev. Sci. Instrum.*, 2001, **72**, 1691-1699.
18. T. Schmid, L. Opilik, C. Blum and R. Zenobi, *Angew. Chem. Int. Ed.*, 2013, **52**, 5940-5954.
19. P. B. Johnson and R. W. Christy, *Phys. Rev. B*, 1972, **6**, 4370-4379.
20. E. Le Ru and P. Etchegoin, *Principles of Surface-Enhanced Raman Spectroscopy and Related Plasmonic Effects*, Elsevier, Amsterdam, 2008.
21. J. Kalbacova, R. D. Rodriguez, V. Desale, M. Schneider, I. Amin, R. Jordan and D. R. Zahn, *Nanospectroscopy*, 2014, **1**, 12-18.

22. L. Opilik, Ü. Dogan, J. Szczerbiński and R. Zenobi, *Appl. Phys. Lett.*, 2015, **107**, 091109.
23. J. Stadler, T. Schmid and R. Zenobi, *Nanoscale*, 2012, **4**, 1856-1870.
24. R. Rodriguez, E. Sheremet, S. Müller, O. Gordan, A. Villabona, S. Schulze, M. Hietschold and D. Zahn, *Rev. Sci. Instrum.*, 2012, **83**, 123708.
25. N. Kumar, A. Rae and D. Roy, *Appl. Phys. Lett.*, 2014, **104**, 123106.
26. M. Seah, *J. Electron. Spectrosc. Relat. Phenom.*, 1995, **71**, 191-204.
27. A. Hartschuh, E. J. Sanchez, X. S. Xie and L. Novotny, *Phys. Rev. Lett.*, 2003, **90**, 095503.
28. M. S. Anderson and W. T. Pike, *Rev. Sci. Instrum.*, 2002, **73**, 1198-1203.
29. S. Garreau, G. Louarn, J. P. Buisson, G. Froyer and S. Lefrant, *Macromolecules*, 1999, **32**, 6807-6812.
30. J. Moulder, W. Stickle, P. Sobol and K. Bomben, *Handbook of X-ray Photoelectron spectroscopy*, Perkin-Elmer Corporation, Eden Prairie, 1992.
31. G. Bearnson and D. Briggs, *High Resolution XPS of Organic Polymers*, John Wiley & Sons Ltd, Chichester, 1992.
32. M. Seah, *Surf. Interface Anal.*, 2012, **44**, 1353-1359.
33. J. C. Vickerman and G. I.S., *Surface Analysis -The Principal Techniques, 2nd Ed.*, John Wiley & Sons Ltd, Chichester, 2009.
34. T. Oates, M. Losurdo, S. Noda and K. Hinrichs, *J. Phys. D: Appl. Phys.*, 2013, **46**, 145308.
35. L. Volpe and P. Peterson, *Corros. Sci.*, 1989, **29**, 1179-1196.
36. T. Graedel, *J. Electrochem. Soc.*, 1992, **139**, 1963-1970.
37. C. A. Barrios, A. V. Malkovskiy, A. M. Kisliuk, A. P. Sokolov and M. D. Foster, *J. Phys. Chem. C*, 2009, **113**, 8158-8161.

Chapter 3

Nanoscale Chemical Imaging of Solid-liquid Interfaces using Tip-enhanced Raman Spectroscopy

Abstract

Tip-enhanced Raman spectroscopy (TERS) is a powerful tool for non-destructive and label-free surface molecular mapping at the nanoscale. However, to date nanoscale resolution chemical imaging in a liquid environment has not been possible, in part due to the lack of robust TERS probes that are stable when immersed in liquid. In this Chapter, we have addressed this challenge by developing plasmonically active TERS probes with a multilayer metal coating structure that are highly stable within a liquid environment. Using these novel TERS probes, we have compared the plasmonic enhancement of TERS signals in air and water environments for gap and non-gap TERS modes and showed that in both cases, the plasmonic signal enhancement decreases in water. To better understand the attenuation of TERS signal in water, we have performed numerical simulations that revealed a negative correlation between the electric field enhancement at the TERS probe-apex and the refractive index of the surrounding medium. Finally, using these robust probes, we demonstrate TERS imaging with nanoscale spatial resolution in a water environment for the first time by employing single wall carbon nanotubes as a model sample. Our findings are expected to significantly broaden the scope of TERS to a range of scientific disciplines in which nanostructured solid-liquid interfaces play a key role.

This Chapter is based on: N. Kumar, W. Su, M. Veselý, B. M. Weckhuysen, A. J. Pollard and A. J. Wain, *Nanoscale*, 2018, **10**, 1815-1824.

3.1 Introduction

Understanding how the heterogeneity of nanostructured surfaces impacts chemical behaviour on the macroscopic scale plays a vital role in the design, development and implementation of new functional materials. Surface analytical tools are indispensable in the characterisation of such materials, but often lack the desired spatiotemporal resolution and sensitivity to isolate the chemically distinctive features of interest, as well determine their distribution. Moreover, many analytical techniques are not sufficiently adaptable to an *in situ* or *operando* environment, which is critical for the identification of chemically active sites.[1] This need for versatility is particularly pertinent for solid-liquid interfaces, which feature heavily in a wide range of scientific disciplines including heterogeneous catalysis,[2] electrochemistry[3] and biology.[4] The presence of a liquid phase in contact with the sample often hampers nanoscale characterisation, thereby presenting a fundamental challenge in mapping chemical behaviour.

Over the last two decades, tip-enhanced Raman spectroscopy (TERS) has emerged as a powerful nanoanalytical tool for simultaneous topographical and molecular mapping of surfaces at the nanoscale.[5, 6] As described in Chapter 1, TERS primarily operates on the principle of localised surface plasmon resonance (LSPR), whereby a high intensity electric field is generated at the apex of a metallic scanning probe microscopy probe positioned at the focal point of an excitation laser,[7]

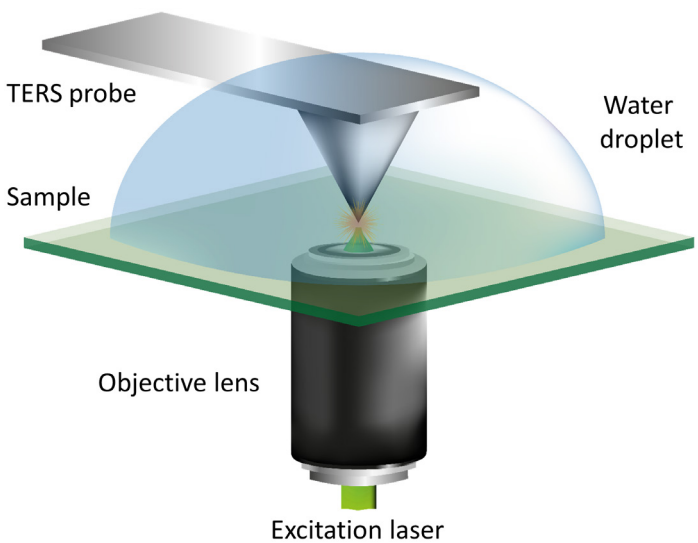

Fig. 3.1 Schematic diagram of the AFM-TERS system employed. For TERS measurements in liquid, a water droplet was placed on the sample and measurements were performed with the TERS probe fully immersed.

as schematically shown in Fig. 3.1. The LSPR between the excitation laser and the metal nanoparticles at the probe-apex, in combination with the lightening rod effect enhances the intensity of the electric field by several orders of magnitude and this enhancement is confined to a region similar to the size of the nanoparticles.[7, 8] This effect simultaneously enhances the sensitivity as well as spatial resolution of Raman microscopy, pushing it far beyond the diffraction limit. Since its first experimental demonstration in 2000,[9-11] TERS has been successfully used for nanoscale chemical characterisation in a wide range of research areas such as organic photovoltaic devices,[12] catalysis,[13-15] polymer-blends,[16] biological cells,[17] crystalline[18] and semiconductor[19] materials, graphene[20, 21] and related two-dimensional (2D)[22] materials, single wall carbon nanotubes (SWCNT)[23] and other one-dimensional (1D)[24] materials and single molecule imaging.[25, 26] However, the majority of these studies have been performed in ambient air or ultrahigh vacuum[27-29] with only a few in aqueous,[30-33] organic liquid[34] and electrochemical[35-39] environments. Furthermore, TERS experiments in liquids have been almost exclusively restricted to point spectroscopy measurements and attempts at 2D chemical imaging have been met with a very limited success. Maisonhaute *et al.* performed TERS mapping of a self-assembled molecular monolayer on Au with partial probe immersion in a thin organic solvent layer.[34] However, no defined spatial features could be resolved in the spectral map, highlighting the difficulty in generating meaningful 2D information using this technique.

One of the key challenges in generating TERS images in a liquid environment is the lack of robust plasmonically active probes. This is especially true for atomic force microscopy (AFM)-TERS, which offers the benefits of tapping and contact mode positional feedback, but typically relies on metal-coated probes which have been shown to exhibit rapid delamination when exposed to liquid.[30] This delamination issue precludes liquid phase TERS imaging due to the long measurement times associated with spectral acquisition at each pixel. To address the stability of TERS probes in liquids, Schmid *et al.*[30] and more recently Scherger and Foster[32] have reported the development of AFM-TERS probes using an adhesion layer of SiO_X for Ag coating or using titanium nitride coating with an alumina protective layer, respectively. In both cases, the stability of the plasmonic coating was improved but physical degradation was still observed after exposure to water for 1h - 2 h and in neither case was chemical imaging demonstrated.

The majority of TERS studies in liquid environments to date have been carried out either in “gap mode”, where the sample is supported on a metal substrate or in “non-gap mode”, where samples are supported on a dielectric substrate. Gap mode TERS measurements benefit from additional signal enhancement due to electromagnetic coupling between surface plasmons in the metallic tip and the metal substrate, To the best of our knowledge, a systematic comparison between TERS

measurements in gap and non-gap modes within a liquid environment has never been reported and the impact of a liquid medium on the TERS signal enhancement across these two configurations has not been investigated in detail.

In this Chapter, we report the development of robust AFM-TERS probes, with a multilayer metal coating structure, which are highly stable and capable of performing successful TERS measurements in both air and liquid environments. Since the nature of the substrate has a major impact on the TERS enhancement factor, we demonstrate TERS measurements in water in both gap and non-gap modes. Non-resonant analyte molecules are investigated, with the TERS probe fully immersed in water and these results are then compared with equivalent measurements in air. Furthermore, to understand the differences in plasmonic enhancement in air and water, we have carried out numerical simulations of the electric field enhancement at the TERS probe-apex in both gap and non-gap modes. Finally, using these robust probes, we demonstrate nanoscale TERS imaging of SWCNTs in a liquid environment in non-gap mode for the first time. This work paves the way for performing spatially resolved, *in situ* chemical characterisation at the nanoscale in a wide range of applications comprising solid-liquid interfaces with nanoscale features.

3.2 Experimental

3.2.1 TERS Probe Preparation

TERS probes with three different types of metal coatings were prepared and tested for their stability in a liquid environment: (1) Ag coated TERS probes were prepared by oxidising commercial Si AFM cantilevers (CSC17/No Al, MikroMasch, USA) to a thickness of 300 nm SiO_2 and then depositing a 100 nm thick Ag layer using a vacuum evaporator (MB 200B, MBRAUN, Germany) at a pressure of 10^{-6} mbar *via* thermal evaporation; (2) Cr-Ag coated TERS probes were prepared by depositing 3.5 nm Cr, followed by 100 nm Ag layers onto oxidised Si AFM cantilevers; (3) Cr-Au-Ag coated TERS probes were prepared by sequentially depositing 3.5 nm Cr, 10 nm Au and 100 nm Ag layers onto oxidised Si AFM cantilevers. Deposition rates of 0.02 nm s^{-1}, 0.03 nm s^{-1} and 0.05 nm s^{-1} were used for the deposition of Cr, Au and Ag, respectively.

3.2.2 TERS set-up and measurements

Measurements were performed using a bespoke transmission-mode TERS system consisting of an AFM (Combiscope, AIST-NT, USA) secured on the top of an inverted confocal optical microscope (Ti-U Eclipse, Nikon, Japan) attached to a Raman spectrometer (iHR 320, HORIBA Scientific, France) and a charge coupled device detector (Newton, Andor Technology, UK). All confocal Raman and TERS measurements were conducted using 532 nm excitation laser, which was radially polarised and focussed on the sample using a 1.49 NA, 100× oil immersion microscope objective (Apo TIRF, Nikon, Japan). All TERS measurements were performed using a contact mode AFM feedback. Far-field measurements were conducted by retracting the TERS probe from the sample and refocussing the laser at the same spot on the sample. The intensity of Raman bands in the measured TERS and far-field spectra was calculated from the height of fitted Lorentzian curves after linear background subtraction.

3.2.3 Sample Preparation

Three different samples were investigated in this study:
(1) Polystyrene (PS) thin film samples for non-gap mode TERS measurements were prepared by spin coating a 20 mg ml^{-1} solution of PS (Sigma-Aldrich, USA) in chloroform onto 0.17 mm thick glass coverslips at 2000 revolutions per minute for 2 minutes.
(2) Biphenyl thiol (BPT) self-assembled monolayer (SAM) samples for gap mode TERS measurements were prepared by first depositing 3 nm Cr followed by 10 nm Au layer on glass coverslips *via* thermal evaporation. The Au coated coverslips were then immersed in 5 mM solution of BPT (Sigma-Aldrich, USA) in ethanol for 18 h at 50° C in order to form a densely packed BPT SAM. Samples were rinsed in ethanol and deionised water to remove any physisorbed molecules from the sample surface.
(3) SWCNT samples for TERS imaging were prepared by depositing SWCNTs (NIST, USA) from a solution of 1 % deoxycholate onto piranha cleaned (3-aminopropyl)triethoxysilane functionalised glass coverslips.

3.3 Results and Discussion

3.3.1 Development of Robust TERS Probes

AFM-TERS probes are typically prepared by coating commercial Si AFM cantilevers with a thin film (20 nm – 100 nm) of Ag or Au. However, metal coating of such probes is not stable when exposed to an aqueous environment. Fig. 3.2a depicts a scanning electron microscopy (SEM) image of a typical Ag coated TERS

probe and Fig. 3.2b shows an SEM image of a Ag probe after immersing in water for 1 h at room temperature. The Ag coating of the TERS probe exhibits evidence of severe localised corrosion and delamination after exposure to the aqueous environment. Loss of surface material and exposure of the underlying SiO_2 surface is clearly observed on the probe itself, as well as the cantilever (Fig. 3.2c and 3.2d).

To improve the stability of the Ag coating in water, we first tried an adhesion layer of 3.5 nm Cr between the SiO_2 surface of the oxidised AFM cantilevers and 100 nm Ag coating. Fig. 3.2e and 3.2f show SEM images of a Cr-Ag coated TERS probe before and after immersion in water for 1 h. Although the adhesion of the Ag coating is improved for the Cr-Ag probe compared to the Ag-only coated probe, the coating still undergoes degradation. Parts of the Ag coating are lost from several regions of the probe shaft as well as the cantilever (Fig. 3.2g and 3.2h).

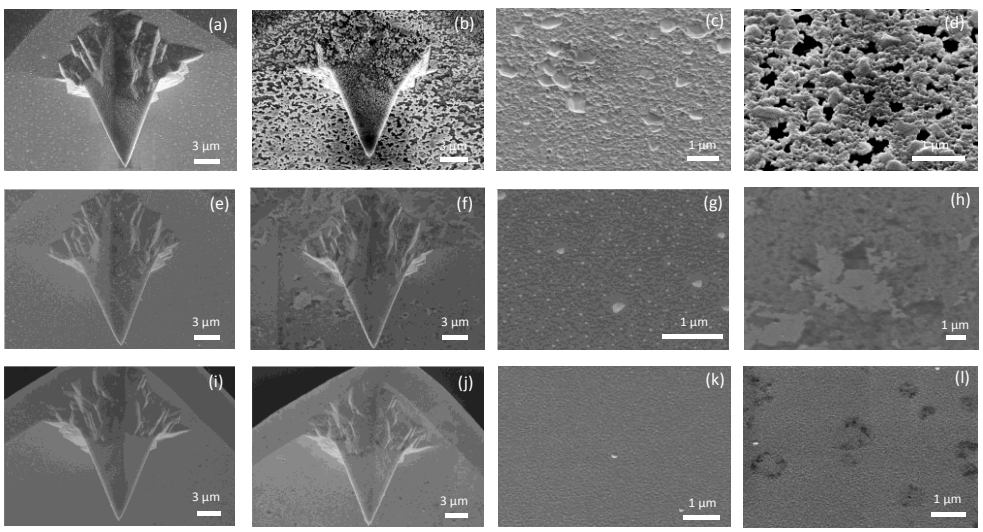

Fig. 3.2 SEM images of a Ag coated TERS probe before (a) and after (b) immersing in water for 1 h. SEM images of the cantilever of the probes shown in Fig. 3.2a (c) and Fig. 3.2b (d). SEM images of a Cr-Ag coated TERS probe before (e) and after (f) immersing in water for 1 h. SEM images of the cantilever of the probes shown in Fig. 3.2e (g) and Fig. 3.2f (h). SEM images of a Cr-Au-Ag coated TERS probe before (i) and after (j) immersing in water for 1 h. SEM images of the cantilever of the probes shown in Fig. 3.2i (k) and Fig. 3.2j (l). The origin of the circular patches observed in Fig. 3.2l is not clear, but the shape is consistent with a "coffee ring effect" resulting from residue remaining on the surface after evaporation of the water.

Finally, we used a 10 nm buffer layer of Au between the Cr and Ag layers, since Cr and Au are known to exhibit very strong adhesion.[40, 41] Fig. 3.2i and 3.2j show the SEM images of Cr-Au-Ag coated probes before and after immersion in water for 1 h. In this case, the metal coating of the TERS probe shows no evidence

of degradation on the probe shaft or the cantilever (Fig. 3.2k and 3.2l). SEM images of two additional Cr-Au-Ag coated TERS probes before and after immersion in water for 1 h are presented in Fig. 3.3, showing complete preservation of Ag coating after

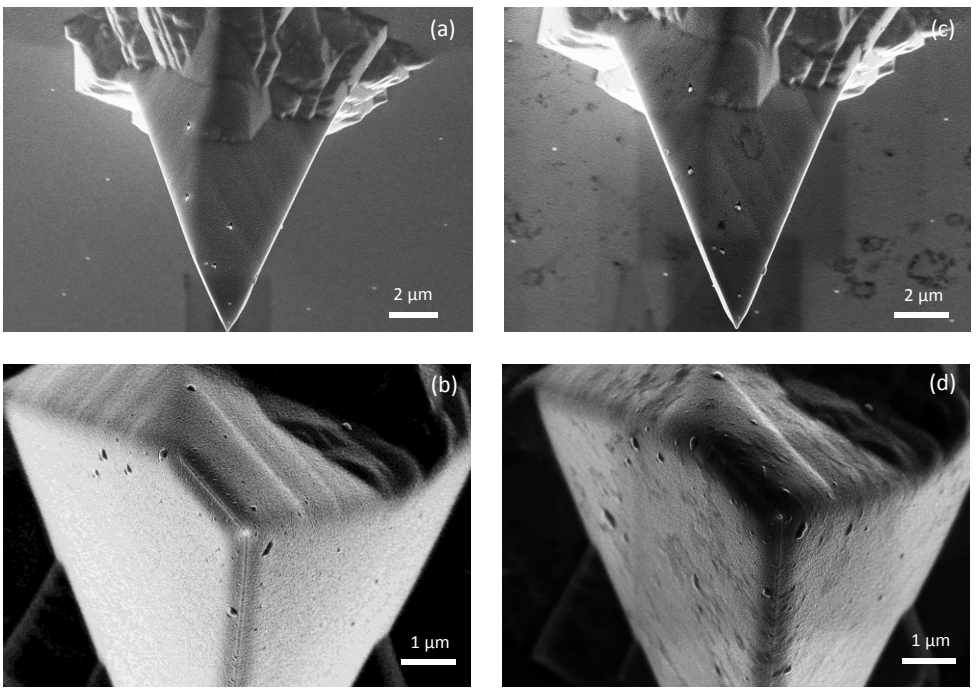

Fig. 3.3 (a), (b) SEM images of two different Cr-Au-Ag coated TERS probes before immersion in water showing the side and top views, respectively. (c), (d) SEM images of the TERS probes shown in Fig. 3.3a and 3.3b, respectively after immersion in water for 1 h. Note that Ag coating of the TERS probes is fully preserved after exposure to water. As in Fig. 3.2l, there is evidence of the "coffee ring effect" in Fig. 3.3c and 3.3d.

exposure to the aqueous environment. The significant improvement in water resistance of the Cr-Au-Ag coated probes likely relates to the improved continuity of the Ag coating resulting from the better adhesion between Ag and Au compared to Ag and Cr. The SEM image of the Ag coated TERS probe cantilever in Fig. 3.2c shows that the coating is rather inhomogeneous containing a significant number of pinholes. This can expose the underlying SiO_2 surface to water, leaving the Ag layer susceptible to oxidation and delamination from the underside. In contrast, the Cr-Ag and Cr-Au-Ag probes (Fig. 3.2g and 3.2k) show a progressive improvement in the uniformity of the Ag coating, which correlates with the corresponding improvement in their water resistance. Given their high stability in water, all TERS measurements in this study were performed using Cr-Au-Ag coated TERS probes.

3.3.2 Comparison of TERS Plasmonic Enhancement in Air and Water

To compare the TERS plasmonic enhancement in air and water, we performed TERS measurements in gap and non-gap modes using Cr-Au-Ag coated TERS probes. Non-gap mode TERS measurements were performed on a thin film of PS on glass substrate. The thickness of the PS film was estimated to be of the order of 100 nm, based on AFM measurements. Spectra measured with the TERS probe in contact with the sample (TERS) and retracted from the sample (far-field) in air are presented in Fig. 3.4a. In both cases, intense Raman bands are observed at 1002 cm^{-1} (ring breathing mode) and 1602 cm^{-1} ($\nu_{C=C}$).[16, 42] As expected, the intensity of these bands is higher in the TERS spectrum than the far-field due to the plasmonic enhancement of local electric field. Note that the TERS spectrum represents the sum of Raman intensity generated in the near-field (plasmonically enhanced electric-field region at the TERS probe-apex) as well as the far-field. The enhancement factor (EF) of a Raman band due to the TERS effect is defined as[43]

$$EF = \left(\frac{I_{TERS}}{I_{FF}} - 1\right)\frac{V_{FF}}{V_{NF}} \tag{3.1}$$

where, I_{TERS} and I_{FF} are the intensity of a Raman band with the TERS probe in contact and retracted from the sample respectively. V_{NF} and V_{FF} are the sampling volumes associated with the near-field and far-field measurements, respectively. For the Raman system used in this work the laser spot size is estimated to be 450 nm, based on confocal Raman imaging of SWCNTs, and the axial resolution is of the order of 1000 nm, estimated from vertical (z direction) measurements of a single layer graphene flake. Therefore, the far-field sampling volume of the system is approximated to a cylinder with a diameter equal to 450 nm and a height equal to the PS film thickness (114 nm), yielding a value of 7.25×10^7 nm^3. The lateral size of the near-field enhancement is usually estimated from the size of the TERS probe-apex.[12, 14, 30, 43-45] Furthermore, the Raman enhancement has been shown to decay within a distance comparable to the radius of the TERS probe-apex.[12, 46-48] Therefore, the near-field sampling volume is approximated to a hemisphere underneath the TERS probe apex with a radius of 20 nm, giving a value of 1.68×10^4 nm^3. Using Equation 3.1, the EF of TERS signals in air with three nominally identical probes was calculated using the intensity of the PS Raman band at 1602 cm^{-1} to be $8.6 \pm 2.5 \times 10^3$, where the uncertainty is the standard deviation. This band was chosen for the EF calculation to facilitate comparison with the gap mode TERS measurements on BPT SAM presented below, in which the same aromatic vibrational mode is excited.

Next, TERS measurements of the PS thin film were performed in a liquid

environment by placing a water droplet on the sample surface with the TERS probe fully immersed inside as illustrated in Fig. 3.1. The resulting TERS and far-field spectra are depicted in Fig. 3.4b. In water, the far-field signal intensity of the 1602 cm^{-1} band was found to decrease by a factor of 3.6 ± 0.9 compared to air, which is similar to the attenuation reported by Sabanés *et al.*,[33] who attributed the loss in intensity to a distortion of laser focus resulting from the presence of water on the sample. This loss of optical coupling most likely originates from a combination of laser focus distortion and dielectric loss of laser field intensity due to the higher refractive index (RI) of water compared to air as discussed in the next

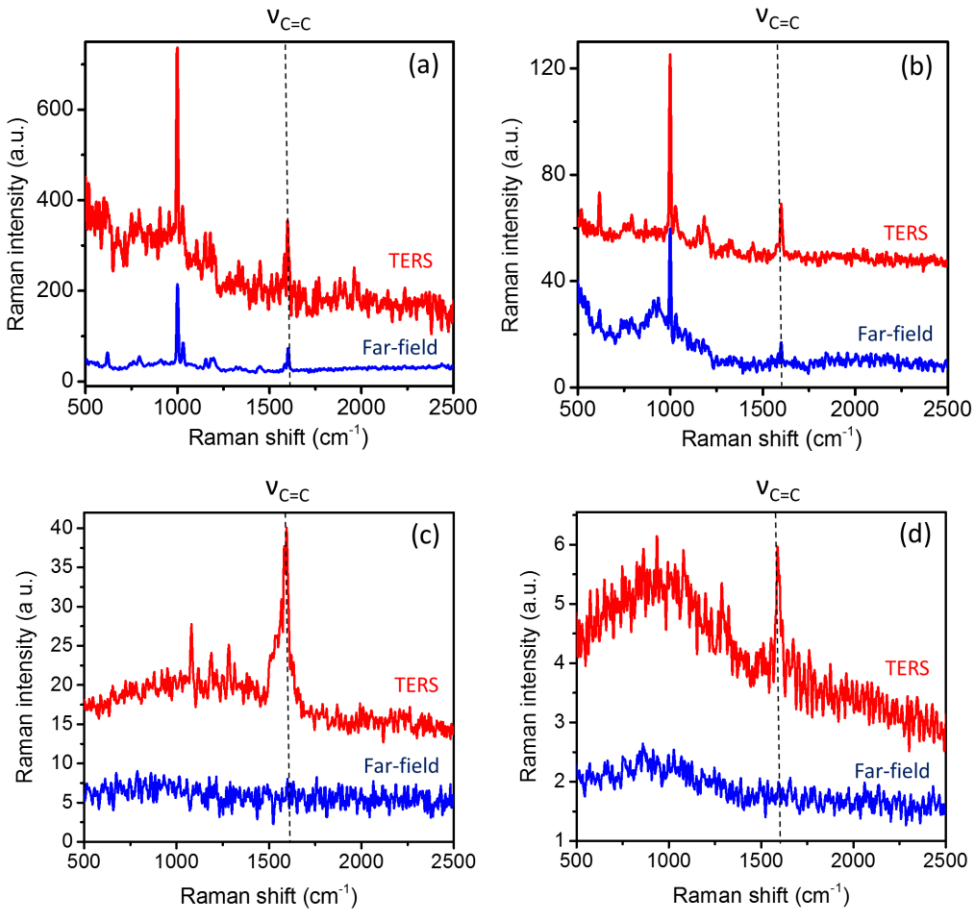

Fig. 3.4 TERS and far-field Raman spectra of a PS thin film on glass in (a) air and (b) water. Integration time: 60 s, laser power at the sample: 170 µW. TERS and far-field spectra of a BPT SAM on a Au substrate in (c) air and (d) water. Integration time: 1 s in air, 60 s in water, laser power at the sample: 117 µW. Raman intensity is measured in arbitrary units (a.u.).

section. However, since the EF in Equation 3.1 is determined from the ratio of the TERS and far-field signal intensity, our calculation of EF should not be affected by the attenuation of optical coupling in water. In the water environment, the EF of the 1602 cm^{-1} Raman band was estimated to be 6.0 ± 3.4 × 10^3, showing a slight reduction of the mean EF by a factor of 1.4 ± 0.9 compared to air. The similarity of TERS EF measured in air and water indicates that, despite the decrease in optical coupling discussed above, TERS probes undergo efficient LSPR with the excitation laser in water. Notably, compared to the 1602 cm^{-1} band, the highest intensity PS Raman band at 1002 cm^{-1} exhibited a lower mean EF value of 6.0 ± 3.9 × 10^3 and 3.0 ± 1.7 × 10^3 in air and water, respectively. This corresponds to a decrease in EF by a factor of 2.0 ± 1.7, similar to the 1602 cm^{-1} band.

To compare the plasmonic enhancement in air and water in gap mode, we carried out TERS measurements on a BPT SAM formed on a 10 nm thick Au film on a glass substrate. Fig. 3.4c shows TERS and far-field spectra measured on the BPT SAM in air. In the far-field, no Raman bands are observed in the spectrum because the sensitivity of confocal Raman spectroscopy is too low to produce a detectable signal from a monolayer of BPT molecules present within the confocal probe volume. This is consistent with the previously reported far-field measurements of SAMs of organic molecules adsorbed on Au.[30, 33, 34] However, in the near-field spectrum, due to the strong plasmonic enhancement of the electric field at the TERS probe-apex, the characteristic BPT Raman bands at 1081 cm^{-1} (δ_{C-H}, 1285 cm^{-1} ($\nu_{C=C}$) and 1593 cm^{-1} ($\nu_{C=C}$) become clearly visible.[49, 50]

The TERS and far-field Raman spectra from the BPT SAM sample measured in water are shown in Fig. 3.4d. Similar to the measurements in air, no Raman bands are observed in the far-field spectrum measured in water, whereas they clearly appear in the TERS spectrum. However, the TERS signal intensity is significantly reduced in water compared to air such that only the BPT Raman band at 1593 cm^{-1} is clearly visible in the TERS spectrum. The average TERS intensity of the 1593 cm^{-1} BPT Raman band measured using three nominally identical probes was found to decrease by an order of magnitude from 15 ± 5 a.u. in air to 1.5 ± 0.4 a.u. in water. This reduction in signal intensity in water compared to air is comparable to previous reports of STM-TERS measurements on a thiophenol SAM, a similar non-resonant probe molecule.[33] Furthermore, the signal to noise ratio (SNR) of the same TERS band also decreases from 13 ± 1 in air to 4.7 ± 0.1 in water, where the noise level was determined from the standard deviation of TERS intensity between 1710 cm^{-1} and 2500 cm^{-1}. This suggests a significant loss in TERS sensitivity in water compared to air. Interestingly, although no Raman bands were observed in the far-field, the noise level in the far-field spectra, calculated from the standard deviation of Raman intensity between 1470 cm^{-1} and 1670 cm^{-1}, was found to decrease by a factor of 10 ± 5 in water compared to air. Comparison of this with the

factor of 3.6 calculated above for the PS film measurements suggests that the far-field optical losses associated with water in gap mode are about three times higher than in non-gap mode.

Since no BPT Raman bands are observed in the far-field, it is not possible to calculate the EF of the TERS signals in Fig. 3.4c and 3.4d using Equation 3.1. However, it is possible to estimate the minimum value of EF by assuming that the intensity of the 1593 cm^{-1} BPT Raman band in the far-field is at most equal to the noise level in the same spectral range. In the case of a molecular monolayer, the near-field and far-field sampling volumes in Equation 3.1 can be approximated by the respective probe areas at the sample surface.[43] These probe areas can be estimated from the diameter of the TERS probe-apex (≈ 40 nm, measured using SEM) and the excitation laser spot size (≈ 450 nm), respectively.[30, 43] Using this approach, the minimum EF of the 1593 cm^{-1} BPT Raman band is estimated to be $1.1 \pm 0.4 \times 10^3$ and $1.1 \pm 0.3 \times 10^3$ in air and water, respectively. The similarity in these minimum EF values indicates that the loss in near-field sensitivity in water evidenced by the decrease in SNR, is compensated for by the decrease in far-field intensity resulting from the optical losses discussed above. However, this comparison of minimum EFs should be treated with caution since their calculation is clearly complicated by varying noise levels between air and water. For ease of comparison, the EF and SNR values estimated from the gap and non-gap mode TERS measurements are summarised in Table 3.1.

Table 3.1 Summary of the EF values of TERS measurements in gap and non-gap modes in air and water and comparison with electric field enhancement determined from numerical simulations.

Experimental measurement of TERS EF		
	Non-gap mode EF	Gap mode minimum EF (TERS SNR)
Air	$8.6 \pm 2.5 \times 10^3$	$1.1 \pm 0.4 \times 10^3$ (13 ± 1)
Water	$6.0 \pm 3.4 \times 10^3$	$1.1 \pm 0.3 \times 10^3$ (4.7 ± 0.1)
Air : Water Ratio	1.4 ± 0.9	1 ± 0.5 (2.8 ± 0.2)
Numerical simulations of electric field enhancement		
	Non-gap mode	Gap mode
Air	5.3	1875.2
Water	2.7	453.3
Air : Water Ratio	1.9	4.1

An additional observation evident from time-series TERS measurements in gap mode was that the signal intensity from the BPT SAM was found to decay in air

as shown in the time-series TERS spectra presented in Fig. 3.5a. A plot of the 1593 cm^{-1} band intensity versus time for BPT TERS signal from the time-series spectra measured in air is shown in Fig. 3.5b. The 1593 cm^{-1} band intensity decreased to 50 % of its initial value (half-life) within approximately 2 minutes, based

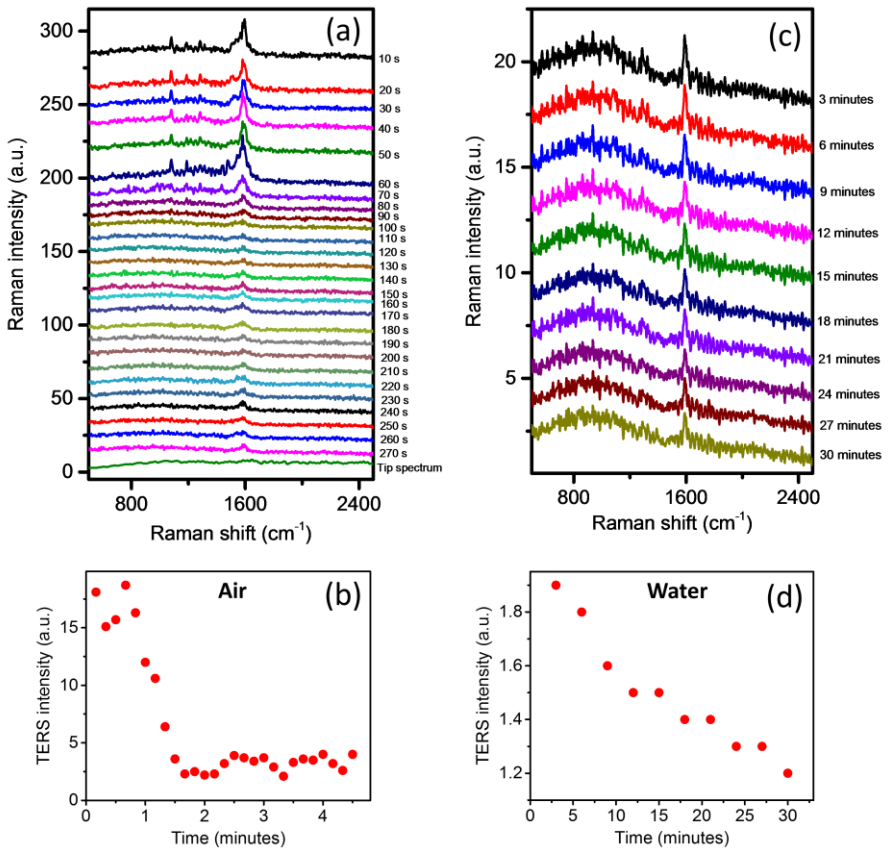

Fig. 3.5 (a) Time-series TERS spectra measured from BPT SAM on Au in air at intervals of 9 s. Integration time: 1 s. Laser power at the sample: 117 μW**.** (b) Plot of the TERS intensity of 1593 cm^{-1} BPT band versus time calculated from the time-series spectra shown in Fig. 3.5a. (c) Time-series TERS spectra measured from BPT SAM on Au in water at intervals of 2 minutes. Integration time: 60s. Laser power at the sample: 117 μW**.** TERS spectra measured from the BPT SAM in water have been normalised by integration time for comparison with the corresponding measurements in air. Spectra have been shifted vertically for easier visualisation. (d) Plot of the TERS intensity of 1593 cm^{-1} BPT band versus time calculated from the time-series spectra shown in Fig. 3.5c. Note that the time-series spectra presented in Fig. 3.5a and 3.5c were measured using the same TERS probe. After performing the time-series TERS measurements shown in Fig. 3.5a and 3.5c the cleanliness of the TERS probe was checked on a clean Au coated glass coverslip. The tip spectrum is shown at the bottom of the plot in Fig. 3.5a, which confirmed the cleanliness of the TERS probe.

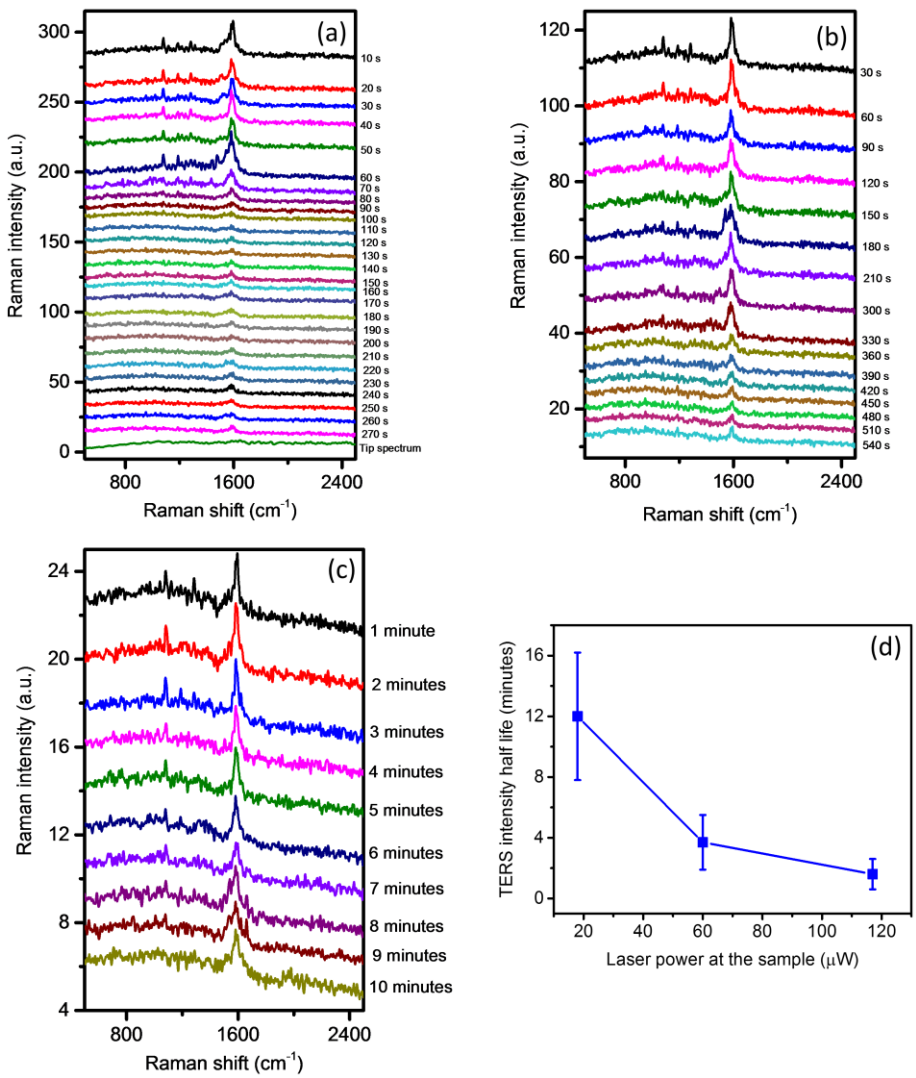

Fig. 3.6 Time-series TERS spectra measured from BPT SAM on Au in air using a laser power of (a) 117 μW (b) 60 μW (c) 18 μW at the sample. Integration time: 1s. Spectra have been vertically shifted for easier visualisation. (d) Plot of the half-life of 1593 cm^{-1} band TERS intensity versus laser power at the sample based on time-series TERS measurements performed using three nominally identical probes. Half-life is defined as the time for the TERS signal intensity to reduce to half of its initial value. The TERS intensity half-life is found to be negatively correlated with the excitation laser power at the sample consistent with laser induced thermal desorption of the SAM under the enhanced electric field of the TERS probe. The time-series spectra presented in Fig. 3.6a - 3.6c were measured using the same TERS probe. After performing the time-series TERS measurements shown in Fig. 3.6a - 3.6c the cleanliness of the TERS probe was checked on a clean Au coated glass coverslip. The tip spectrum is shown at the bottom of the plot in Fig. 3.5a, which confirmed the cleanliness of the TERS probe.

on average TERS measurements from three nominally identical TERS tips. In contrast, whilst the absolute TERS signal intensity was supressed by the presence of water, it was found to decay relatively gradually in this environment, with a half-life of > 30 minutes as shown in the time-series spectra in Fig. 3.5c and the plot of the 1593 cm^{-1} band intensity versus time in Fig. 3.5d. We propose that the attenuation of TERS signal in air arises from thermal degradation of the BPT SAM possibly *via* molecular desorption in the intense TERS near-field, where local temperature can increase by up to 50° C.[27, 51] Such heating effect from LSPR has been previously shown to cause desorption of analyte molecules in surface-enhanced Raman spectroscopy (SERS) measurements leading to a complete loss of signal.[52] In our TERS measurements, the presence of water not only decreases the electric field enhancement, but is also expected to act as a heat sink, improving heat dissipation through thermal conduction.[30, 53] Consistent with this theory, the half-life of the TERS signal decay in air was found to be negatively correlated with excitation laser power, as shown in Fig. 3.6.

3.3.3 Numerical Simulation of Electric Field Enhancement in Air and Water

To better understand the observed differences in plasmonic signal enhancement in gap and non-gap mode TERS configurations, we performed numerical simulations using finite-element model in Comsol Multiphysics®. A model of the TERS probes with a multilayer coating of 3.5 nm Cr, 10 nm Au and 100 nm Ag, as used in this study, was constructed. The electric field enhancement was calculated at the TERS probe-apex in non-gap (glass substrate) and gap (10 nm Au on a glass substrate) modes in both air and water environments. The details of the simulation model are presented in Fig. 3.7. Fig 3.8a and 3.8b show simulated maps of the electric field enhancement surrounding a TERS probe on a glass substrate in air and water, respectively. Electric field enhancement is defined as E/E_0, where E is the amplitude of electric field at the substrate (beneath the probe apex) with the TERS probe present and E_0 is the electric field amplitude (=1) at the substrate without the TERS probe. The calculated enhancement is found to be 1.9 times lower in water compared to air. This is consistent with our experimental results, where the mean EF of PS TERS signals decreased by a factor of 1.4 in water compared to air. Equivalent electric field enhancement simulations for a TERS probe on 10 nm Au film in air and water are shown in Fig. 3.8c and 3.8d, respectively. The calculated enhancement is clearly greater in air compared to water but in both cases is spatially localised to the contact point between the probe-apex and the sample. A quantitative comparison of the calculated electric field enhancement in air and water is presented

in Table 3.1, along with the relevant experimental values discussed in the previous section. The maximum electric field enhancement in gap mode determined through simulations is found to be 4.1 times lower in water than air, indicating a stronger TERS enhancement in air. This is consistent with our experimental observation of a lower sensitivity for TERS measurements of the BPT SAM on Au in water. Although the EF of TERS measurements in gap mode cannot be precisely determined due to

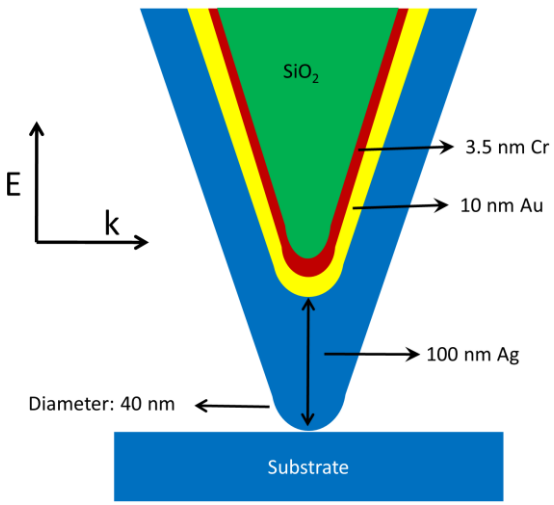

Fig. 3.7 Schematic diagram of the model used for numerical simulation to calculate electric field enhancement at the apex of a Cr-Au-Ag coated TERS probe. Conical SiO_2/Ag probes with a spherical apex were used in the geometric model constructed in COMSOL Multiphysics®, a commercial finite element modelling software. The probe and sample characteristics were modelled on the properties of the probes used experimentally in this work. The height and cone angle of the TERS probe were set to 450 nm and 45°, respectively. The nominal thickness of Cr, Au and Ag films on SiO_2 probe were set to 3.5 nm, 10 nm and 100 nm, respectively with the apex diameter of 40 nm. For gap mode calculations, the thickness of the Au film on glass substrate was set to 10 nm. Since all experimental measurements were performed in contact mode AFM, the distance between the Ag coated probe and the sample was set to 0.5 nm. A fine physics-controlled mesh with a minimum mesh size of 0.2 nm was used between the probe-apex and the sample surface. In order to simplify the calculations, a plane electromagnetic wave with 532 nm wavelength was incident on the TERS probe from the left side, with electric field parallel to the probe-axis. This configuration mimics the focal plane of radially polarised light used in this study, wherein a large portion of the electric field is oriented in the z direction, parallel to the probe-axis.

unobservable Raman bands in the far-field spectra as discussed before, the SNR of the TERS signal, presented in parentheses in Table 3.1, decreased by about 2.8 times in water compared to air, indicating a much lower electric field enhancement at the TERS probe-apex.

The simulation results show that the maximum electric field enhancement in

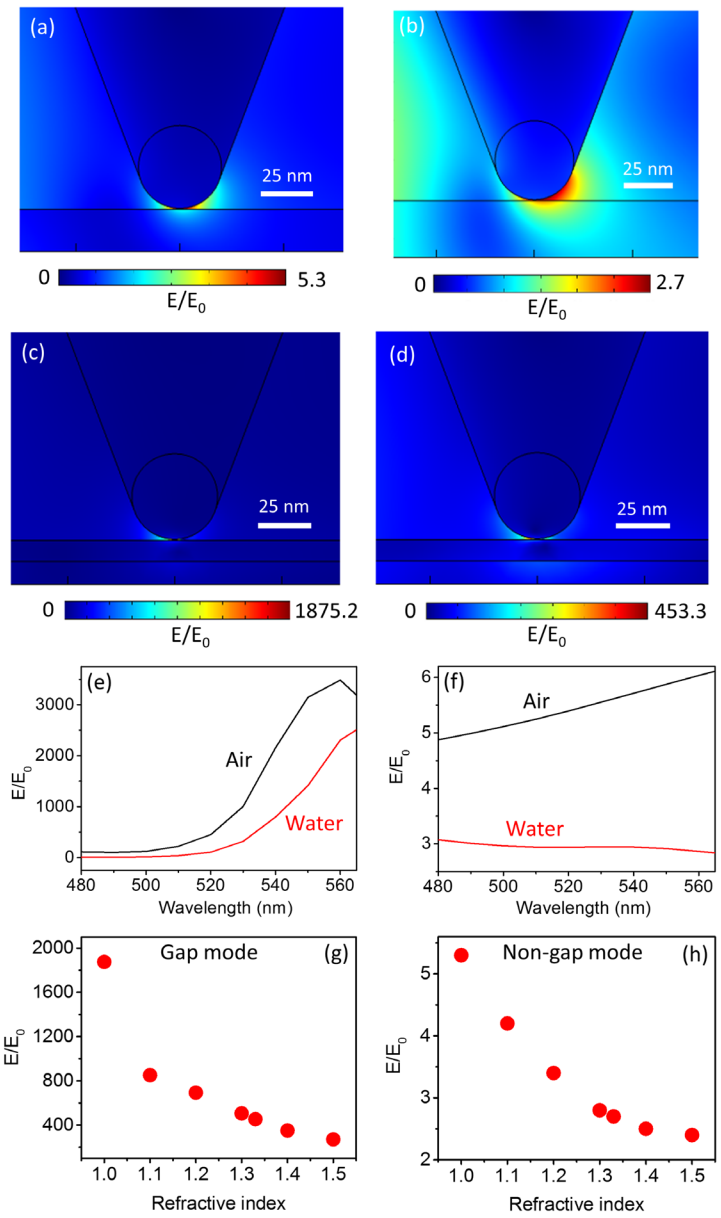

Fig. 3.8 Numerical simulation maps of the electric field enhancement at the apex of a modelled Cr-Au-Ag TERS probe in contact with a glass coverslip (non-gap mode) in (a) air and (b) water. Numerical simulation maps of electric field enhancement at the apex of a modelled TERS probe in contact with a 10 nm Au film on glass (gap mode) in (c) air and (d) water. Plots of calculated electric field enhancement at the probe-apex versus excitation laser wavelength in (e) gap and (f) non-gap modes. Plots of the calculated electric field enhancement at the probe-apex versus RI of the surrounding medium in (g) gap and (h) non-gap modes.

non-gap mode (Fig. 3.8a and 3.8b) is approximately three orders of magnitude smaller than gap mode in both air and water (Fig. 3.8c and 3.8d), which is consistent with previous experimental reports.[54] Furthermore, across the entire green light wavelength range (520 nm – 560 nm)[55] a higher electric field enhancement is revealed in air compared to water in both gap and non-gap modes, as shown in Fig. 3.8e and 3.8f, respectively. Interestingly, the decrease in the electric field enhancement from air to water was found to be smaller in non-gap mode (a factor of 1.9) compared to gap mode (a factor of 4.1). However, since the EF of our gap mode TERS measurements cannot be precisely determined, this trend could not be experimentally verified.

To gain further insights into the decrease of electric field enhancement in water compared to air, we calculated the electric field enhancement at the TERS probe-apex as a function of the RI of the surrounding medium. The electric field enhancement was found to decrease with increasing RI in both gap and non-gap modes as shown in Fig. 3.8g and 3.8h. Furthermore, a sharper drop in electric field enhancement with increasing RI was observed in gap mode compared to non-gap mode. These results are consistent with previous experimental reports in which the LSPR of Ag and Au nanoparticles was found to red-shift with an increase in local RI.[56-58] For Ag, the LSPR was observed to shift by up to 35 nm per 0.1 RI increase.[56] Since we used a 532 nm excitation laser, a red-shift of the LSPR in water (RI = 1.33) compared to air (RI = 1) would lead to a loss in electric field enhancement and hence a decrease in TERS EF as observed *via* numerical simulations and TERS experiments in this study. Therefore, this negative correlation between electric field enhancement and RI may offer a physical rationale for the loss of TERS sensitivity observed experimentally in water compared to air, in that the presence of a higher dielectric medium results in near-field optical losses due to dipolar interactions at the probe-substrate interface. Given the additional plasmonic signal enhancement associated with the metallic probe and metal substrate set-up of the gap mode, it is not surprising that the above attenuation is more pronounced in this configuration.

Note that our simulation model greatly simplifies the real TERS experimental conditions, for example by ignoring the roughness of the Ag coating on TERS probes and the radial polarisation of the excitation laser incident onto the sample in bottom illumination geometry. It is also prudent to highlight the large uncertainties associated with the experimentally determined values of EF values presented in Table 3.1, which show that nominally identical probes display significantly different properties at the nanostructured apex. Nevertheless, the simulation results exhibit the same general trend as observed experimentally for the plasmonic signal enhancement in both gap and non-gap modes, suggesting a reasonable agreement between experiment and theory.

3.3.4 Nanoscale Raman Imaging in a Liquid Environment

Finally, we performed TERS imaging in air and water using the Cr-Au-Ag coated TERS probes in order to critically compare their chemical imaging characteristics in these two environments. We used a glass coverslip decorated with SWCNTs for this purpose since the 1D nature of SWCNTs makes them convenient model structures to demonstrate high resolution imaging.[59-61] A line profile across the TERS map of a SWCNT gives a direct estimate of the size of the near-field enhancement at the TERS probe-apex[62] and the spatial resolution achieved during the imaging.[63] We note there are different interpretations of the term "spatial resolution"; for simplicity here we define it as the full width at half maximum (FWHM) of the Raman signal intensity measured across a single 1D feature. Since the lateral dimensions of the SWCNT are significantly smaller than the probe apex dimensions, the spatial resolution is governed largely by the latter. Fig. 3.9a shows an AFM topography image of SWCNTs dispersed on a glass substrate. The height profile shown in Fig. 3.9b confirm that the carbon nanotubes are indeed single-walled and are singly distributed over the sample surface. Fig. 3.9c shows the confocal Raman spectrum of the SWCNT sample exhibiting the characteristic D, G and 2D Raman bands.

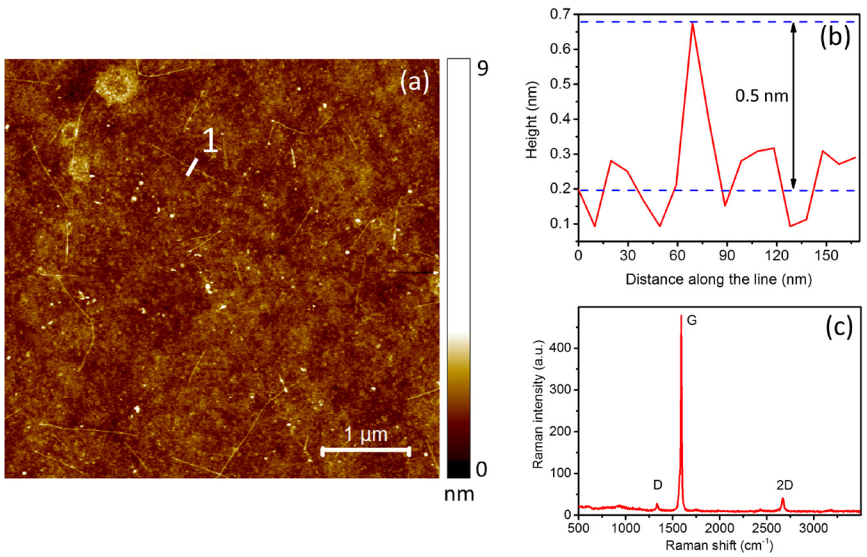

Fig. 3.9 (a) AFM topography image showing distribution of SWCNTs over a glass substrate. (b) Height profile along the line marked as 1 Fig. 3.9a. From the AFM topography image, size of SWCNTs is estimated to be 0.7 ± 0.1 nm, indicating that the carbon nanotubes are indeed single-walled and are singly distributed over the glass substrate. (c) Confocal Raman spectrum of a SWCNT measured from the sample shown in Fig. 3.9a. Integration time: 10 s, laser power at the sample: 170 µW.

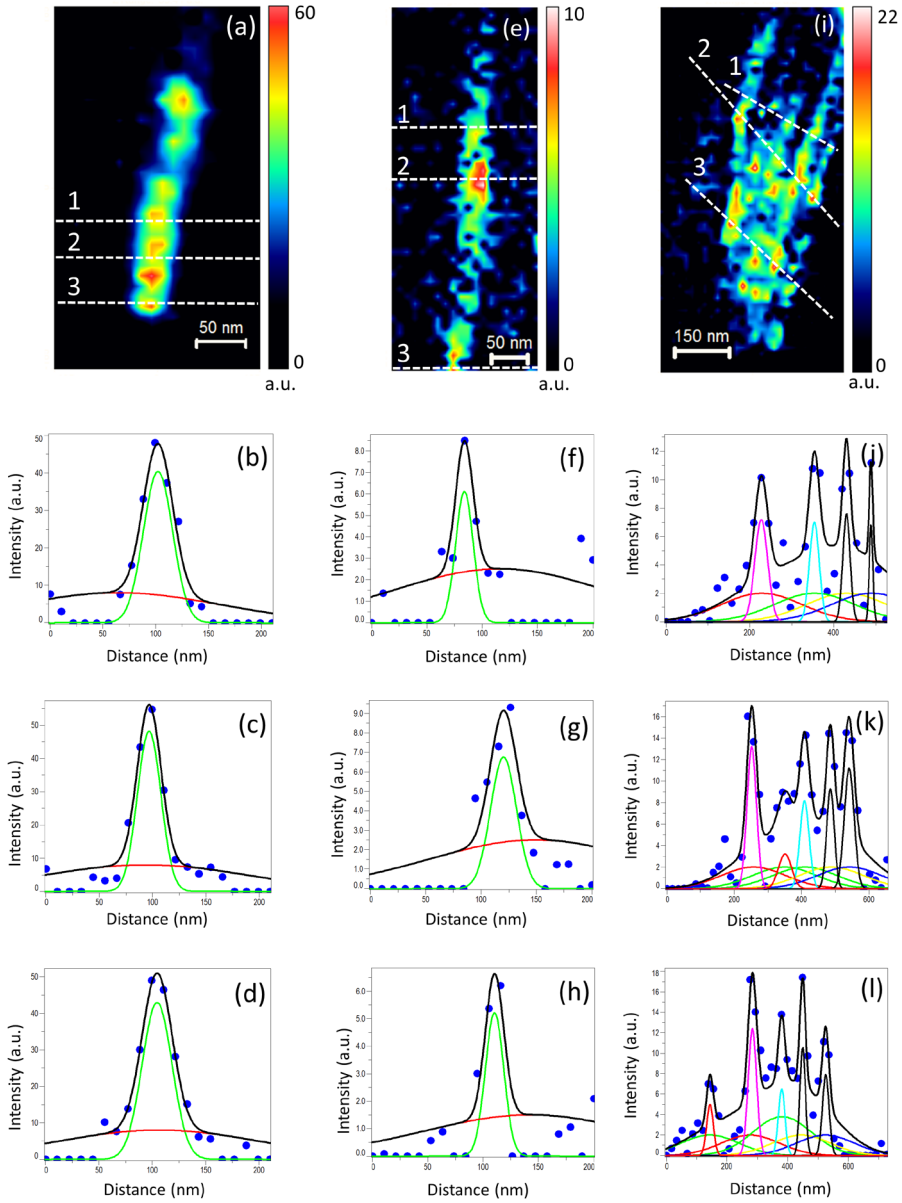

Fig. 3.10 (a), (e), (i) TERS images of SWCNTs, obtained using the 1591 cm^{-1} Raman band intensity measured in air. Integration time: 1s, nominal pixel size in Fig. 3.10a and 3.10e: 10 nm, Fig. 3.10i: 17 nm, laser power at the sample: 170 μW. Fig. 3.10a and 3.10e show TERS maps of one SWCNT, whereas a bundle of SWCNTs is mapped in Fig. 3.10i. (b) – (d), (f) – (h), (j) – (l) Intensity profiles along lines 1 – 3 marked in Fig. 3.10a, 3.10e and 3.10i, respectively along with Gaussian curves fits representing the near-field (green) and far-field (red) contributions.

High-resolution TERS images of the G band intensity (at 1591 cm^{-1}) for SWCNTs measured in air are shown in Fig. 3.10a, 3.10e and 3.10i. The G band intensity at each pixel in these images was determined from the height of a Lorentzian fit to the TERS spectrum in 1470 cm^{-1} - 1671 cm^{-1} region after linear background subtraction using a MATLAB program. To minimize fitting errors, only the pixels where Raman intensity was at least three times higher than the median

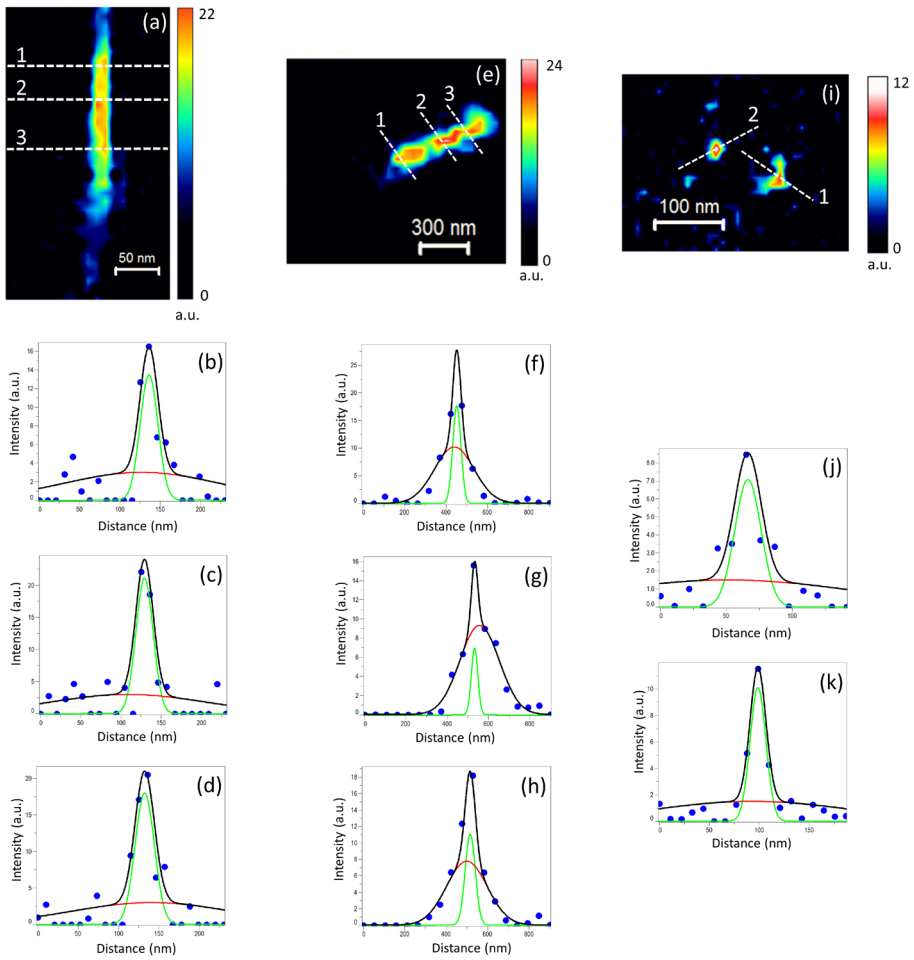

Fig. 3.11 (a), (e), (i) TERS images of SWCNTs, obtained using the 1591 cm^{-1} Raman band intensity measured in water. Integration time: 1s, nominal pixel size in Fig. 3.11a and 3.11i: 10 nm, Fig. 3.11e: 50 nm, laser power at the sample: 170 μW. Attempts at mapping the SWCNT in Fig. 3.11e with a smaller pixel size were unsuccessful due to issues with SWCNT displacement during TERS imaging. (b) – (d), (f) – (h), (j) – (k) Intensity profiles along the lines 1-3 marked in Fig. 3.11a, 3.11e and 1-2 marked in 3.11i, respectively along with Gaussian curves fits representing the near-field (green) and far-field (red) contributions. Note that the step size used for the TERS map in Fig. 3.11e is similar to the estimated spatial resolution, so the latter value should be treated with caution as the Nyquist sampling criterion is not satisfied in this case.

noise level in the chosen spectral range were fitted using a Lorentzian curve. To calculate the spatial resolution of the SWCNT TERS maps, we used the procedure reported by Roy *et al.*,[62] which separates the near-field and far-field components in an intensity profile measured across the TERS map of a SWCNT by fitting with two different Gaussian curves. All TERS maps exhibited intensity fluctuations along the length of the SWCNTs. Therefore, in order to gain a more representative estimation of the spatial resolution, we performed the Gaussian fitting procedure on three different line profiles across the TERS maps. Fig. 3.10b – 3.10d show intensity profiles across the lines marked in Fig. 3.10a fitted with two Gaussian curves representing the far-field (red) and near-field (green) contributions. The FWHM of the far-field Gaussian curve was set to 225 nm corresponding to a laser spot size of 450 nm. The near-field spatial resolution of the TERS map in Fig. 3.10a was estimated from the FWHM of the green Gaussian curves to be 28 ± 2 nm. Following the similar procedure, spatial resolution of TERS maps shown in Fig. 3.10e and 3.10i were estimated to be 22 ± 5 nm and 27 ± 4 nm, respectively. We then performed TERS imaging of SWCNTs on the same sample immersed in water, which is shown in Fig. 3.11. Fig. 3.11a and 3.11e show TERS maps of a SWCNT each, whereas Fig. 3.11i shows TERS map of a broken SWCNT on the sample. Following the same analysis procedure described above, spatial resolution of the TERS maps in Fig. 3.11a, 3.11e and 3.11i was estimated to be 26 ± 2 nm, 47 ± 11 nm and 22 ± 4 nm, respectively. A summary of the spatial resolution calculated from the TERS maps of SWCNTs in air and water is presented in Table 3.2.

The TERS images of SWCNTs in air exhibited an average spatial resolution ranging from 22 nm - 28 nm. However, TERS imaging of SWCNTs was generally found to be more challenging in water. In particular, the SWCNTs were often displaced by the TERS probe during mapping, whereas they remained stationary whilst imaging in air, suggesting a weaker interaction between the SWCNTs and the glass substrate in water. Despite this difficulty, we were successful in obtaining TERS maps of SWCNTs in water with a spatial resolution ranging from 22 nm – 58 nm. Although on average a poorer resolution was achieved in water, the difference between air and water is relatively small compared to the uncertainty in measurement. Indeed, the significantly wider spread of spatial resolution data across the water measurements reflects the practical difficulties encountered whilst performing TERS imaging in water, which may exacerbate the natural variation in imaging performance expected between TERS probes. Nevertheless, these results clearly demonstrate the feasibility of spatially resolved TERS measurements in liquid at nanometre length-scales using multi-layer metal coated TERS probes.

Furthermore, the spatial resolution estimated from these TERS images is also consistent with the lateral size of the electric field enhancement obtained from the non-gap mode numerical simulation maps in air and water (Fig. 3.8a and 3.8b).

Table 3.2 Comparison of the spatial resolution of SWCNT TERS maps measured in air and water.

	TERS map	Pixel size of TERS map (nm)	Spatial resolution (nm)	Mean spatial resolution (nm)
Air	Fig. 3.10a	10	26	28 ± 2
			29	
			28	
	Fig. 3.10e	10	19	22 ± 5
			28	
			20	
	Fig. 3.10i	17	27	27 ± 4
			31	
			23	
Water	Fig. 3.11a	10	28	26 ± 2
			25	
			26	
	Fig. 3.11e	50	46	47 ± 11
			37	
			58	
	Fig. 3.11i	10	24	22 ± 4
			19	

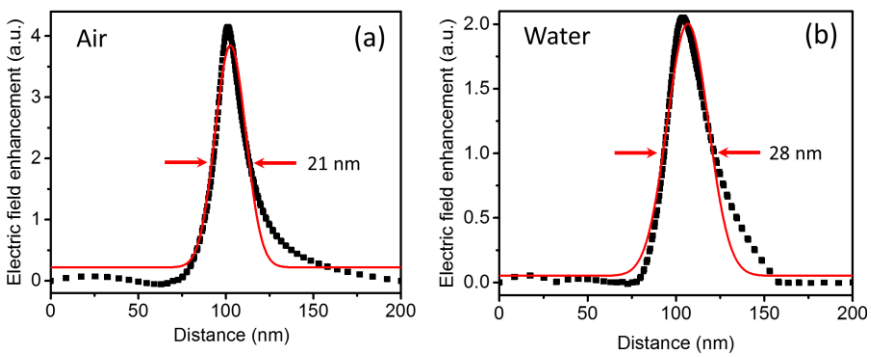

Fig. 3.12 Calculated horizontal intensity profiles of electric field enhancement beneath the tip-apex in non-gap mode numerical simulation maps shown in (a) Fig. 3.8a and (b) 3.8b along with fitted Gaussian curves. Lateral size of near-field enhancement at the tip-apex in air and water is estimated from the FWHM of the fitted Gaussian curves (red) to be 21 nm and 28 nm, respectively. The similar lateral size of the electric field enhancement in air and water indicates that a similar nanoscale spatial resolution is achievable for TERS imaging in both environments.

Horizontal line profiles measured beneath the probe-apex across these maps are shown along with Gaussian curve fits in Fig. 3.12. The lateral dimension of the electric field enhancement can be estimated from the FWHM of the fitted Gaussian curves. A rather similar FWHM in air (21 nm) and water (28 nm) suggests that although the electric field enhancement decreases in water, it remains confined to the TERS probe-apex. This also indicates that a similar lateral resolution for TERS imaging should be possible in both air and water, which is indeed substantiated by our experimental results.

3.4 Conclusions

In conclusion, we have developed robust plasmonically active TERS probes capable of performing successful TERS imaging when fully immersed in a liquid environment. Using these novel probes, we have performed TERS measurements in water in both gap and non-gap mode TERS configurations and analysed the difference in plasmonic enhancement of Raman signals with the corresponding measurements in air. Plasmonic signal enhancement was found to decrease in an aqueous environment compared to air in both gap and non-gap modes. Numerical simulations of the near-field intensity revealed a negative correlation between electric field enhancement at the TERS probe-apex and the RI of the surrounding medium, providing a physical basis for these experimental observations. Finally, we have demonstrated sub-30 nm resolution chemical mapping in a liquid environment using TERS for the first time. It has been shown that the TERS spatial resolution for SWCNTs measured in water can be similar to that observed in air, although experimental challenges in liquid lead to increased experimental variability. This work is expected to significantly broaden the application of AFM-TERS across scientific disciplines such as heterogeneous catalysis, electrochemistry and cellular biology, wherein non-destructive and label-free chemical mapping of nanostructured solid-liquid interfaces presents a key measurement challenge.

References

1. I. L. C. Buurmans and B. M. Weckhuysen, *Nat. Chem.*, 2012, **4**, 873-886.
2. B. M. Weckhuysen, *In-situ Spectroscopy of Catalysts*, American Scientific Publishers, Stevenson Ranch, 2004.
3. M. J. Weaver and X. Gao, *Annu. Rev. Phys. Chem.*, 1993, **44**, 459-494.
4. Y. F. Dufrêne, *Nat. Rev. Microbiol.*, 2004, **2**, 451 - 460.
5. T. Deckert-Gaudig, A. Taguchi, S. Kawata and V. Deckert, *Chem. Soc. Rev.*, 2017, **46**, 4077-4110.
6. N. Kumar, S. Mignuzzi, W. Su and D. Roy, *EPJ Tech. Instrum.*, 2015, **2**, 9.
7. P. Verma, *Chem. Rev.*, 2017, **117**, 6447-6466.

8. A. Hartschuh, *Angew. Chem. Int. Ed.*, 2008, **47**, 8178-8191.
9. R. M. Stockle, Y. D. Suh, V. Deckert and R. Zenobi, *Chem. Phys. Lett.*, 2000, **318**, 131-136.
10. N. Hayazawa, Y. Inouye, Z. Sekkat and S. Kawata, *Opt. Commun.*, 2000, **183**, 333-336.
11. M. S. Anderson, *Appl. Phys. Lett.*, 2000, **76**, 3130-3132.
12. N. Kumar, A. Zoladek-Lemanczyk, A. A. Guilbert, W. Su, S. M. Tuladhar, T. Kirchartz, B. C. Schroeder, I. McCulloch, J. Nelson and D. Roy, *Nanoscale*, 2017, **9**, 2723-2731.
13. E. M. van Schrojenstein Lantman, T. Deckert-Gaudig, A. J. G. Mank, V. Deckert and B. M. Weckhuysen, *Nat. Nanotechnol.*, 2012, **7**, 583-586.
14. N. Kumar, B. Stephanidis, R. Zenobi, A. Wain and D. Roy, *Nanoscale*, 2015, **7**, 7133-7137.
15. J.-H. Zhong, X. Jin, L. Meng, X. Wang, H.-S. Su, Z.-L. Yang, C. T. Williams and B. Ren, *Nat. Nanotechnol.*, 2017, **12**, 132-136.
16. B. S. Yeo, E. Amstad, T. Schmid, J. Stadler and R. Zenobi, *Small*, 2009, **5**, 952-960.
17. N. Kumar, M. M. Drozdz, H. Jiang, D. M. Santos and D. J. Vaux, *Chem. Commun.*, 2017, **53**, 2451-2454.
18. S. Berweger, C. C. Neacsu, Y. Mao, H. Zhou, S. S. Wong and M. B. Raschke, *Nat. Nanotechnol.*, 2009, **4**, 496-499.
19. A. Lucia, O. A. Cacioppo, E. Iulianella, L. Latessa, G. Moccia, D. Passeri and M. Rossi, *Appl. Phys. Lett.*, 2017, **110**, 103105.
20. S. Mignuzzi, N. Kumar, B. Brennan, I. S. Gilmore, D. Richards, A. J. Pollard and D. Roy, *Nanoscale*, 2015, **7**, 19413-19418.
21. W. Su, N. Kumar, N. Dai and D. Roy, *Chem. Commun.*, 2016, **52**, 8227-8230.
22. W. Su, N. Kumar, S. Mignuzzi, J. Crain and D. Roy, *Nanoscale*, 2016, **8**, 10564-10569.
23. Y. Okuno, Y. Saito, S. Kawata and P. Verma, *Phys. Rev. Lett.*, 2013, **111**, 216101.
24. M. Boehmler, Z. Wang, A. Myalitsin, A. Mews and A. Hartschuh, *Angew. Chem. Int. Ed.*, 2011, **50**, 11536-11538.
25. R. Zhang, Y. Zhang, Z. C. Dong, S. Jiang, C. Zhang, L. G. Chen, L. Zhang, Y. Liao, J. Aizpurua, Y. Luo, J. L. Yang and J. G. Hou, *Nature*, 2013, **498**, 82-86.
26. A. B. Zrimsek, N. Chiang, M. Mattei, S. Zaleski, M. O. McAnally, C. T. Chapman, A.-I. Henry, G. C. Schatz and R. P. Van Duyne, *Chem. Rev.*, 2016, **117**, 7583 - 7613.
27. M. Sun, Z. Zhang, H. Zheng and H. Xu, *Sci. Rep.*, 2012, **2**, 647.
28. E. A. Pozzi, M. D. Sonntag, N. Jiang, N. Chiang, T. Seideman, M. C. Hersam and R. P. Van Duyne, *J. Phys. Chem. Lett.*, 2014, **5**, 2657-2661.
29. E. A. Pozzi, G. Goubert, N. Chiang, N. Jiang, C. T. Chapman, M. O. McAnally, A.-I. Henry, T. Seideman, G. C. Schatz and M. C. Hersam, *Chem. Rev.*, 2016, **117**, 4961-4982.
30. T. Schmid, B. S. Yeo, G. Leong, J. Stadler and R. Zenobi, *J. Raman Spectrosc.*, 2009, **40**, 1392-1399.
31. A. Nakata, T. Nomoto, T. Toyota and M. Fujinami, *Anal. Sci.*, 2013, **29**, 865-869.
32. J. D. Scherger and M. D. Foster, *Langmuir*, 2017, **33**, 7818-7825.
33. N. Martín Sabanés, L. M. Driessen and K. F. Domke, *Anal. Chem.*, 2016, **88**, 7108-7114.
34. T. Touzalin, A. L. Dauphin, S. Joiret, I. T. Lucas and E. Maisonhaute, *Phys. Chem. Chem. Phys.*, 2016, **18**, 15510-15513.
35. Z.-C. Zeng, S.-C. Huang, D.-Y. Wu, L.-Y. Meng, M.-H. Li, T.-X. Huang, J.-H. Zhong, X. Wang, Z.-L. Yang and B. Ren, *J. Am. Chem. Soc.*, 2015, **137**, 11928-11931.
36. D. Kurouski, M. Mattei and R. P. Van Duyne, *Nano Lett.*, 2015, **15**, 7956-7962.
37. X. Wang, J.-H. Zhong, M. Zhang, Z. Liu, D.-Y. Wu and B. Ren, *Anal. Chem.*, 2015, **88**, 915-921.
38. T. Touzalin, S. Joiret, E. Maisonhaute and I. T. Lucas, *Anal. Chem.*, 2017, **89**, 8974-8980.
39. M. Mattei, G. Kang, G. Goubert, D. V. Chulhai, G. C. Schatz, L. Jensen and R. P. Van Duyne, *Nano Lett.*, 2016, **17**, 590-596.
40. D. Mattox, *Thin Solid Films*, 1973, **18**, 173-186.
41. M. George, W. Glaunsinger, T. Thundat and S. Lindsay, *Thin Solid Films*, 1990, **189**, 59-72.

42. R. Nyquist, C. Putzig, M. Leugers, R. McLachlan and B. Thill, *Appl. Spectrosc.*, 1992, **46**, 981-987.
43. N. Kumar, A. Rae and D. Roy, *Appl. Phys. Lett.*, 2014, **104**, 123106.
44. T. Schmid, A. Messmer, B. S. Yeo, W. Zhang and R. Zenobi, *Anal. Bioanal. Chem.*, 2008, **391**, 1907-1916.
45. J. Stadler, T. Schmid and R. Zenobi, *Nano Lett.*, 2010, **10**, 4514-4520.
46. D. Richards, R. G. Milner, F. Huang and F. Festy, *J. Raman Spectrosc.*, 2003, **34**, 663-667.
47. B. Pettinger, K. F. Domke, D. Zhang, G. Picardi and R. Schuster, *Surf. Sci.*, 2009, **603**, 1335-1341.
48. L. G. Cancado, A. Jorio, A. Ismach, E. Joselevich, A. Hartschuh and L. Novotny, *Phys. Rev. Lett.*, 2009, **103**, 186101.
49. F. Benz, C. Tserkezis, L. O. Herrmann, B. De Nijs, A. Sanders, D. O. Sigle, L. Pukenas, S. D. Evans, J. Aizpurua and J. J. Baumberg, *Nano Lett.*, 2014, **15**, 669-674.
50. J. Kalbacova, R. D. Rodriguez, V. Desale, M. Schneider, I. Amin, R. Jordan and D. R. Zahn, *Nanospectroscopy*, 2014, **1**, 12-18.
51. W. Zhang, T. Schmid, B.-S. Yeo and R. Zenobi, *J. Phys. Chem. C*, 2008, **112**, 2104-2108.
52. R. L. Sobocinski and J. E. Pemberton, *Langmuir*, 1988, **4**, 836-845.
53. H. Liu, Y. Sun, Z. Jin, L. Yang and J. Liu, *Chem. Sci.*, 2013, **4**, 3490-3496.
54. S. Berweger and M. B. Raschke, *Anal. Bioanal. Chem.*, 2010, **396**, 1613-1613.
55. C. F. Bohren and E. E. Clothiaux, *Fundamentals of Atmospheric Radiation: An Introduction with 400 Problems*, Wiley-VCH, Weinheim, 2006.
56. J. J. Mock, D. R. Smith and S. Schultz, *Nano Lett.*, 2003, **3**, 485-491.
57. M. M. Miller and A. A. Lazarides, *J. Phys. Chem. B*, 2005, **109**, 21556-21565.
58. K. L. Kelly, E. Coronado, L. L. Zhao and G. C. Schatz, *J. Phys. Chem. B*, 2003, **107**, 668-677.
59. A. Hartschuh, E. J. Sanchez, X. S. Xie and L. Novotny, *Phys. Rev. Lett.*, 2003, **90**, 095503.
60. A. Weber-Bargioni, A. Schwartzberg, M. Cornaglia, A. Ismach, J. J. Urban, Y. Pang, R. Gordon, J. Bokor, M. B. Salmeron, D. F. Ogletree, P. Ashby, S. Cabrini and P. J. Schuck, *Nano Lett.*, 2011, **11**, 1201-1207.
61. D. Roy and C. Williams, *J. Vac. Sci. Technol. A*, 2010, **28**, 472-475.
62. D. Roy, J. Wang and C. Williams, *J. Appl. Phys.*, 2009, **105**, 013530.
63. T.-A. Yano, P. Verma, Y. Saito, T. Ichimura and S. Kawata, *Nat. Photonics*, 2009, **3**, 473-477.

Chapter 4

In Situ Nanoscale Mapping of Catalytic Reactions in the Liquid Phase using Tip-enhanced Raman Spectroscopy

Abstract

Tip-enhanced Raman spectroscopy (TERS) is a promising technique for non-destructive and label-free topographical and chemical imaging at the nanoscale. However, its scope for *in situ* characterisation of catalytic reactions in the liquid phase has remained limited due to the lack of durable and chemically inert plasmonically active TERS probes. In this Chapter, we present novel zirconia protected TERS probes with three orders of magnitude increase in lifetime under ambient conditions compared to unprotected silver coated probes, together with a high stability in liquid media. Using these probes, we demonstrate spatially resolved characterisation of a photocatalytic reaction at the nanoscale within an aqueous environment, employing plasmon-assisted oxidation of *p*-aminothiophenol as a model reaction. The reported improved lifetime and stability of probes within a liquid environment extend the scope of TERS as a nanoanalytical tool not only to heterogeneous catalysis, but also to a range of scientific disciplines in which dynamic solid-liquid interfaces play a defining role.

This Chapter is based on: N. Kumar, C. S. Wondergem, A. J. Wain and B. M. Weckhuysen, 2018, submitted for publication.

4.1 Introduction

Heterogeneous catalysis is the mainstay of the modern chemical industry, enabling efficient chemical conversion in over 80% of all industrial processes and contributing to over 35% of the global GDP.[1] Rational design of novel catalyst materials with tailored properties relies on the identification of active sites at reacting solid-liquid and solid-gas interfaces, which are typically spatially heterogeneous, in order to comprehend structure-performance relationships.[2, 3] However, conventional analytical techniques, such as Raman, infrared (IR), ultraviolet-visible and fluorescence spectroscopies, often lack the required sensitivity and spatial resolution to achieve this ambitious goal.[4, 5] In recent years, tip-enhanced Raman spectroscopy (TERS) has emerged as a potential solution to this challenge, enabling non-destructive topographical and molecular imaging of surfaces at the nanoscale.[6, 7] This technique has been successfully used in a wide range of research areas including biology,[8] polymer blends,[9] semiconductors,[10] crystalline materials,[11] solar energy conversion,[12] nanomaterials research[13-15] and single molecule imaging.[16, 17] As discussed in Chapter 1, in TERS, a metallic scanning probe microscopy (SPM) probe positioned within the excitation laser spot of a Raman microscope (Fig. 4.1), enhances the incident electric field by several orders of magnitude *via* a combination of localised surface plasmon resonance (LSPR) and lightening rod effect and confines the field enhancement to a region similar in size to the probe-apex. This near-field approach significantly improves the sensitivity of Raman microscopy and pushes its spatial resolution far beyond the diffraction limit.

Despite the advantages of high spatial resolution and rich chemical information offered by TERS,[2, 18, 19] only a handful of TERS studies of catalytic reactions have been reported so far.[20-26] Furthermore, the majority of such studies have been carried out in ambient air or ultra-high vacuum, with only a few in liquid environments, mostly limited to point spectroscopy measurements.[27-32] Two-dimensional (2D) nanoscale chemical imaging of catalytic reaction in liquids represents a key challenge, but has not been achieved using TERS, primarily due to the chemical reactivity,[21, 33] short lifetime[34-37] and/or instability of TERS probes in liquids.[27, 32] The chemical reactivity of metallic TERS probes is a particularly important consideration when studying catalysis *in situ*, due to the potential for interference in the reaction under investigation. To address this issue, as well as extend the lifetime of metallic TERS probes, the use of an ultrathin coating of dielectric material such as alumina[22, 38] and silica[39] as a protective layer has been reported. However, alumina and silica are not stable over the entire pH range,[40] limiting the conditions in which such TERS probes could be used. Furthermore, both alumina and silica coatings only increased the lifetime of TERS probes to approximately one month and although some increased stability in liquids was

observed, no TERS mapping was performed.

In this Chapter, we present novel atomic force microscopy (AFM)-TERS probes with a multilayer metal coating protected using an ultrathin layer of zirconia (ZrO_2) that successfully overcome the key limitations of short lifetime, chemical inertness and instability in a liquid environment. ZrO_2 offers excellent catalytic support properties for several reactions[41, 42] and stability over the entire pH range[40] making it especially suitable for investigating heterogeneous catalytic reactions under a wide range of conditions. Furthermore, using the novel TERS probes, we demonstrate the feasibility of mapping of a catalytic reaction over a heterogeneous catalyst surface in water with nanoscale spatial resolution, employing the photocatalytic oxidation of *p*-aminothiophenol (pATP) to *p*,*p*'-dimercaptoazobenzene (DMAB) as a model reaction (Fig. 4.1).[22, 43]

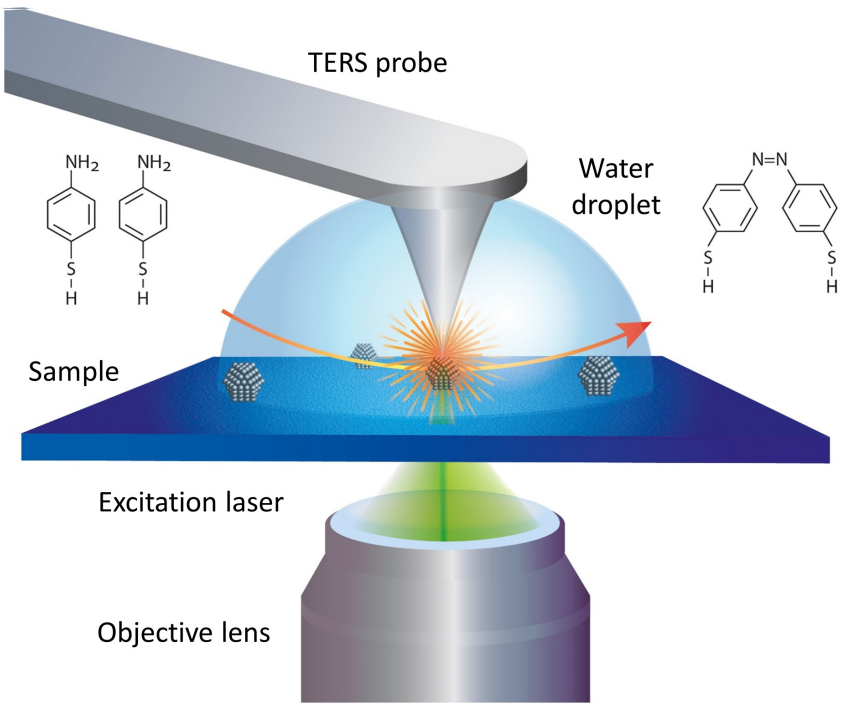

Fig. 4.1 Schematic diagram of the experimental TERS setup used in this work for spatially resolved mapping of plasmon-assisted oxidation of pATP → DMAB over a heterogeneous Ag substrate within an aqueous environment.

4.2 Experimental

4.2.1 TERS System

A bespoke transmission mode TERS system was used in this work consisting of an AFM (AIST-NT, USA) positioned on top of an inverted confocal Raman microscope (Nikon, Japan), which was attached to a Raman spectrometer (HORIBA Scientific, France) fitted with a charged coupled device detector (Andor Technology, UK). All far-field and TERS measurements were performed using a radially polarised 532 nm excitation laser that was focussed on the sample using a 100x, 1.49 NA, oil immersion objective lens (Nikon, Japan). The diameter of the excitation laser spot at the sample was estimated from the far-field optical spatial resolution measured using a line Raman map across a SWCNT to be ≈ 450 nm. TERS measurements were carried out using contact mode AFM feedback. A laser power of 50 μW - 117 μW at the sample was used for the far-field and TERS measurements. For TERS measurements, a TERS probe was brought in contact with the sample surface and aligned with the excitation laser. Thereafter, the sample was moved in a raster fashion between the TERS probe and objective lens, whilst a TERS spectrum was measured at each pixel. To map pATP → DMAB at the TERS probe-apex, a TERS probe was aligned with the laser spot first. Then, the objective lens was moved in a raster fashion around the TERS probe whilst keeping the sample and the probe stationary and measuring a Raman spectrum at each pixel. All TERS spectra presented in this work comprise sum of Raman signals generated in the near-field as well as far-field. Data analysis was performed using OriginPro, SPIP™, AIST-NT SPM, MATLAB and LabSpec 5 softwares. All TERS, SERS and far-field Raman spectra were smoothened and vertically shifted for a clearer visualisation of the vibrational bands.

4.2.2 Sample Preparation

PEDOT:PSS thin film sample was prepared by spin coating an aqueous solution of PEDOT:PSS (Heraeus Precious Metals GmbH & Co., Germany) onto a glass coverslip (thickness number: 1.5) at 2000 revolutions per minute for 2 minutes under Ar atmosphere. Heterogeneous Ag substrate was prepared by thermal deposition of 10 nm Ag (99.99 % purity, Advent Research Materials, UK) on a glass coverslip at 10^{-6} mbar pressure. pATP (97 %, purity, Sigma Aldrich, UK,) self-assembled monolayer (SAM) was prepared by immersing the Ag substrate in 10 mM pATP solution in ethanol (99.99 % purity, Fisher Scientific, UK) for 2 hours (h). The pATP functionalised Ag substrate was subsequently rinsed with copious amount of ethanol and deionised water to remove any surface residuals.

4.2.3 Transmission Electron Microscopy

Transmission electron microscopy (TEM) measurements were performed on a Talos F200X (FEI) electron microscope operating at 200 keV. Each TERS probe

was mounted on a high tilt holder and its apex was measured at 71° angle. TEM images were analysed using iTEM 5.0 software.

4.2.4 Preparation of TERS Probes

TERS probes were prepared in two stages. First, a multilayer coating of 3 nm Cr, 10 nm Au and 100 nm Ag was deposited on commercial AFM probes (MikroMasch, USA) using thermal evaporation at a pressure of 10^{-6} mbar. The average apex diameter of the TERS probes was estimated from the scanning electron microscopy (SEM) measurements to be ≈ 50 nm. At the second stage, a thin layer of ZrO_2 was coated on top of the multilayer metal coated TERS probes using the following three step procedure. A schematic diagram of the coating procedure is presented in Fig. 4.2.

Step 1. (3-aminopropyl)trimethoxysilane (APTMS) was adsorbed on the Ag surface of metal coated TERS probes by immersing them in 8 μM solution of APTMS in MilliPore water (resistivity 18.2 MΩ cm) for 15 minutes at room temperature.

Step 2. Immersion of the APTMS functionalised TERS probes in 2.5 mM zirconium (IV) propoxide solution in 1-propanol resulted in the condensation of the ZrO_2 precursor. APTMS serves as an anchor for ZrO_2 growth. In order to achieve a thin, uniform, pinhole free coating, the solution was placed in a 3:1 ice:NaCl bath (-18°C) in order to slow down the reaction rate. The reaction temperature was found to be a critical factor affecting the growth of ZrO_2 layer. See Fig. 4.3 for a comparison of ZrO_2 coating performed at different temperatures on Au nanoparticles.

Step 3. The ZrO_2-protected probes were washed by dipping them alternately in 1-propanol, MilliPore water, 1-propanol, MilliPore water, ethanol, MilliPore water and ethanol.

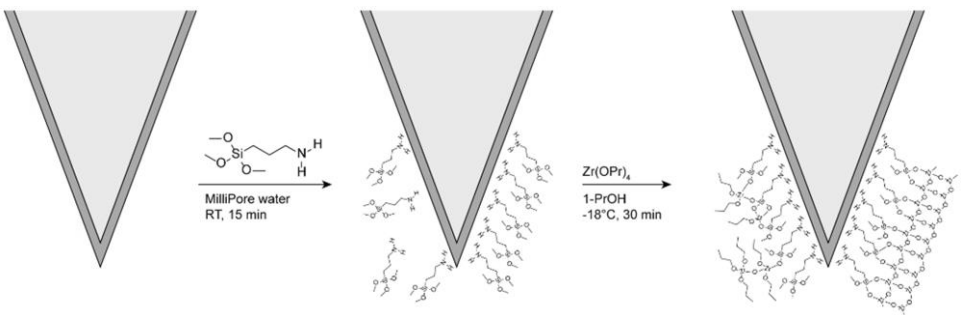

Fig. 4.2 Schematic diagram illustrating the procedure for producing ultrathin ZrO_2 layer over Ag coating of TERS probes.

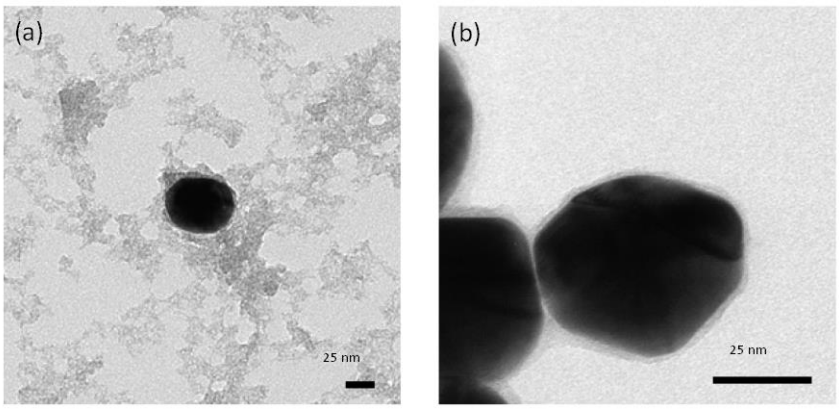

Fig. 4.3 (a) TEM image of a Au nanoparticle subjected to the ZrO_2 coating procedure at room temperature. A rapid reaction rate results in an uncontrolled nucleation and growth of ZrO_2 throughout the sample. (b) TEM image of Au nanoparticles subjected to the ZrO_2 coating procedure at -18°C using 3:1 ice:NaCl bath. At -18°C, a slow reaction rate yields a smooth and pinhole free ZrO_2 layer at the surface of Au nanoparticles.

ZrO_2 coating was found to be highly stable in different pH environments as shown in Fig. 4.4.

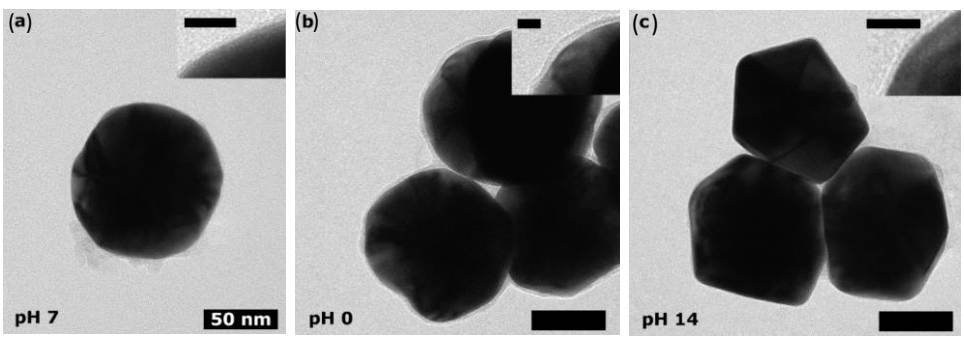

Fig. 4.4 Au@ZrO_2 nanoparticles were prepared following the method described above. After the washing steps the NPs were redispersed in solutions with different pH for 30 minutes – 45 minutes and subsequently the stability of the ZrO_2 layer was assessed using TEM. (a) TEM image of a reference Au@ZrO_2 nanoparticle dispersed in a solution of pH ≈7. (b) TEM image of Au@ZrO_2 nanoparticles redispersed in a solution of pH 0 (1 M HCl in MilliPore water). (c) TEM image of Au@ZrO_2 nanoparticles redispersed in a solution of pH 14 (1 M NaOH in MilliPore water). Scale bars: 50 nm; scale bars for insets: 10 nm. The Au nanoparticles are found to be fully covered with a ZrO_2 layer after exposure to both pH 0 and pH 14 environments, demonstrating the high stability of ZrO_2 coating.

Furthermore, ZrO_2 coating exhibited high stability in an aqueous environment over a very long period of time as shown in Fig. 4.5.

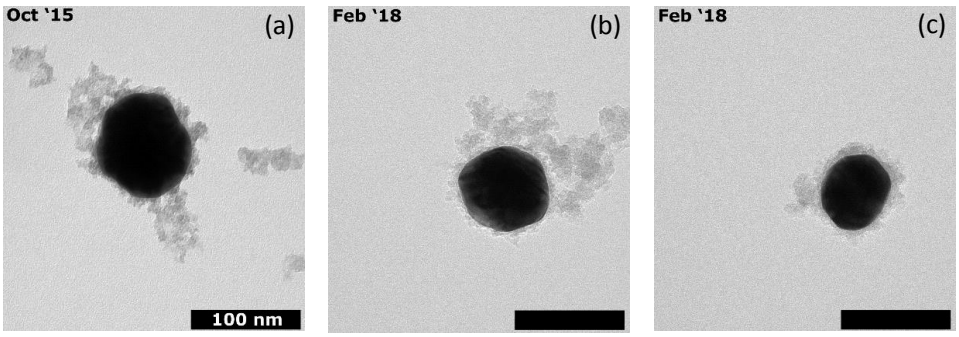

Fig. 4.5 Au@ZrO_2 nanoparticles prepared following the unoptimised method described in Fig. 4.3. Instead of carrying out the coating at -18°C, room temperature was used, resulting in uncontrolled ZrO_2 growth. (a) TEM image of a Au@ZrO_2 nanoparticle immediately after synthesis. (b), (c) TEM images of two different Au@ZrO_2 nanoparticles from the same batch as Fig. 4.5a after storage in water at room temperature for 2 years and 5 months. All scale bars: 100 nm. No significant change in the ZrO_2 coating was observed, demonstrating high stability within an aqueous environment over a long period of time.

Finally, ZrO_2 coating on Ag coated TERS probes was found to be structurally intact after TERS measurements in an aqueous environment as shown in Fig. 4.6.

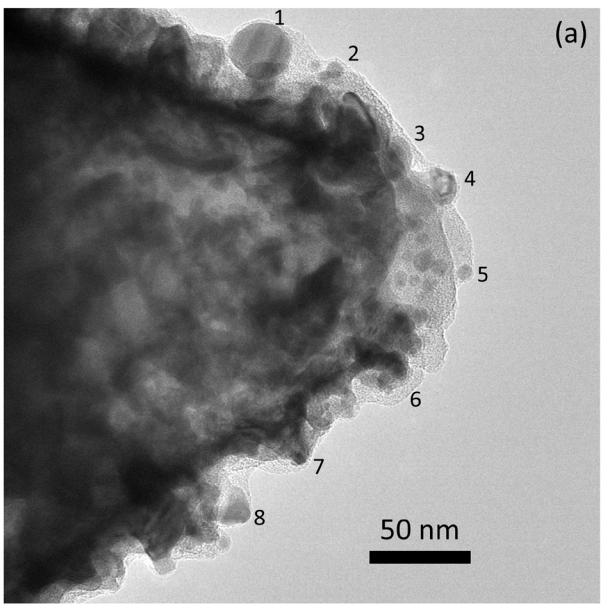

(b)

Location of zirconia coating	Thickness (nm)
1	1.4 ± 0.2
2	1.5 ± 0.2
3	2.2 ± 0.1
4	1.0 ± 0.3
5	1.2 ± 0.4
6	5.3 ± 0.4
7	1.8 ± 0.7
8	1.4 ± 0.2

Fig. 4.6 (a) TEM image of a ZrO_2-protected TERS probe-apex after being used for continuous TERS measurements in water for ≈ 2 h. (b) Average thickness of ZrO_2 coating measured using iTEM 5.0 software at the locations marked as 1 - 8 in Fig. 4.6a. The thickness of the ZrO_2 layer on the Ag varies from 1 nm - 5 nm. This demonstrates the robustness and structural stability of ZrO_2 coating during the course of TERS measurements within a liquid environment.

4.3 Results and Discussion

4.3.1 Extending Plasmonic Lifetime of TERS Probes using ZrO_2 Coating

As described in the previous section, the novel ZrO_2 coating procedure produced a pinhole free layer of ZrO_2 with a thickness of 1 nm - 5 nm on Ag coated TERS probes (Fig. 4.6). The ZrO_2 coating was also found to be highly stable over the entire pH range (Fig. 4.4), after > 2 years of storage in an aqueous environment (Fig. 4.5) and during the course of continuous TERS measurements in water (Fig. 4.6). The lifetime of ZrO_2-protected TERS probes was compared with the unprotected (Ag coated) TERS probes using a poly(3,4-ethylenedioxythiophene) :poly(styrenesulfonate) (PEDOT:PSS) thin film as a test sample. Plasmonic enhancement of a TERS probe can be monitored using the ratio of Raman signal intensity in the near-field (plasmonically enhanced electric field at a TERS probe-apex) and far-field (electric field in the entire excitation laser spot), which is known as "contrast" and defined as follows[44]

$$Contrast = \frac{I_{TERS}}{I_{FF}} - 1 \qquad (4.1)$$

where, I_{TERS} and I_{FF} are the intensity of a Raman band with the TERS probe in contact and retracted from the sample, respectively. Time-series TERS spectra recorded using unprotected and ZrO_2-protected TERS probes stored in ambient air are shown in Fig. 4.7a and 4.7b, respectively. Contrast was determined using the intensity of 1454 cm^{-1} PEDOT:PSS band ($\nu_{sym,C\alpha=C\beta}$) and is plotted in Fig. 4.7c and 4.7d, for the unprotected and protected probes, respectively. The near-field signal intensity of a fresh unprotected TERS probe is found to be almost 3× higher than the far-field signal, indicating a strong plasmonic enhancement of the electric field at the probe-apex. However, the TERS contrast decreases rapidly by 50% of its initial value (half-life) within 4.5 h due to the surface oxidation of the Ag coating in air.[34] After a rapid initial decline, the contrast decreases rather gradually by 75% in 10 h, eventually reaching zero after 170 h of exposure to air, indicating a complete loss of plasmonic signal enhancement.

On the other hand, although the ZrO_2-protected TERS probes exhibit a decrease in contrast of almost 50% compared to the unprotected probes (after 2 days of preparation), they show a much higher plasmonic stability; even after 140 days of exposure to the ambient environment, the TERS contrast decreased by only 43%, indicating that the plasmonic sensitivity for TERS measurements is largely preserved. The pinhole-free ZrO_2 layer likely blocks contact of the Ag coating with oxygen and moisture present in the surroundings, thereby preventing plasmonic degradation.[34] From extrapolation of the time-series plot in Fig. 4.7d the half-life of the ZrO_2-protected TERS probes is estimated to be over 160 days. This corresponds

to more than an 850× increase in lifetime compared to unprotected probes. To the best of our knowledge, this is the longest lifetime of any TERS probe stored under ambient conditions reported to date.

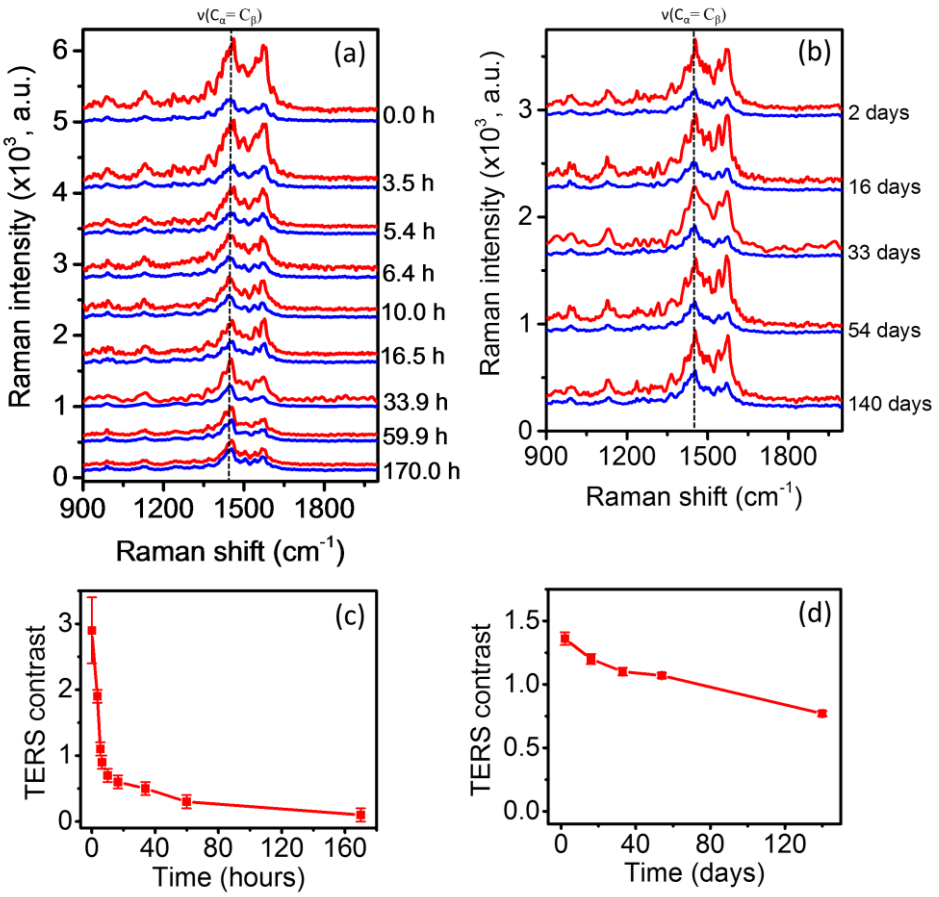

Fig. 4.7 Time-series TERS (red) and far-field Raman (blue) spectra measured from a PEDOT:PSS thin film on glass after exposing (a) unprotected TERS probes for 0 h - 170 h and (b) ZrO_2-protected TERS probes for 2 days – 140 days to the ambient environment. Integration time: 30 s. Laser power at the sample: 50 µW. Plots of TERS contrast versus exposure time of TERS probes to the ambient environment for the TERS and far-field Raman measurements presented in (c) Fig. 4.7a and (d) Fig. 4.7b. Contrast was calculated using Equation 4.1 from the intensity of 1454 cm^{-1} PEDOT:PSS band, which was determined from Lorentzian fitting of Raman bands in the 1313 cm^{-1} - 1721 cm^{-1} region after linear background subtraction.

Furthermore, unlike STM-TERS, which is limited by the essential requirement of a conductive substrate, the novel ZrO_2-protected TERS probes open

up the possibilities of nanoscale chemical mapping of almost any sample surface using an AFM-TERS setup, thereby significantly expanding the scope of TERS measurements.

4.3.2 Nanoscale Mapping of a Catalytic Reaction within a Liquid Environment

We next performed spatially resolved characterisation of a catalytic reaction at the nanoscale within an aqueous environment using the ZrO_2-protected TERS probes. For this study, we selected the photocatalytic oxidation of pATP → DMAB as model reaction (Fig. 4.1) due to the ease of monitoring using the distinct Raman bands of the azo group of DMAB, appearing in the 1140 cm^{-1} - 1500 cm^{-1} region.[43, 45] pATP → DMAB is a plasmon-assisted reaction wherein hot electrons generated *via* LSPR of metal nanoparticles cause dissociation of adsorbed oxygen under ambient conditions, facilitating oxidative dimerisation.[46] On a plasmonic metal substrate, nanoparticles exhibiting a stronger LSPR with the excitation laser are expected to act as more active catalysts. Therefore, we used a SAM of pATP molecules on a heterogeneous Ag substrate containing nanostructures varying from 1 nm - 9 nm in height shown in Fig. 4.8a and 4.8b as the test sample to map pATP → DMAB within a liquid environment. The Ag substrate was surface-enhanced Raman spectroscopy (SERS) active with the 532 nm excitation laser. Characteristic a_g Raman bands of DMAB at 1142 cm^{-1} (β_{C-H}), 1390 cm^{-1} ($\nu_{N=N}$) and 1437 cm^{-1} ($\nu_{N=N}$) could be clearly observed in the SERS spectrum of pATP adsorbed on the Ag substrate, indicating conversion to DMAB. A detailed comparison of the SERS and Raman spectra of pATP is presented in Fig. 4.8c.

Interestingly, compared to the SERS measurements in air, a 210× stronger signal was observed in water as shown in Fig. 4.9. This is in contrast to previous reports where far-field Raman signal of molecular SAMs on Au was found to decrease by a factor of > 3 in a liquid environment compared to air due to laser focus aberrations.[24, 32] A similar loss of optical coupling in water was also observed in our TERS system during far-field Raman measurements.[32] However, for the pATP SAM on the heterogeneous Ag substrate, a higher SERS signal intensity in water compared to air suggests that the aqueous environment likely enables diffusion of pATP molecules into the plasmonically active sites over the heterogeneous Ag substrate leading to a higher pATP → DMAB conversion within the confocal probe area. The lateral diffusion of pATP molecules over the Ag substrate could take place either before SERS measurements due to the dissolution of loosely bound/unbound pATP molecules in water, or during SERS measurements due to the local depletionof pATP during pATP → DMAB. However, the SERS signal intensity was found to be stable over time in both air and water. Another possible reason for a relatively higher

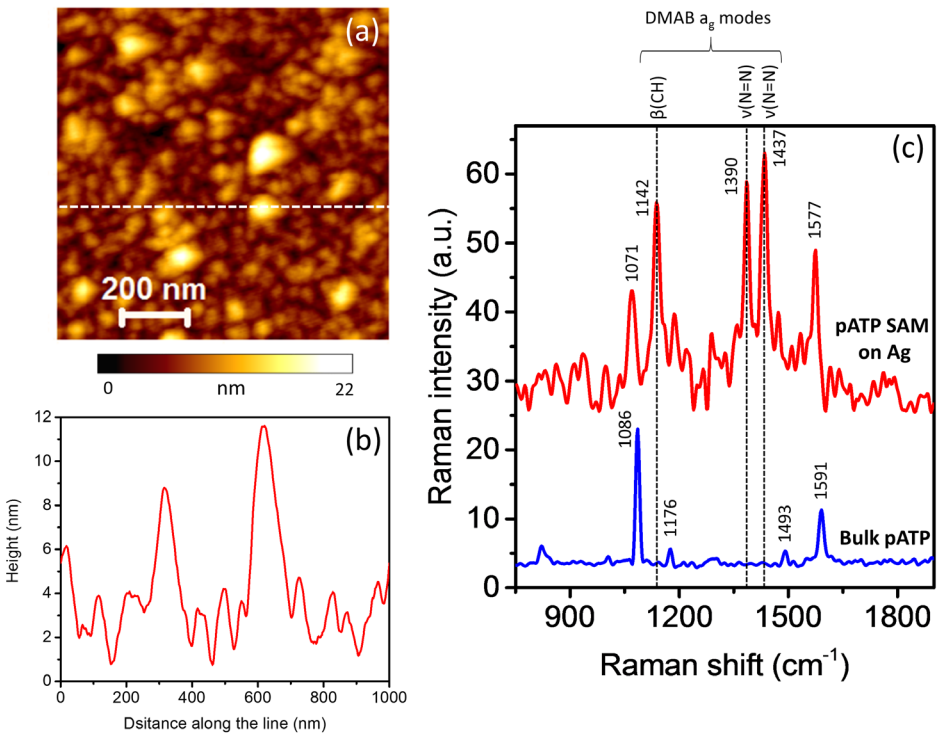

Fig. 4.8 (a) AFM topography image of pATP functionalised heterogeneous Ag substrate used for mapping pATP → DMAB using TERS in this work. (b) Height profile along the line marked in Fig. 4.8a showing size variation of Ag nanostructures on the substrate. Along the line, the height of the Ag nanostructures on the heterogeneous Ag substrate varies from 1 nm - 9 nm, whereas their lateral size varies from 17 nm – 89 nm. However, since the lateral size measured in the AFM image results from the convolution of sample topography with the size of the AFM tip-apex (diameter ≈ 16 nm), the actual lateral size of the Ag nanoparticles is expected to be much smaller. (c) Confocal Raman spectrum of bulk pATP (blue, integration time: 1 s) and SERS spectrum of pATP (red, integration time: 60 s) adsorbed on a heterogeneous Ag substrate measured in air using 532 nm excitation laser. Laser power at the sample: 117 µW. In the confocal Raman spectrum of bulk pATP, characteristic a_1 Raman bands are visible at 1086 cm^{-1}, 1176 cm^{-1}, 1493 cm^{-1} and 1591 cm^{-1}, whereas in the SERS spectrum, characteristic Raman bands of DMAB are visible at 1071 cm^{-1}, 1142 cm^{-1}, 1390 cm^{-1}, 1437 cm^{-1} and 1577 cm^{-1}, indicating conversion of pATP → DMAB.[43] On the SERS active heterogeneous Ag substrate, DMAB is produced through dimerisation of pATP at the sites where plasmonic Ag nanostructures exhibit strong LSPR with the excitation laser and within plasmonic SERS hotspots, which are the locations of strongest LSPR produced by gap mode plasmons emerging between closely spaced plasmonic nanostructures. Therefore, the SERS spectrum represents the total amount of DMAB formed at all plasmonically active sites present within the probe area (≈1.6 × 10^5 nm^2) of the excitation laser spot at the sample surface. Furthermore, 1086 cm^{-1} and 1591 cm^{-1} Raman bands of pATP overlap with the DMAB Raman bands at 1071 cm^{-1} ($\nu_{C\text{-}S}$)and 1577 cm^{-1} ($\nu_{C=C}$), respectively. However, the pATP → DMAB reaction can be monitored using the DMAB a_g bands at 1142 cm^{-1} ($\beta_{C\text{-}H}$), 1390 cm^{-1} ($\nu_{N=N}$), 1437 cm^{-1} ($\nu_{N=N}$), which appear at distinct spectral positions compared to the pATP Raman bands.[45, 47, 48]

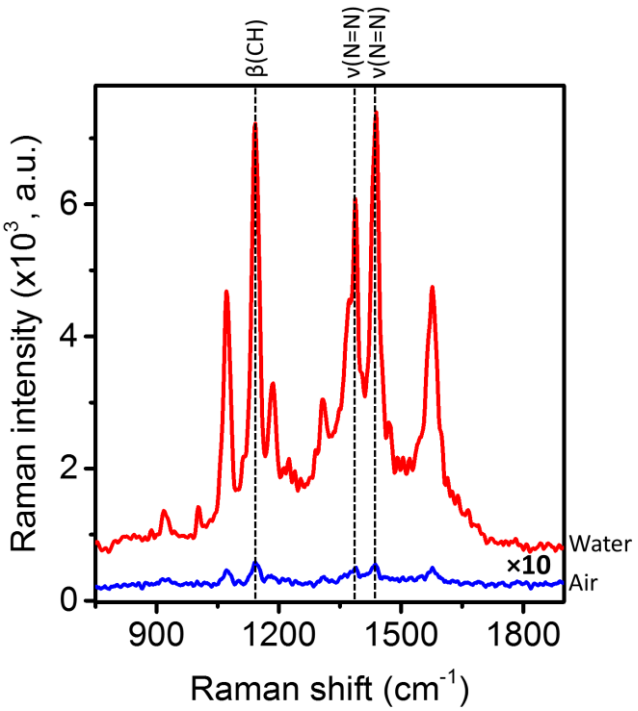

Fig. 4.9 pATP → DMAB SERS spectra measured on a heterogeneous Ag substrate in air (blue) and water (red). Integration time: 60 s. Laser power at the sample: 117 μW. Note that the SERS spectrum in air has been multiplied by a factor of 10 for easier visualisation.

SERS signal in the aqueous environment could be redshift of the LSPR of the Ag SERS substrate due to the higher refractive index of water,[49] serendipitously providing a better overlap with the excitation wavelength.

To rule out the possibility of ZrO_2-protected TERS probe interfering in pATP → DMAB reaction at the sample, we conducted TERS measurements on a thin film of pATP mixed with PMMA spin coated on a glass substrate as shown in Fig. 4.10. TERS spectrum measured at the of ZrO_2-protected TERS probe-apex on this sample did not show signal from any DMAB a_g Raman bands, whereas the a_1 Raman bands of pATP at 1086 cm^{-1} and 1591 cm^{-1} were enhanced by a contrast of 5.3 in the TERS near-field. This demonstrated the pinhole free character and chemical inertness of ZrO_2-protected TERS probes for investigation of catalytic reactions.

We first tested the sensitivity of ZrO_2-protected TERS probes for monitoring pATP → DMAB in air and aqueous environments. For measurements in air, we placed the TERS probe in contact with the Ag substrate and carried out Raman mapping around the probe. Fig. 4.11a shows the map of the 1437 cm^{-1} DMAB Raman band intensity, in which a much stronger intensity is observed at the positon

of the probe-apex. Comparison of average spectra measured at the TERS probe-apex (position P1) and away from it (positions P2-P4) presented in Fig. 4.11b showed that the DMAB bands are visible only in the TERS spectra measured at the probe-apex, indicating a strong LSPR. Although no DMAB bands are visible in the average SERS spectra from positions P2 – P4 during the short integration time of

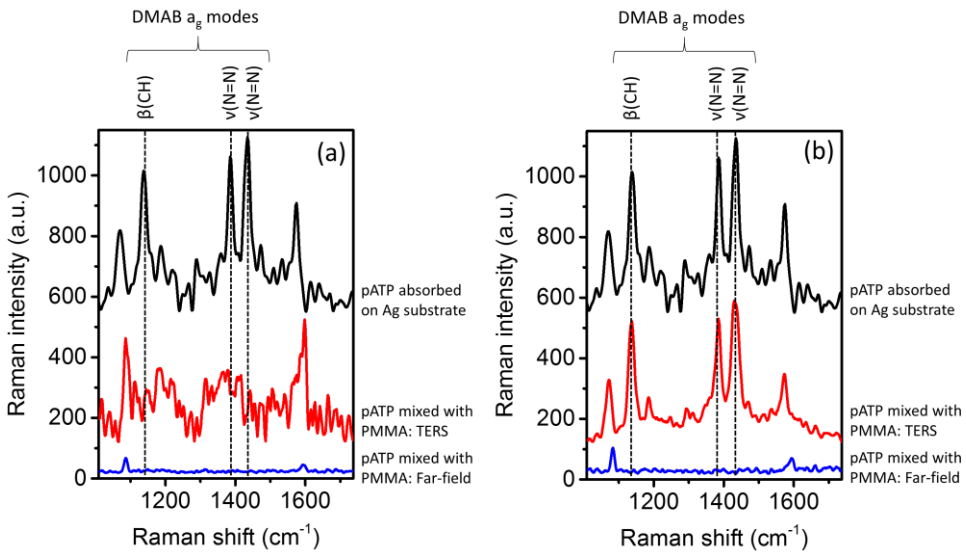

Fig. 4.10 (a) A ZrO_2-protected probe was placed in contact with a thin film of pATP mixed with PMMA spin coated on a glass substrate and Raman mapping was carried out around the probe by moving the objective lens in a raster fashion. TERS spectrum measured at the TERS probe-apex and far-field spectrum measured with the TERS probe retracted from the sample are shown in red and blue respectively. Integration time: 60s. Laser power at the sample: 50 µW. SERS spectrum (black) of pATP adsorbed on a heterogeneous Ag substrate (from Fig. 4.8c) is also shown for comparison. TERS spectrum shows absence of all DMAB a_g Raman bands. However, the a_1 Raman bands of pATP at 1086 cm^{-1} and 1591 cm^{-1} are enhanced by a contrast of 5.3 (measured using 1086 cm^{-1} band intensity) in the TERS near-field. (b) Similar TERS measurements on a thin film of pATP mixed with PMMA spin coated on a glass substrate with a Ag coated TERS probe without ZrO_2 protection. In the TERS spectrum (red) measured at the probe-apex, all DMAB a_g Raman bands are clearly visible confirming the pATP → DMAB reaction. Whereas, only pATP Raman band appear in the far-field spectrum (blue). Integration time: 60s. Laser power at the sample: 50 µW.

1 s, the DMAB bands do appear in the SERS spectrum when the integration time is increased to 60 s as shown in Fig. 4.8c. Note that whilst the SERS spectra at position P2-P4 represents the DMAB molecules produced within the probe area of excitation laser spot (≈1.6 × 10^5 nm^2), the TERS spectrum at positon P1 results from the Raman signal of DMAB produced in a much smaller region at the probe-apex (≈7.1 × 10^2 nm^2) in addition to the SERS signal from the area around the probe. Furthermore, the TERS signal measured at the position of maximum intensity in Fig.

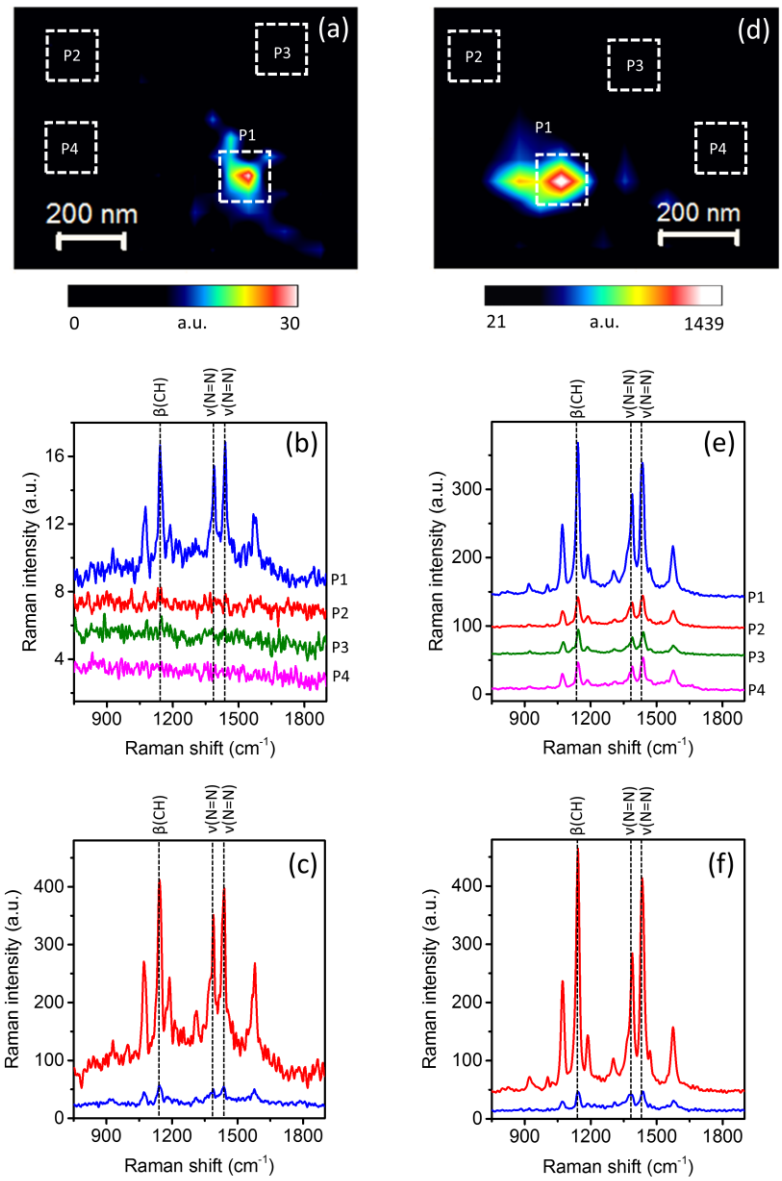

Fig. 4.11 Maps of pATP → DMAB at the TERS probe-apex obtained using the intensity of 1437 cm^{-1} ($\nu_{N=N}$) DMAB Raman band measured from pATP SAM on Ag substrate in (a) air and (d) water. Integration time: 1 s. Laser power at the sample: 117 µW. Average Raman spectra from 150 nm × 150 nm areas at the probe-apex (P1) and away from the probe-apex (P2 – P4) marked in (b) Fig. 4.11a and (e) Fig. 4.11d. TERS (red) and SERS (blue) spectra measured at the position of maximum DMAB signal in (c) Fig. 4.11a (f) Fig. 4.11d, with the TERS probe in contact and retracted from the sample, respectively. Integration time: 60 s (Fig. 4.11c), 1 s (Fig. 4.11f).

4.11a is found to be ≈ 12× stronger than the SERS signal measured at the same position with the probe retracted from the sample, as shown in Fig. 4.11c.

Next, we examined the sensitivity of the ZrO_2-protected TERS probes for monitoring pATP → DMAB in an aqueous environment. In this case, TERS measurements were performed inside a water droplet placed on the sample surface as shown in Fig. 4.1. A map of the 1437 cm^{-1} DMAB band intensity measured around the TERS probe-apex is shown in Fig. 4.11d. Once again, a significantly higher DMAB signal intensity is observed at the probe-apex indicating a strong LSPR. A comparison of average spectra measured at the probe-apex (P1) in Fig. 4.11d and away from it (P2-P4) is presented in Fig. 4.11e. Interestingly, average spectra from P1-P4 show a significantly higher signal to noise ratio compared to the corresponding measurements in air shown in Fig. 4.11b. Furthermore, average SERS spectra from areas away from the probe-apex (P2 – P4) in water show clear DMAB bands with an integration time of 1 s in contrast to the corresponding SERS spectra in air where no DMAB bands are visible. This is consistent with the higher SERS signal observed in water compared to air shown in Fig. 4.9. The intensity of the TERS signal in water is found to be ≈ 12× stronger compared to the SERS signal measured at the same location (Fig. 4.11f), clearly showing that the ZrO_2-protected TERS probes retain their plasmonic sensitivity in water.

Furthermore, comparison of average spectra measured at the probe-apex and away from it in Fig. 4.11e also confirms the chemical inertness rendered by ZrO_2-protection. In the Raman spectra, the $\nu_{C\text{-}S}$ vibrational mode at ≈1071 cm^{-1} is assigned to both pATP and DMAB, whereas the $\nu_{N=N}$ modes at 1390 cm^{-1} and 1437 cm^{-1} and the $\beta_{C\text{-}H}$ mode at 1142 cm^{-1} are assigned exclusively to DMAB.[43] Therefore, the relative conversion of pATP → DMAB can be assessed using the ratio of the average intensity of DMAB bands (I_{DMAB}) to I_{1071}.[45] Furthermore, this ratiometric analysis method allows quantification in spite of fluctuations in the absolute TERS signal.[50] Calculations of I_{DMAB} / I_{1071} at locations P1–P4 in Fig. 4.11d are presented in Table 4.1. At all four locations, I_{DMAB} / I_{1071} is found to be ≈1.9 indicating that the conversion of pATP → DMAB is unaffected by the presence of the ZrO_2-protected TERS probe, and it can therefore be considered as chemically non-interfering.

Results shown in Fig. 4.11 demonstrate that the strong LSPR in the nanogap between a TERS probe and metal substrate can open up the possibilities of studying molecular transformations on single catalyst particles with different shapes, sizes and crystal orientations in both air and liquid environments by placing them at a TERS probe-apex. The LSPR generated at the TERS probe-apex can act as a sensitive probe to monitor the structural changes of adsorbed reactants elucidating structure-performance relationships for efficient catalytic conversion.

Finally, we performed nanoscale chemical mapping of pATP → DMAB reaction on a heterogenous Ag substrate in water. Fig. 4.12a shows an AFM height

Table 4.1. Calculation of I_{DMAB}/I_{1071} ratio at locations P1 – P4 in Fig. 4.11d. I_{DMAB} is calculated from the average intensity of DMAB Raman bands at 1142 cm^{-1} (I_{1142}), 1390 cm^{-1} (I_{1390}) and 1437 cm^{-1} (I_{1437}). For comparison, I_{DMAB}/I_{1071} has also been calculated for the highest intensity spectrum observed in area P1 at the probe-apex. A similar I_{DMAB}/I_{1071} at the locations P1-P4 indicates that the ZrO_2-protected TERS probe does not interfere with the pATP → DMAB reaction.

Location	I_{1071} (a.u.)	I_{1142} (a.u.)	I_{1390} (a.u.)	I_{1437} (a.u.)	$(I_{1142} + I_{1390} + I_{1437})/3$ (I_{DMAB})	I_{DMAB}/I_{1071}
P1	97	217	144	191	184	1.9
P2	22	43	35	46	41	1.9
P3	16	35	25	32	31	1.9
P4	21	38	33	46	39	1.9
Highest signal at P1	197	428	244	361	344	1.8

image of the surface, and Fig. 4.12b shows a TERS map of the pATP → DMAB conversion, obtained using the I_{DMAB}/I_{1071} ratio in an area of 500 nm × 500 nm.

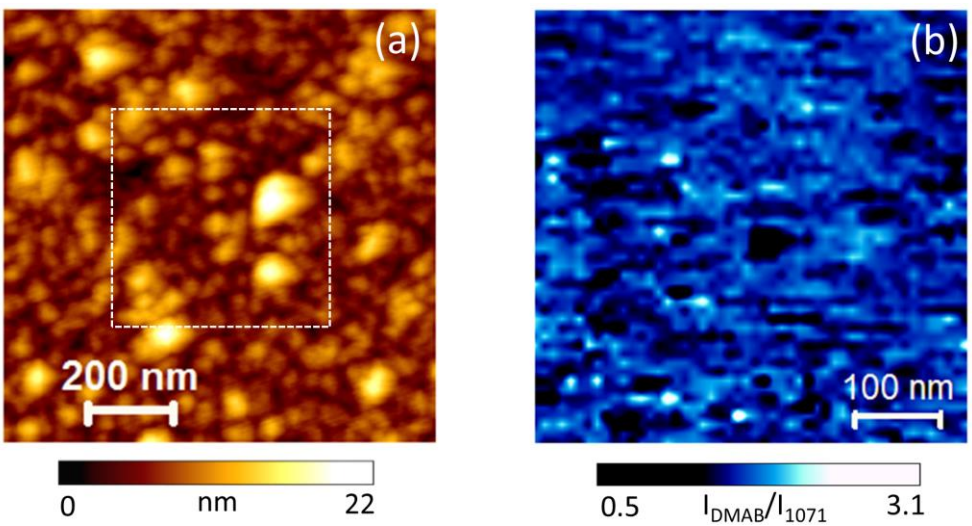

Fig. 4.12 (a) AFM topography image of a heterogeneous Ag substrate functionalised with pATP. (b) TERS map of I_{DMAB}/I_{1071} intensity ratio for area marked in Fig. 4.12a measured within an aqueous environment. Integration time: 1 s. Laser power at the sample: 117 μW.

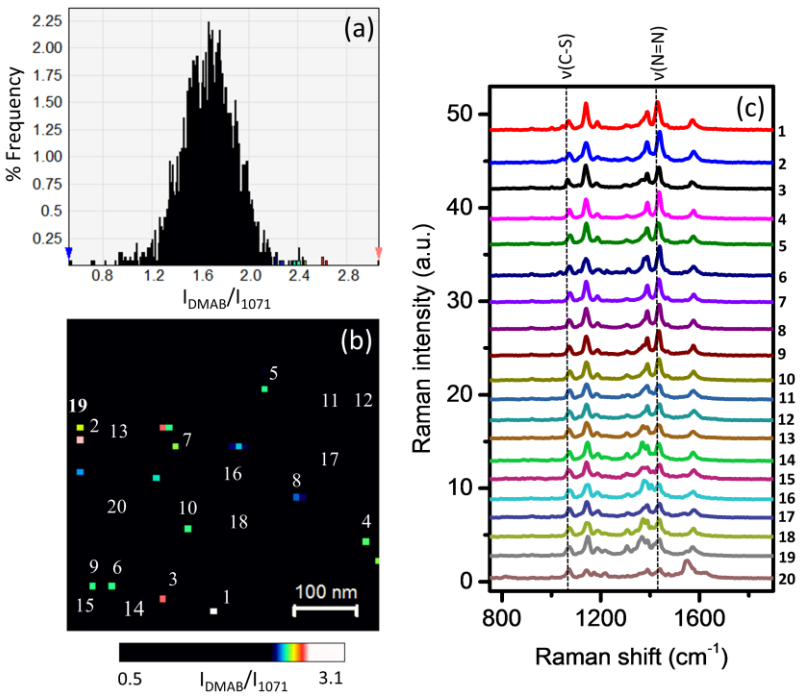

Fig. 4.13 (a) Histogram showing % frequency of I_{DMAB}/I_{1071} ratio in the pATP → DMAB TERS map in Fig. 4.12b. (b) TERS map of pATP → DMAB conversion within an aqueous environment shown in Fig. 4.12b with adjusted contrast to highlight regions of notably high activity. TERS intensity of the high activity reaction hotspots is also highlighted in colour in the histogram shown in Fig. 4.13a. (c) Plot of TERS spectra from ten different locations of high and low I_{DMAB}/I_{1071} ratio marked as 1-10 and 11-20, respectively in Fig. 4.13a. Spectra have been normalised to the intensity of Raman band at 1071 cm^{-1} for easier comparison. At positions 6, 13, 14, 15, 16, 18, and 19, Raman band appearing at ≈ 1365 cm^{-1} is assigned to the C-H bending mode resulting from the local structural deformation of DMAB molecules on the sample reported previously by Uetsuki *et al.*[51] This indicates that the DMAB molecules formed at various locations on the heterogeneous Ag substrate are oriented differently.

The conversion exhibits a high degree of spatial heterogeneity across the Ag substrate employed. A histogram analysis of the I_{DMAB} / I_{1071} ratio across this map presented in Fig. 4.13a is consistent with a broad range of catalytic activities measured at the sample. Furthermore, the TERS map in Fig. 4.12b exhibits a number of highly localised regions of notably high pATP → DMAB conversion. Fig. 4.13b shows the TERS map of pATP → DMAB conversion shown in Fig. 4.12b with adjusted contrast to highlight regions of markedly high activity. These "reaction hotspots" are labelled as 1-10 in Fig. 4.13b and corresponding TERS spectra are shown in Fig. 4.13c. For comparison, example spectra from regions of low conversion labelled as 11-20 in Fig. 4.13b are also shown in Fig. 4.13c. At locations 1-10 a larger amount of DMAB is formed on the heterogeneous Ag substrate during pATP → DMAB compared to locations 11-20, as evidenced by the much higher

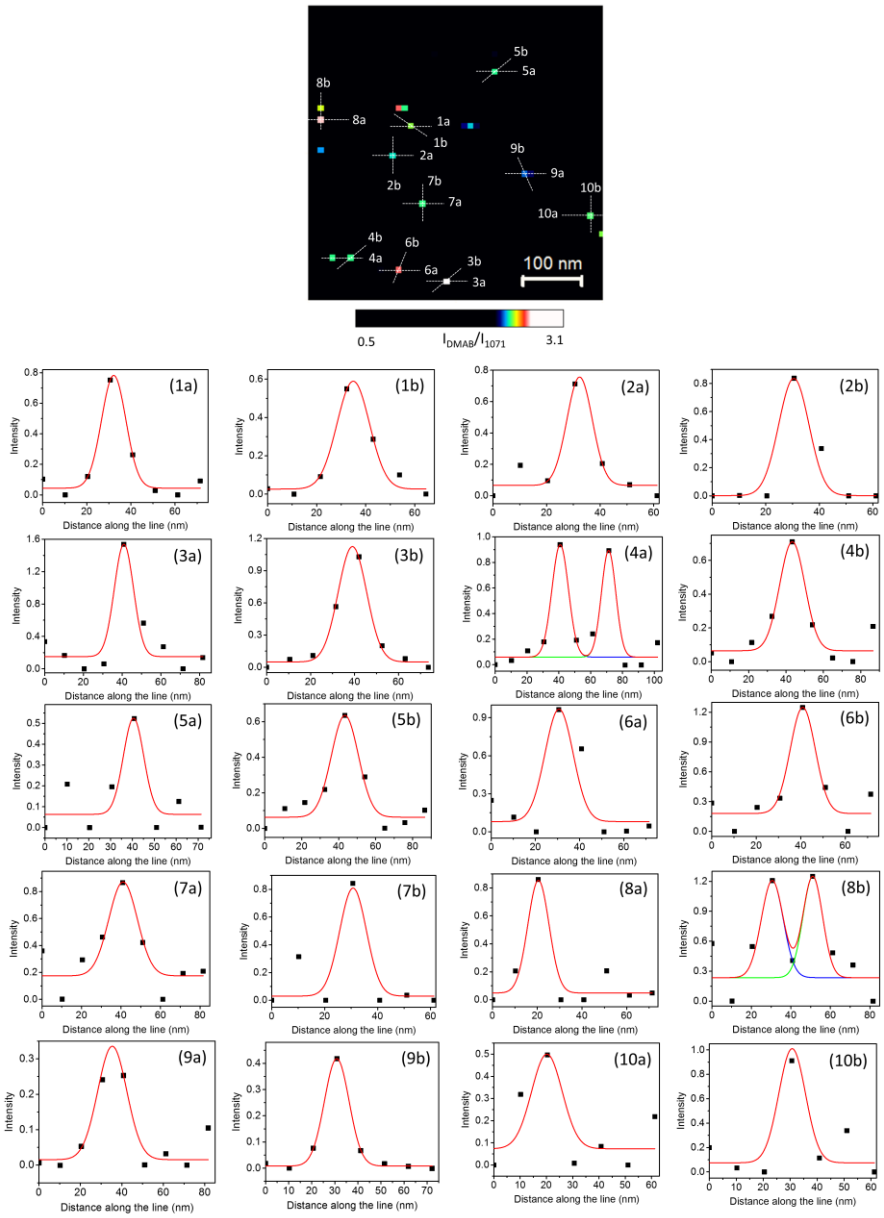

Fig. 4.14 Top: TERS map of pATP → DMAB in aqueous environment shown in Fig. 4.12b with the contrast adjusted to reveal regions of notably high activity. Bottom: Intensity profiles along the lines marked as 1 – 10 in the TERS map shown on top in horizontal (a) and oblique (b) directions fitted with Gaussian curves. The average full width at half maximum (FWHM) of the Gaussian fits to all line profiles is calculated to be 13.5 ± 2.1 nm. This shows the highly localised nature of the reaction hotspots on the Ag substrate as well the nanoscale spatial resolution of TERS for mapping of these hotspots within an aqueous environment. The intensity scale on the Y-axis represents the I_{DMAB}/I_{1071} ratio after linear baseline subtraction.

I_{DMAB}/I_{1071} ratio in the corresponding TERS spectra. We propose that these extremely confined regions of high conversion reflect the plasmon-assisted nature of the pATP → DMAB reaction,[46] in which LSPR at and between individual Ag nanoparticles can confine light to extremely small (< 1 nm^3) volumes.[52] Line profile analysis of the high activity regions presented in Fig. 4.14 and Table 4.2 indicates that these reaction hotspots are typically confined to one or two pixels (100 nm^2 – 200 nm^2), consistent with a nanoscale spatial resolution.

Table 4.2 Spatial analysis of the reaction hotspots of pATP → DMAB TERS map. List of FWHM calculated from the Gaussian fit to the line profiles in horizontal (a) and oblique (b) directions at 10 different hotspots shown in Fig. 4.14.

Line profile	FWHM (nm)	
	Horizontal direction (a)	Oblique direction (b)
1	13.0	15.6
2	11.2	13.3
3	11.7	15.3
4	11.4	15.9
5	11.0	17.2
6	15.0	13.3
7	17.0	11.9
8	11.2	12.4
9	16.5	12.6
10	13.7	11.2
Average	13.5 ± 2.1	

4.4 Conclusions

We have addressed the key challenges of chemical inertness, plasmonic degradation and instability within a liquid environment of Ag coated TERS probes by developing a novel method of protecting them with an ultrathin dielectric layer of zirconia. This successfully extends the lifetime of the probes by over 850×, from a few hours to > 4.5 months, while rendering them chemically inert for the investigation of catalytic reactions at the nanoscale. Finally, using the robust and durable zirconia-protected probes we have demonstrated mapping of a model catalytic reaction on a heterogeneous substrate within a liquid environment with nanoscale spatial resolution. This work opens up the possibility of using TERS as a nanoanalytical tool to map molecular heterogeneities and interfacial dynamics *in situ*, in diverse areas of scientific research such as heterogeneous catalyst systems,[4] biology[53] and electrochemistry,[54] in which nanoscale features at solid-liquid interfaces play a

primary role in governing chemical behavior. Furthermore, this clear improvement in the probe lifetime and structural and chemical stability significantly broadens the scope of AFM-TERS for non-destructive, label-free and nanoscale chemical characterisation on a wide range of samples and environments.

References

1. J. Hagen, *Industrial Catalysis: A Practical Approach, 2nd Ed.*, Wiley-VCH, Weinheim, 2015.
2. I. L. C. Buurmans and B. M. Weckhuysen, *Nat. Chem.*, 2012, **4**, 873-886.
3. G. Rothenberg, *Catalysis: Concepts and Green Applications, 2nd Ed.*, Wiley-VCH, Weinheim, 2017.
4. B. M. Weckhuysen, *In-situ Spectroscopy of Catalysts*, American Scientific Publishers, Stevenson Ranch, 2004.
5. G. Mestl, *J. Mol. Catal. A-Chem.*, 2000, **158**, 45-65.
6. P. Verma, *Chem. Rev.*, 2017, **117**, 6447-6466.
7. T. Deckert-Gaudig, A. Taguchi, S. Kawata and V. Deckert, *Chem. Soc. Rev.*, 2017, **46**, 4077-4110.
8. N. Kumar, M. M. Drozdz, H. Jiang, D. M. Santos and D. J. Vaux, *Chem. Commun.*, 2017, **53**, 2451-2454.
9. B. S. Yeo, E. Amstad, T. Schmid, J. Stadler and R. Zenobi, *Small*, 2009, **5**, 952-960.
10. A. Lucia, O. A. Cacioppo, E. Iulianella, L. Latessa, G. Moccia, D. Passeri and M. Rossi, *Appl. Phys. Lett.*, 2017, **110**, 103105.
11. S. Berweger, C. C. Neacsu, Y. Mao, H. Zhou, S. S. Wong and M. B. Raschke, *Nat. Nanotechnol.*, 2009, **4**, 496-499.
12. N. Kumar, A. Zoladek-Lemanczyk, A. A. Guilbert, W. Su, S. M. Tuladhar, T. Kirchartz, B. C. Schroeder, I. McCulloch, J. Nelson and D. Roy, *Nanoscale*, 2017, **9**, 2723-2731.
13. T.-a. Yano, T. Ichimura, S. Kuwahara, F. H'Dhili, K. Uetsuki, Y. Okuno, P. Verma and S. Kawata, *Nat. Commun.*, 2013, **4**, 2592.
14. W. Su, N. Kumar, N. Dai and D. Roy, *Chem. Commun.*, 2016, **52**, 8227-8230.
15. W. Su, N. Kumar, S. Mignuzzi, J. Crain and D. Roy, *Nanoscale*, 2016, **8**, 10564-10569.
16. R. Zhang, Y. Zhang, Z. C. Dong, S. Jiang, C. Zhang, L. G. Chen, L. Zhang, Y. Liao, J. Aizpurua, Y. Luo, J. L. Yang and J. G. Hou, *Nature*, 2013, **498**, 82-86.
17. A. B. Zrimsek, N. Chiang, M. Mattei, S. Zaleski, M. O. McAnally, C. T. Chapman, A.-I. Henry, G. C. Schatz and R. P. Van Duyne, *Chem. Rev.*, 2016, **117**, 7583 - 7613.
18. H. Kim, K. M. Kosuda, R. P. Van Duyne and P. C. Stair, *Chem. Soc. Rev.*, 2010, **39**, 4820-4844.
19. T. Hartman, C. S. Wondergem, N. Kumar, A. van den Berg and B. M. Weckhuysen, *J. Phys. Chem. Lett.*, 2016, **7**, 1570-1584.
20. K. F. Domke and B. Pettinger, *ChemPhysChem*, 2009, **10**, 1794-1798.
21. E. M. van Schrojenstein Lantman, T. Deckert-Gaudig, A. J. G. Mank, V. Deckert and B. M. Weckhuysen, *Nat. Nanotechnol.*, 2012, **7**, 583-586.
22. N. Kumar, B. Stephanidis, R. Zenobi, A. Wain and D. Roy, *Nanoscale*, 2015, **7**, 7133-7137.
23. J.-H. Zhong, X. Jin, L. Meng, X. Wang, H.-S. Su, Z.-L. Yang, C. T. Williams and B. Ren, *Nat. Nanotechnol.*, 2017, **12**, 132-136.
24. N. Martín Sabanés, L. M. Driessen and K. F. Domke, *Anal. Chem.*, 2016, **88**, 7108-7114.
25. N. Martín Sabanés, T. Ohto, D. Andrienko, Y. Nagata and K. F. Domke, *Angew. Chem. Int. Ed.*, 2017, **56**, 9796-9801.
26. M. Mattei, G. Kang, G. Goubert, D. V. Chulhai, G. C. Schatz, L. Jensen and R. P. Van Duyne, *Nano Lett.*, 2016, **17**, 590-596.
27. T. Schmid, B. S. Yeo, G. Leong, J. Stadler and R. Zenobi, *J. Raman Spectrosc.*, 2009, **40**, 1392-1399.

28. J. D. Scherger and M. D. Foster, *Langmuir*, 2017, **33**, 7818-7825.
29. T. Touzalin, A. L. Dauphin, S. Joiret, I. T. Lucas and E. Maisonhaute, *Phys. Chem. Chem. Phys.*, 2016, **18**, 15510-15513.
30. Z.-C. Zeng, S.-C. Huang, D.-Y. Wu, L.-Y. Meng, M.-H. Li, T.-X. Huang, J.-H. Zhong, X. Wang, Z.-L. Yang and B. Ren, *J. Am. Chem. Soc.*, 2015, **137**, 11928-11931.
31. D. Kurouski, M. Mattei and R. P. Van Duyne, *Nano Lett.*, 2015, **15**, 7956-7962.
32. N. Kumar, W. Su, M. Vesely, B. M. Weckhuysen, A. J. Pollard and A. J. Wain, *Nanoscale*, 2018, **10**, 1815-1824.
33. W. Su, N. Kumar, S. Mignuzzi, J. Crain and D. Roy, *Nanoscale*, 2016, **8**, 10564-10569.
34. N. Kumar, S. J. Spencer, D. Imbraguglio, A. M. Rossi, A. J. Wain, B. M. Weckhuysen and D. Roy, *Phys. Chem. Chem. Phys.*, 2016, **18**, 13710-13716.
35. J. Kalbacova, R. D. Rodriguez, V. Desale, M. Schneider, I. Amin, R. Jordan and D. R. Zahn, *Nanospectroscopy*, 2014, **1**, 12-18.
36. L. Opilik, Ü. Dogan, J. Szczerbiński and R. Zenobi, *Appl. Phys. Lett.*, 2015, **107**, 091109.
37. B. S. Yeo, J. Stadler, T. Schmid, R. Zenobi and W. H. Zhang, *Chem. Phys. Lett.*, 2009, **472**, 1-13.
38. C. A. Barrios, A. V. Malkovskiy, A. M. Kisliuk, A. P. Sokolov and M. D. Foster, *J. Phys. Chem. C*, 2009, **113**, 8158-8161.
39. L. Opilik, U. z. Dogan, C.-Y. Li, B. Stephanidis, J.-F. Li and R. Zenobi, *J. Phys. Chem. C*, 2016, **120**, 20828-20832.
40. M. Pourbaix, *Atlas of Electrochemical Equilibria in Aqueous Solutions*, National Association of Corrosion Engineers, Houston, 1974.
41. P. D. Vaidya and J. A. Lopez-Sanchez, *ChemistrySelect*, 2017, **2**, 6563-6576.
42. R. M. Navarro, M. Pena and J. Fierro, *Chem. Rev.*, 2007, **107**, 3952-3991.
43. Y.-F. Huang, H.-P. Zhu, G.-K. Liu, D.-Y. Wu, B. Ren and Z.-Q. Tian, *J. Am. Chem. Soc.*, 2010, **132**, 9244-9246.
44. N. Kumar, A. Rae and D. Roy, *Appl. Phys. Lett.*, 2014, **104**, 123106.
45. Z. Zhang, V. Merk, A. Hermanns, W. E. S. Unger and J. Kneipp, *ACS Catal.*, 2017, **7**, 7803-7809.
46. L. B. Zhao, M. Zhang, Y. F. Huang, C. T. Williams, D. Y. Wu, B. Ren and Z. Q. Tian, *J. Phys. Chem. Lett.*, 2014, **5**, 1259-1266.
47. K. Kim, D. Shin, K. L. Kim and K. S. Shin, *Phys. Chem. Chem. Phys.*, 2012, **14**, 4095-4100.
48. P. Xu, L. Kang, N. H. Mack, K. S. Schanze, X. Han and H.-L. Wang, *Sci. Rep.*, 2013, **3**, 2997.
49. J. J. Mock, D. R. Smith and S. Schultz, *Nano Lett.*, 2003, **3**, 485-491.
50. S. W. Bishnoi, C. J. Rozell, C. S. Levin, M. K. Gheith, B. R. Johnson, D. H. Johnson and N. J. Halas, *Nano Lett.*, 2006, **6**, 1687-1692.
51. K. Uetsuki, P. Verma, T.-A. Yano, Y. Saito, T. Ichimura and S. Kawata, *J. Phys. Chem. C*, 2010, **114**, 7515-7520.
52. F. Benz, M. K. Schmidt, A. Dreismann, R. Chikkaraddy, Y. Zhang, A. Demetriadou, C. Carnegie, H. Ohadi, B. de Nijs, R. Esteban, J. Aizpurua and J. J. Baumberg, *Science*, 2016, **354**, 726-729.
53. Y. F. Dufrêne, *Nat. Rev. Microbiol.*, 2004, **2**, 451 - 460.
54. M. J. Weaver and X. Gao, *Annu. Rev. Phys. Chem.*, 1993, **44**, 459-494.

Chapter 5

Nanoscale Chemical Imaging of a Single Catalyst Particle using Tip-enhanced Fluorescence Microscopy

Abstract

Determining active sites in real-life solid catalysts remains an intellectual challenge and is crucial for exploring the road towards their rational design. In recent years, various micro-spectroscopic methods have revealed valuable structure-activity data at the level of a single catalyst particle, even under reaction conditions. In this Chapter, tip-enhanced fluorescence (TEFL) microscopy is introduced as a novel and versatile characterisation tool for catalysis research. This has been demonstrated using a fluid catalytic cracking (FCC) catalyst as showcase material. Thin sectioning of industrially used FCC particles together with selective staining of Brønsted acidity enabled high-resolution TEFL mapping of different catalyst regions. Furthermore, hyperspectral information gained *via* TEFL microscopy reveals a spatial distribution of Brønsted acidity within individual zeolite domains in different regions of the FCC catalyst particle. Finally, comparison of TEFL measurements from different FCC particles showed significant intra- and inter-particle heterogeneities in zeolite domain size and chemical reactivity.

This chapter is based on: N. Kumar, S. Kalirai, A. J. Wain and B. M. Weckhuysen, *ChemCatChem*, 2018. DOI: 10.1002/cctc.201801023

5.1 Introduction

During the last two decades, significant progress has been made in the use of localised surface plasmon resonance (LSPR) generated at the apex of a metallic scanning probe microscopy tip under laser excitation as a means to enhance optical signals.[1] The physical principle underlying this approach, broadly referred to as tip-enhanced optical spectroscopy (TEOS), is enhancement of the local electromagnetic (EM) field and its confinement to a small volume of space surrounding the probe apex.[2] This near-field phenomenon increases the chemical sensitivity of TEOS and pushes its spatial resolution far beyond the diffraction limit of light. To date, TEOS has been predominantly used to enhance two types of optical signal: Raman scattering and photoluminescence emission. Enhancement of Raman signals in this way is commonly known as tip-enhanced Raman spectroscopy (TERS),[3-6] and has been extensively used for nanoscale chemical characterisation in a wide range of disciplines including biology,[7] material science,[8] polymer blends,[9] solar cells,[10] catalysis,[11] single molecule detection,[12] carbon nanotubes[13] and two-dimensional (2D) materials such as graphene.[14,15] On the other hand, its counterpart tip-enhanced photoluminescence (TEPL) microscopy has remained rather underexplored.[16, 17] This is particularly true in the case of fluorescence microscopy, where external fluorescent labels are used to generate photoluminescence, with only a handful of published reports demonstrating tip-enhanced fluorescence (TEFL) measurements.[18-20]

In this Chapter, we demonstrate the application of TEFL microscopy for nanoscale investigation of zeolite domains within a fluid catalytic cracking (FCC) particle. FCC is a leading industrial process for the conversion of crude oil fractions into valuable products, such as gasoline and propylene.[21, 22] This catalytic process utilises 50 μm – 150 μm sized spherical particles containing a zeolite component, such as zeolite Y or ZSM-5, embedded in a matrix of clay, silica, and alumina. The cracking properties of the FCC particles are critically determined by the Brønsted acid sites present within the zeolite domains. Cyclical catalysis and regeneration processes of the FCC particles result in a decrease in the strength and number of Brønsted acid sites within the zeolite domains leading to the lowering of their overall catalytic reactivity. However, due to their inherent chemical and structural complexity, a detailed nanoscale characterisation of the Brønsted acid sites and their spatial distribution within a FCC particle remains extremely challenging.

Previously, confocal fluorescence microscopy (CFM) has been applied to visualise Brønsted acidity within single FCC particles, differing in their catalytic cracking activity, using different Brønsted acid catalysed staining reactions.[23-26] However, due to its diffraction limited spatial resolution and relatively low sensitivity,

CFM cannot provide information about the catalytically active zeolite domains at the nanometre length-scales. Recently, single molecule fluorescence (SMF) microscopy has been used for the investigation of zeolite domains within FCC particles.[27-30] However, SMF is still restricted in resolution for the case of non-dilute fluorescent events and requires a relatively complicated data processing.[27-30] Furthermore, unlike SMF, TEFL provides 2D hyperspectral information, which can allow simultaneous measurement of multiple fluorescent species having different emission wavelengths, enabling detailed chemical information to be gleaned. In other words, in contrast to SMF and CFM, TEFL provides direct *chemical* information at the *nanoscale* without the requirement for complex data processing techniques.

In this Chapter, we have applied TEFL to directly map the catalytic activity within industrially applied FCC catalyst particles containing zeolite Y as the active phase. TEFL microscopy is implemented by placing a Ag coated atomic force microscopy (AFM) probe within the excitation laser spot of an inverted confocal optical microscope (Fig. 5.1a). We have used the Brønsted acid catalysed oligomerisation of thiophene as a probe molecule, which produces fluorescent conjugated carbocationic species of varying length (Fig. 5.1b).[26, 31] An example of a high-resolution fluorescence image of a zeolite domain obtained using TEFL microscopy is shown in Fig. 5.1c. Since the fluorescent species are exclusively formed at the Brønsted acid sites within the zeolite aggregates, their fluorescence emission intensity can be directly used to localise and evaluate Brønsted acidity and hence directly determine the size and inherent reactivity of the zeolite domains. We show that high-resolution spectroscopic information gained *via* TEFL microscopy provides detailed insights into the distribution of Brønsted acidity within individual zeolite domains and reveals significant intra- and inter-particle variations in their size and reactivity.

5.2 Experimental

5.2.1 TEFL Microscopy Set-up

A home built TEFL microscopy system in transmission mode was used for this work, which consisted of an atomic force microscope (AFM) (AIST- NT, USA) fitted on top of an inverted confocal microscope (Nikon, Japan) attached to a Raman spectrometer (Horiba Scientific, France) and a charge coupled device detector (Andor Technology, UK). A radially polarised frequency doubled 532 nm Nd:YAG laser (Coherent, USA) was focussed onto the sample using a 100×, 1.49 NA oil immersion objective lens (Nikon, Japan) to measure the TEFL and far-field fluorescence spectra. All TEFL measurements were conducted in contact mode

AFM. A photograph of the TEFL microscope used in this work is shown in Fig. 5.2.

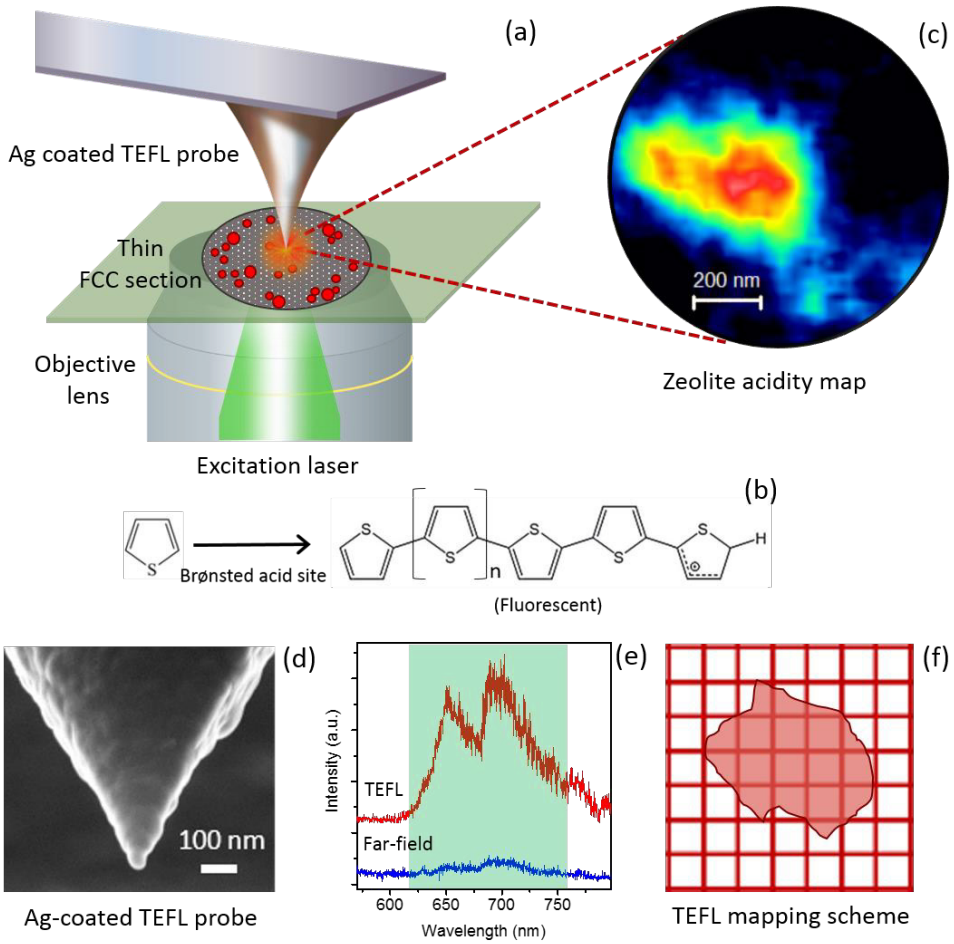

Fig. 5.1 (a) Schematic diagram of the TEFL microscopy configuration used in this work. (b) Example of the Brønsted acid-catalysed oligomerisation of thiophene to form fluorescent carbocationic species at the acid sites of zeolite domains. (c) Chemical map of acidity distribution within an individual zeolite domain obtained *via* TEFL mapping. (d) Scanning electron microscopy (SEM) image of a representative Ag coated TEFL probe used in this work. Typical diameter of the probe-apex is ≈ 50 nm. (e) An exemplary TEFL spectrum (Red) measured with the TEFL probe in contact with the FCC sample and the far-field FL spectrum (Blue) measured at the same position with the TEFL probe retracted from the FCC sample. Integration time: 10 s. Laser power: 365 μW. Excitation laser: 532 nm. The intensity scale on the Y-axis is in arbitrary units (a.u). (f) Diagram illustrating the TEFL mapping scheme. A thin FCC section placed on a glass substrate is moved in a raster fashion between the TEFL probe and excitation laser as shown in Fig. 5.1a, whilst measuring a TEFL spectrum at each pixel of the mapped region.

5.2.2 Preparation of TEFL Probes

The probes for performing TEFL measurements were prepared by depositing 100 nm Ag on contact mode Si AFM probes (MikroMasch, USA) oxidised

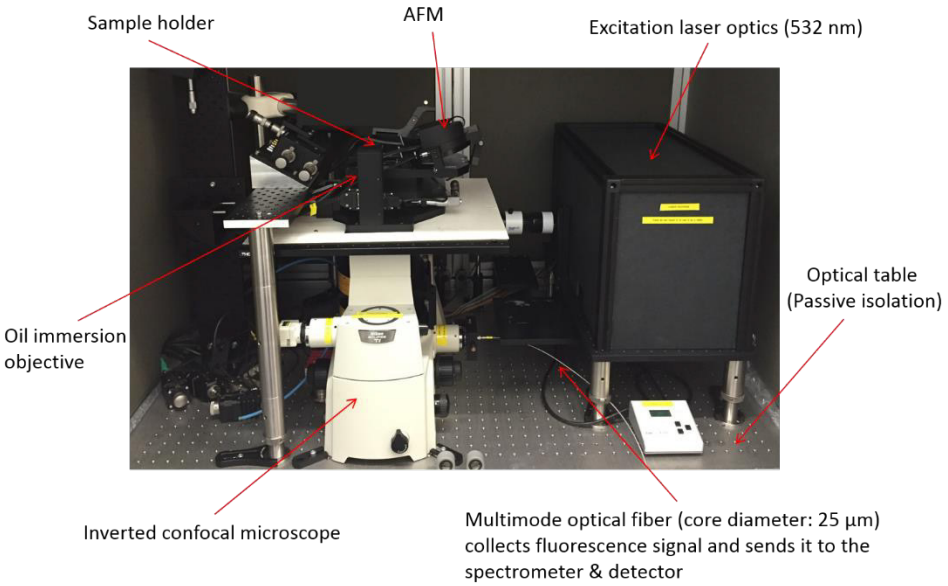

Fig. 5.2 Photograph of the home built TEFL microscopy system used in this work for nanoscale chemical imaging of zeolite domains within single FCC particles.

to a thickness of 300 nm SiO_2. The thermal evaporation of Ag was carried out in a vacuum evaporator (MBRAUN, Germany) at 10^{-6} mbar pressure with a slow deposition rate of 0.05 nm s^{-1}. An SEM image of a representative Ag coated AFM probe is shown in Fig. 5.1d.

5.2.3 Sample Preparation

FCC particles in their equilibrated state (E-CAT) having zeolite Y as the active phase (Albemarle Catalysts Company B.V., Amsterdam) were investigated in this study. The spherical FCC particles were first embedded within an epoxy resin (EpoFix, Agar Scientific, UK) and cured at 60 °C. Sections were cut to ≈ 100 nm thickness using an ultramicrotome (Ultracut Reichert E, Austria) with a diamond knife. To remove epoxy resin and ensure a flat section topography, thin FCC sections were placed on a glass coverslip (thickness = 0.17 mm) and calcined in a static oven using the following scheme - 6 h: 20°C to 500 °C, 6 h: 500°C, 6 h: 500°C to 20 °C. Staining of the sectioned and calcined FCC particles was performed by placing them in a sealed glass container and exposing them to 100 µl of thiophene. Thiophene

oligomerisation reaction was carried out by placing the stained FCC particles in a 120 °C oven for 30 minutes following the procedure reported by Buurmans *et al*.[23]

5.3 Results and Discussion

In the first part of this study, we tested the sensitivity of Ag coated TEFL probes for detection of the fluorescence signal originating from the carbocationic species formed from the oligomerisation of thiophene probe molecules. Fig. 5.1e shows the TEFL and far-field fluorescence spectra measured with a TEFL probe in contact and retracted from a zeolite region within a thin FCC section on a glass substrate. Two prominent fluorescence bands around 650 nm and 700 nm are observed in these spectra, which are assigned to distinct conjugated oligomeric carbocationic species containing > 4 monomer units formed *via* the catalytic conversion of thiophene at Brønsted acid sites.[26, 31] In the TEFL spectrum, a higher fluorescence intensity is observed due to the plasmonic enhancement of the EM field intensity at the probe-apex. Similar to TERS measurements,[32] the plasmonic enhancement of a TEFL signal compared to the far-field FL signal can be calculated using "contrast", which is defined as[32]

$$Contrast = \frac{I_{TEFL}}{I_{Far-field}} - 1 \tag{5.1}$$

where, I_{TEFL} and $I_{Far\text{ - }field}$ are the intensity of fluorescence signal measured with the TEFL probe in contact and retracted from the sample, respectively. Using Equation 5.1, the contrast of the 700 nm band in the TEFL spectrum in Fig. 5.1e is estimated to be 9.3. This indicates that the Ag coated TEFL probe undergoes efficient LSPR with the 532 nm excitation laser leading to a strong enhancement of the local electric field intensity at the AFM probe-apex.

Using plasmonically active TEFL probes, we carried out high-resolution fluorescence microscopy of thin FCC sections of three different FCC catalyst particles, labelled as FCC1, FCC2 and FCC3 following the scheme illustrated in Fig. 5.1f. In order to determine the size of the most reactive zeolite region inside the measured TEFL maps, the following thresholding procedure was implemented for a binary segmentation of zeolite domains:

1. TEFL mapping was carried out at five different locations within a FCC particle using a Ag coated TEFL probe. Prior to the TEFL mapping at each location, plasmonic sensitivity of the TEFL probe was checked by measuring contrast between TEFL and far-field signals using Equation 5.1.

2. The intensity of each TEFL map was normalised by the contrast of TEFL probe measured at that location. For simplicity, the normalised TEFL intensity is simply referred to as “TEFL intensity” in this Chapter.

3. A segmentation of the intensity histogram was performed collectively for all TEFL maps of each FCC particle using an expectation maximisation of a Gaussian mixture model. Here, three Gaussian curves were used corresponding to 1) background, 2) catalytically active and 3) most catalytically active regions as shown in Fig. 5.3.

4. The intersection point of the middle (red) and rightmost (blue) Gaussian fits to the histograms shown in Fig. 5.3 was used to determine a global threshold to determine the size of the most catalytically active regions in the TEFL maps of each FCC particle.

5. Based on this procedure, global threshold values of 2.1, 3.1 and 5.2 were calculated for FCC particles 1 - 3, respectively and used for further analysis of the measured TEFL maps.

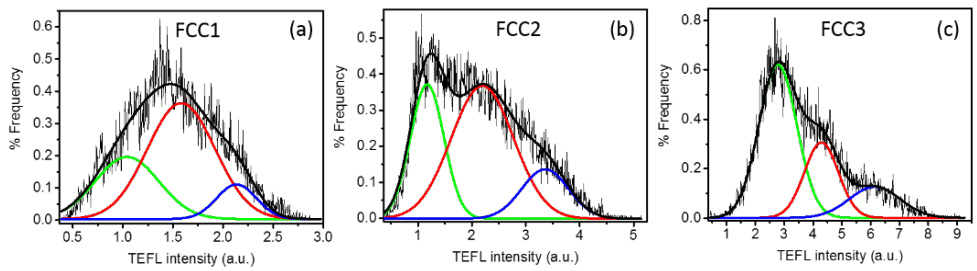

Fig. 5.3 Histograms of normalised TEFL intensity in the TEFL maps measured in different parts of (a) FCC particle 1 (FCC1), (b) FCC particle 2 (FCC2) and (c) FCC particle 3 (FCC3), respectively fitted with three Gaussian curves corresponding to 1) background (green), 2) catalytically active (red) and 3) the most catalytically active (blue) regions. Difference in the average TEFL intensity among the three FCC particles likely reflects their different “catalytic age”. Furthermore, the difference in the shapes of the intensity histograms indicates intra- and inter-particle differences in the Brønsted acidity of zeolite domains within the three FCC particles.

The thresholding procedure was applied to the TEFL maps measured from different locations of the FCC particles presented in Fig. 5.4 - 5.7.

The hyperspectral TEFL mapping performed in a 1 μm × 1 μm area marked as 1 in the centre of FCC1 (Fig. 5.4a) is resented in Fig. 5.4. TEFL spectra in the 540 nm - 800 nm range were measured from 50 × 50 pixels (20 nm × 20 nm pixel size) in the mapped region. The TEFL spectra measured at each pixel in the map were fitted using two Gaussian curves centred at 650 nm and 700 nm after linear background subtraction and the total intensity of the fitted Gaussian curves was used

to construct the TEFL map shown in Fig. 5.4b. A region of high fluorescence intensity is observed in the centre of the TEFL map indicating a high density of Brønsted acid sites at this location. A histogram of the TEFL intensity measured in the TEFL map is shown in Fig. 5.4c. Binary image of the most catalytically active regions in Fig. 5.4b is shown in Fig. 5.4d. In this image, the most reactive regions of the TEFL map

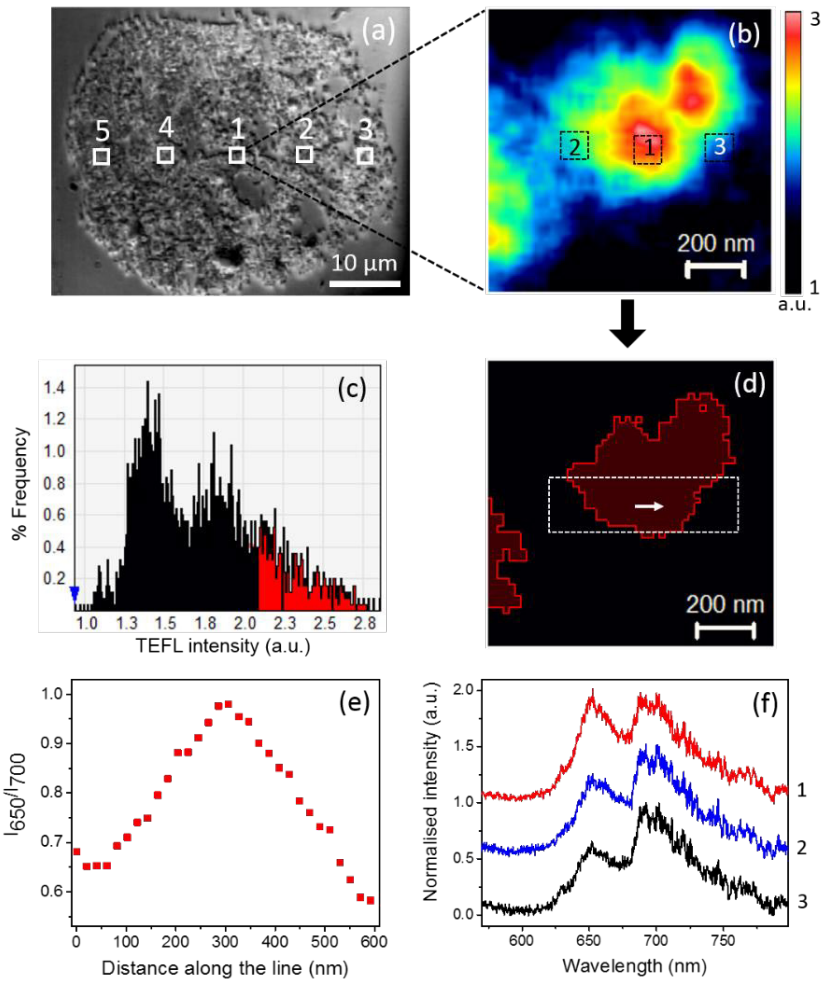

Fig. 5.4 (a) Optical image of a thin section of an industrially spent FCC particle (FCC1) placed on glass substrate. (b) TEFL acidity map obtained using the total intensity of the 650 nm and 700 nm TEFL bands measured in a 1 µm × 1 µm area marked as 1 in Fig. 5.4a. Nominal pixel size: 20 nm. Integration time: 1 s. Laser power: 365 µW. (c) Histogram of the TEFL intensity (I_{FL}) measured in the map shown in Fig. 5.4b. (d) Binary image of the most active zeolite regions in the TEFL map shown in Fig. 5.4b. (e) Profile of the average intensity ratio of the 650 nm and 700 nm TEFL bands (I_{650}/I_{700}) measured in the region marked in Fig. 5.4d along the direction of the arrow. (f) Average TEFL spectra from positions 1-3 marked in Fig. 5.4b. Spectra have been normalised and vertically shifted for easier visualisation.

are depicted in red. The TEFL intensity of these regions is marked in red in the histogram shown in Fig. 5.4c. From the binary image, the total area of the catalytically active regions in the TEFL map is calculated to be 0.34 μm^2. For simplicity, hereafter the most catalytically active areas in the TEFL maps will be simply referred to as the active zeolite domains.

We note that the relative intensity of the 650 nm and 700 nm bands varies inside the TEFL map shown in Fig. 5.4b. Thiophene oligomerisation over Brønsted acid sites is known to produce fluorescent species with different numbers of monomer units.[31] In particular, the limited availability of the Brønsted acid sites in zeolite domains has been shown to induce further oligomerisation of intermediate species leading to more conjugated carbocationic oligomers.[26] Furthermore, the emission wavelength of carbocationic species is positively correlated with their

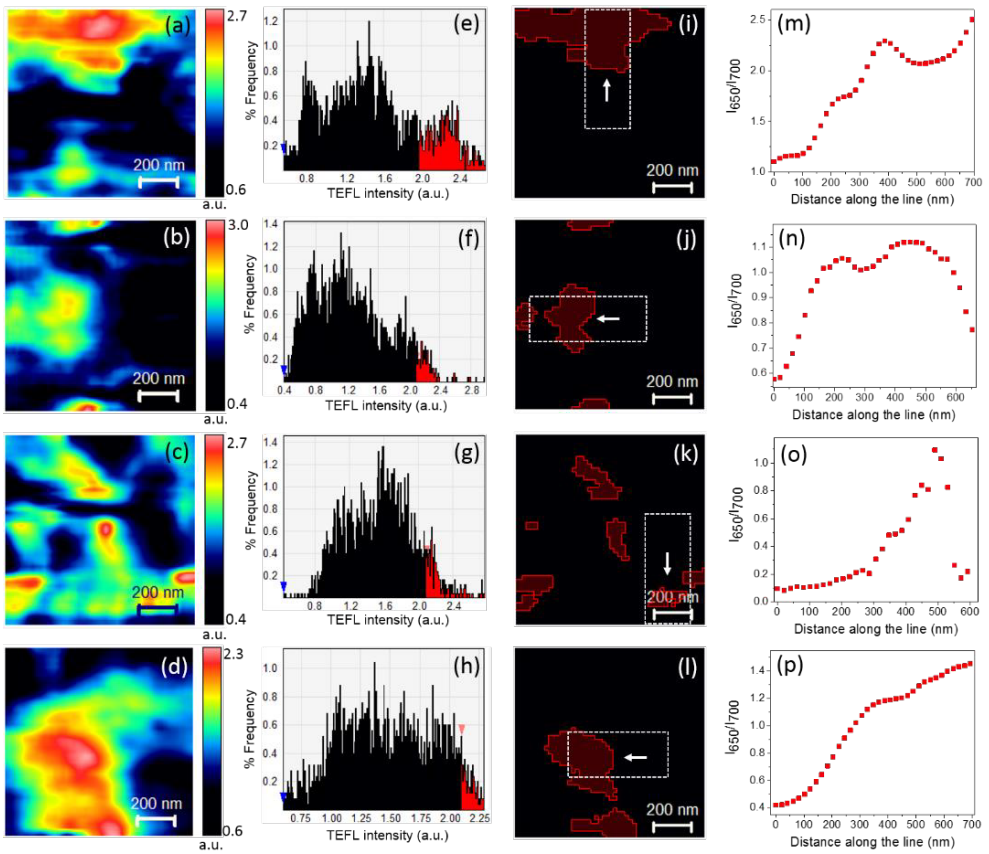

Fig. 5.5 (a) – (d) TEFL maps measured from 1 µm × 1 µm areas marked as 2 – 5 inside FCC1 shown in Fig. 5.4a. Nominal pixel size: 20 nm. Integration time: 1s. Laser power: 365 µW. (e) – (h) Histograms of the TEFL intensity measured in the maps shown in Fig. 5.5a – 5.5d, respectively. (i) – (l) Binary images of the most active zeolite regions in the TEFL maps shown in Fig. 5.5a – 5.5d. (m) – (p) Average intensity profiles of $_{650}/I_{700}$ in the regions marked in Fig. 5.5i – 5.5l along the direction of the arrow.

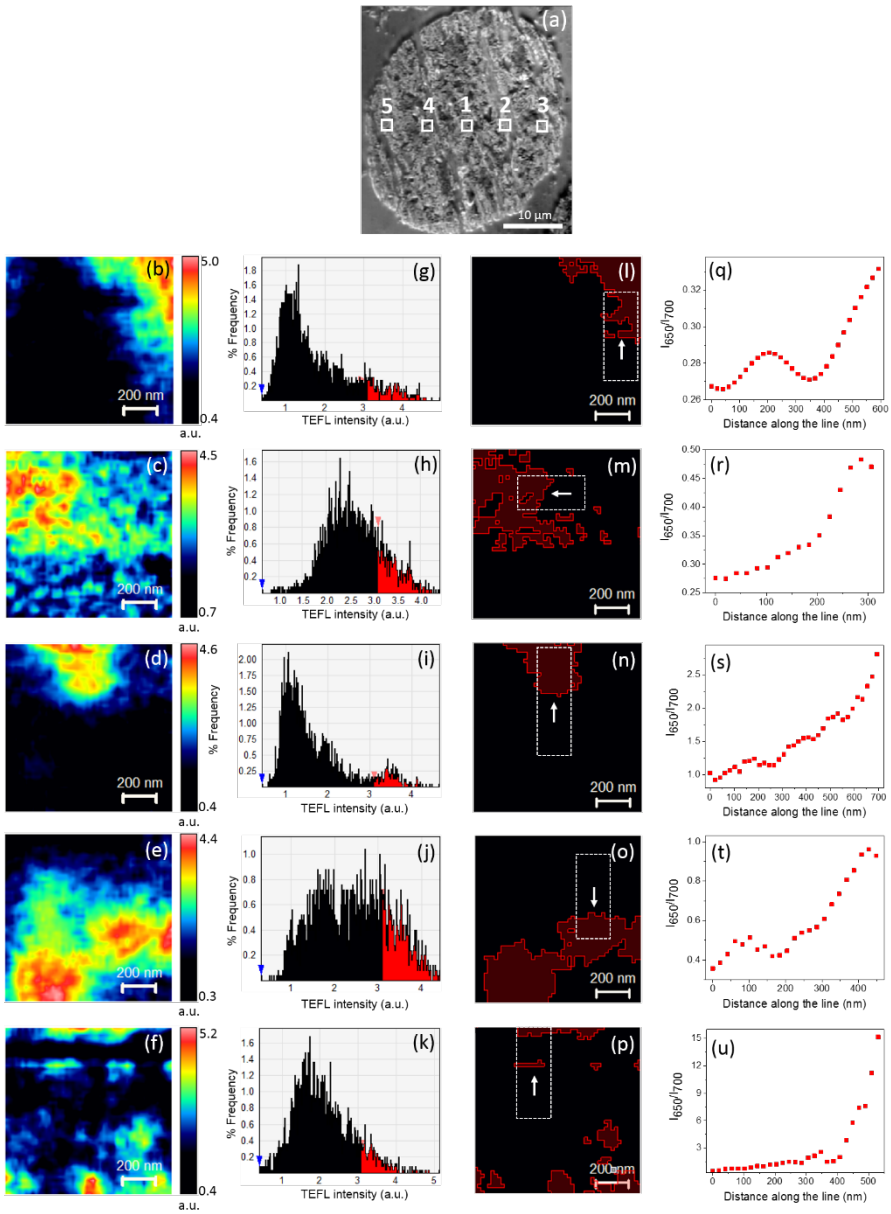

Fig. 5.6 (a) Optical image of the thin section of a second industrially used FCC particle (FCC2) on a glass substrate. (b) - (f) TEFL maps measured from 1 µm × 1 µm areas at locations 1 - 5, respectively on the FCC particle shown in Fig. 5.6a. Nominal pixel size: 20 nm. Integration time: 1s. Laser power: 365 µW. (g) - (k) Histograms of the TEFL intensity measured in the TEFL maps shown Fig. 5.6b – 5.6f, respectively. (l) - (p) Binary image of the most active zeolite regions in the TEFL maps shown in Fig. 5.6b – 5.6f, respectively. (q) - (u) Average intensity profiles of I_{650}/I_{700} in the regions marked in Fig. 5.6l – 5.6p, respectively along the direction of the arrow. I_{650}/I_{700} showed an increasing trend from the outside the active zeolite domains towards the centre.

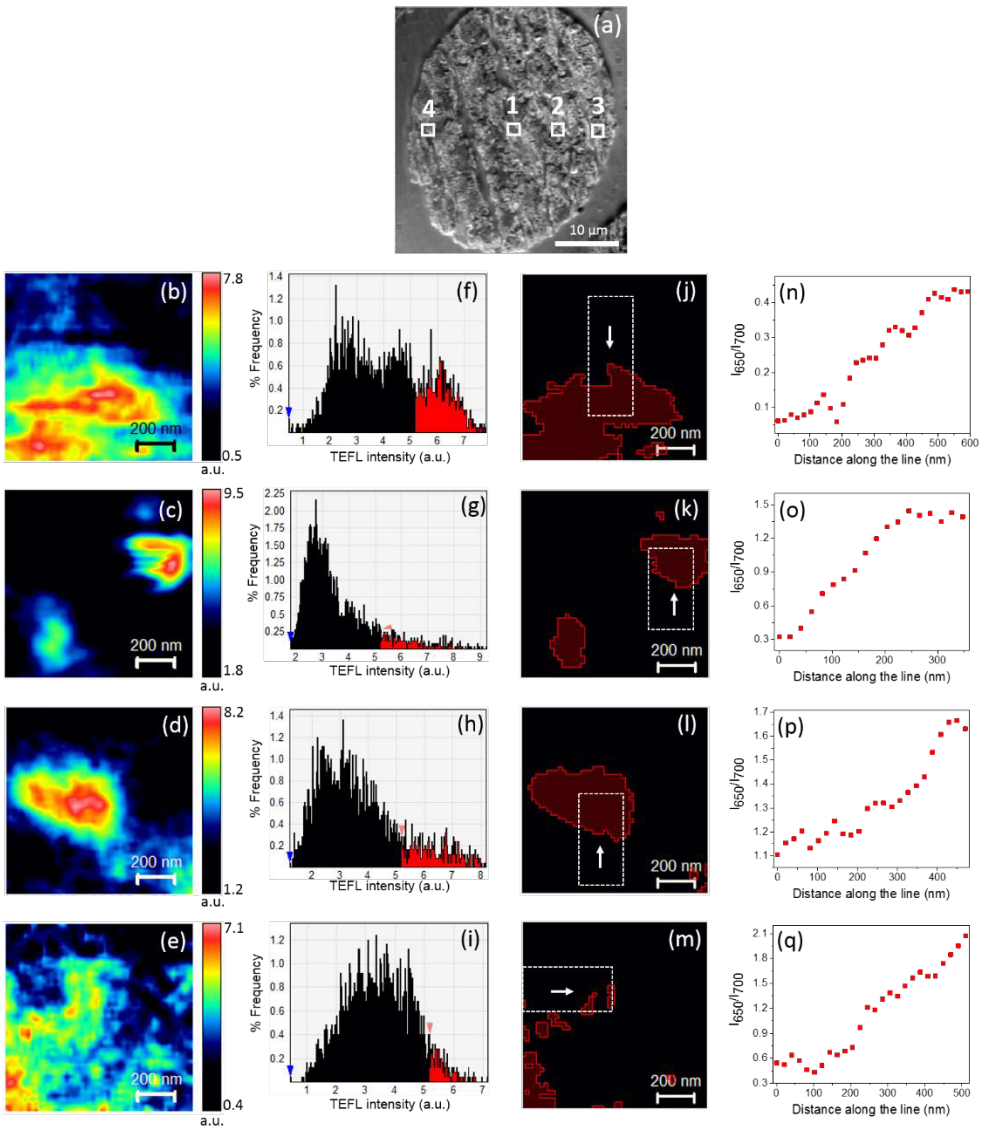

Fig. 5.7 (a) Optical image of the thin section of a third industrially used FCC particle (FCC3) on a glass substrate. (b) - (e) TEFL maps measured from 1 µm × 1 µm areas at locations 1 - 4, respectively on the FCC particle shown in Fig. 5.7a. Nominal pixel size: 20 nm. Integration time: 1s. Laser power: 365 µW. (f) - (i) Histograms of the TEFL intensity measured in the TEFL maps shown Fig. 5.7b – 5.7e, respectively. (j) - (m) Binary image of the most active zeolite regions in the TEFL maps shown in Fig. 5.7b –5.7e, respectively. (n) - (q) Average intensity profiles of I_{650}/I_{700} in the regions marked in Fig. 5.7j – 5.7m, respectively along the direction of the arrow. Similar to FCC1 and FCC2, I_{650}/I_{700} showed an increasing trend from the outside the active zeolite domains towards the centre.

length and conjugation.[26, 33] In other words, the 650 nm emission is more heavily associated with shorter oligomers compared to the 700 nm emission. From this we can deduce that the areas in the TEFL map exhibiting a relatively higher intensity ofthe 650 nm band contain a comparatively higher Brønsted acid site density. Fig. 5.4e shows the profile of the average intensity ratio of the 650 nm and 700 nm TEFL bands (I_{650}/I_{700}) measured in the regions marked in Fig. 5.4d along the direction of the arrow. In this plot, I_{650}/I_{700} shows an increasing trend from outside the zeolite domain to the centre. This trend is also directly evident from the average TEFL spectra plotted in Fig. 5.4f from locations A - C marked in Fig. 5.4b, in which a higher I_{650}/I_{700} is observed in the central region of the zeolite domain at location A compared to the outer regions at locations B and C. This implies that shorter conjugated carbocationic species are produced in the central part of the zeolite domain compared to the peripheral part, indicating that the central part of the zeolite domain contains a higher density of Brønsted acid sites and fewer mesopores. As more conjugated thiophene oligomers are formed in the outer regions of the zeolite domain this also implies that there is more space available to accommodate these fluorescent reaction products. Hence, it can be concluded that there is a mesoporosity gradient present from outer to inner regions of the zeolite domains.

For comparison, we have also carried out TEFL mapping in regions located off-centre (locations 2 and 4) and at the edge (locations 3 and 5) of the FCC particle shown in Fig. 5.4a. The TEFL maps measured at these locations are presented in Fig. 5.5a - 5.5d along with the corresponding histograms of their TEFL intensity (Fig. 5.5e - 5.5h). In these TEFL maps, the reactive regions were identified using the thresholding procedure described before and are presented as binary images in Fig. 5.5i – 5.5l. Average intensity profiles of I_{650}/I_{700} in the regions marked in Fig. 5.5i – 5.5l along the direction of the arrow are shown in Fig. 5.5m - 5.5p. Interestingly, the I_{650}/I_{700} ratio shows a general increasing trend from outside of the zeolite domains towards the centre in all four TEFL maps. This indicates that the distribution of the Brønsted acidity within zeolite domains follows a similar trend throughout the FCC particle irrespective of the location: the outer part of the zeolite domains contains fewer Brønsted acid sites and more mesopores than the central part.

To obtain statistical insights into the distribution of active zeolite domains and evaluate the reproducibility of our results, we performed similar TEFL measurements at centre, off-centre and edge region of two additional FCC particles (FCC2 and FCC3). The results for FCC2 and FCC3 are presented in Fig. 5.6 and 5.7, respectively. The areas of all active zeolite domains and their average TEFL activity measured in the three FCC particles are summarised in Tables 5.1 - 5.3, respectively. All TEFL maps in each FCC particle were measured using the same Ag coated TEFL probe and the TEFL measurements of all three FCC particles were performed using the TEFL probes prepared in the same batch. Following the same

Table 5.1 Area and average TEFL intensity of the active zeolite domains measured at different locations within FCC1 shown in Fig. 5.4 and 5.5.

Location of TEFL map	Active zeolite domains	Domain area (μm²)	Average TEFL intensity (a.u.)
1	1	0.175	2.48
	2	0.031	2.27
2	3	0.167	2.39
3	4	0.011	2.30
	5	0.057	2.19
	6	0.011	2.10
	7	0.010	2.49
4	8	0.025	2.29
	9	0.015	2.42
	10	0.003	2.16
	11	0.008	2.44
	12	0.016	2.36
	13	0.012	2.28
	14	0.007	2.15
5	15	0.082	2.14
	16	0.032	2.14

Table 5.2 Area and average TEFL intensity of the active zeolite domains at different locations within FCC2 shown in Fig. 5.6.

Location of TEFL map	Active zeolite domains	Domain area (μm²)	Average TEFL intensity (a.u.)
1	1	0.112	4.02
2	2	0.174	3.75
	3	0.002	3.18
	4	0.003	3.19
	5	0.003	3.25
	6	0.002	3.22
	7	0.005	3.25
3	8	0.090	3.88
4	9	0.247	3.76
5	10	0.025	3.90
	11	0.004	3.42
	12	0.014	3.48
	13	0.003	3.28
	14	0.007	3.76
	15	0.006	3.38
	16	0.019	4.15
	17	0.025	3.59

Table 5.3 Area and average TEFL intensity of the active zeolite domains at different locations within FCC3 shown in Fig. 5.7.

Location of TEFL map	Active zeolite domains	Domain area (μm^2)	Average TEFL intensity (a.u.)
1	1	0.265	6.51
	2	0.008	5.76
2	3	0.152	6.70
	4	0.002	5.39
	5	0.003	5.61
3	6	0.152	6.70
	7	0.002	5.39
	8	0.003	5.61
4	9	0.004	5.47
	10	0.004	5.61
	11	0.005	5.65
	12	0.005	6.00
	13	0.003	5.46
	14	0.036	6.21

analysis procedure used for FCC1 (Figures 2 and 3), a similar I_{650}/I_{700} ratio trend was observed for the zeolite domains irrespective of their location inside the FCC particles. All zeolite domains exhibited a lower density of Brønsted acid sites in the outer part compared to the central part. Since all three FCC particles were used in an industrial unit, this hierarchical distribution of Brønsted acidity most likely represents the local accessibility differences and/or the changes in framework aluminium content of zeolite domains during aging.

Based on the TEFL microscopy results, we compared intra- and inter-particle differences in the size of active zeolite domains. In the calculation of domain size, the areas < 0.002 μm^2 (corresponding to < 5 pixels), meeting the thresholding criterion were ignored. Histograms of the areas of active zeolite domains obtained from the TEFL maps measured at different locations in the three FCC particles are presented in Fig. 5.8 based on the analysis of 16, 17 and 14 active zeolite domains, respectively. Although areas of > 75 % of the active domains in all three FCC particles was < 0.04 μm^2 (corresponding spherical particle diameter: 127 nm), a significant variation in the zeolite domain size could be observed within individual FCC particles. The average areas of active zeolite domains measured within the individual FCC particles are plotted in Fig. 5.9a. Unlike the large intra-particle variation, the average areas of the active zeolite domains measured within each FCC particle are found to be rather similar. Fig. 5.9b shows the histogram of the areas of 47 active zeolite domains measured in all three FCC particles. 64 % of the active zeolite domains have an area < 0.02 μm^2, which corresponds to a

spherical particle of diameter 80 nm. This is smaller than the previously reported values of zeolite domain size measured in similar FCC particles using CFM (≈ 500 nm),[25] super-resolution optical fluctuation imaging (SOFI) (≈ 500 nm)[27] and scanning transmission X-ray microscopy (STXM) (≈ 400 nm).[34] This shows that the high spatial resolution as well as surface sensitivity offered by TEFL can successfully identify, localise the evaluate acidity and reactivity of individual zeolite domains within single FCC particles.

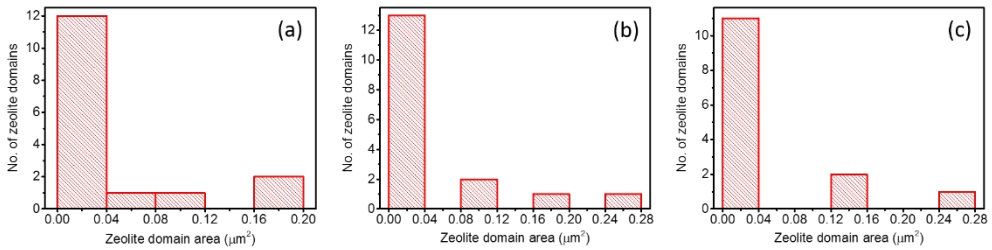

Fig. 5.8 Histograms of the areas of the active zeolite domains in (a) FCC1, (b) FCC2 and (c) FCC3.

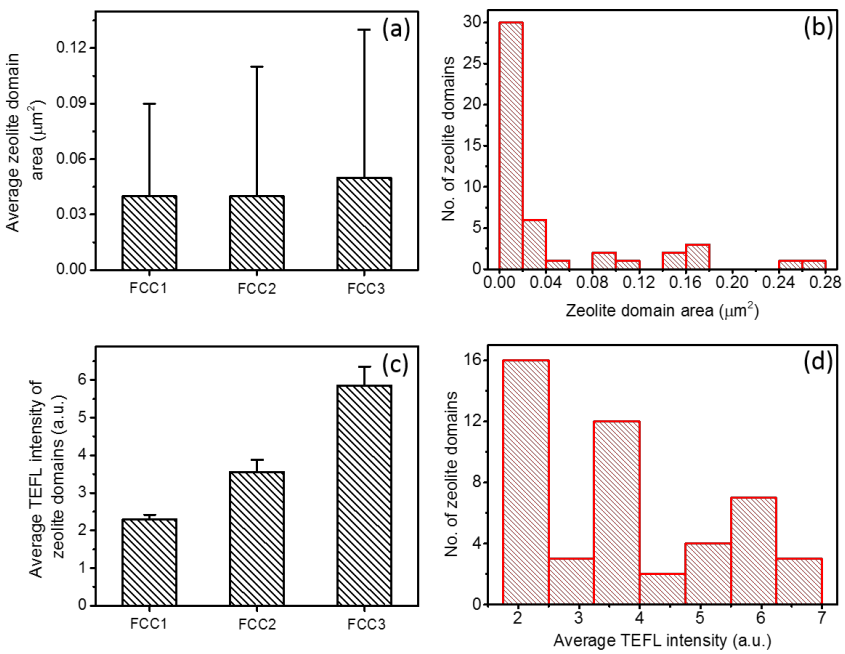

Fig. 5.9 (a) Average areas of active zeolite domains measured using TEFL microscopy in the three FCC particles. (b) Histogram of the areas of 47 active zeolite domains measured in all three FCC particles. (c) Average TEFL intensity measured within the active zeolite domains in the three FCC particles. (d) Histogram of the average TEFL intensity measured inside 47 active zeolite domains within all three FCC particles. Error bars in parts (a) and (c) represent the sample standard deviation.

An inter-particle comparison of the activity of 47 zeolite domains estimated from their average TEFL intensity is presented in Fig. 5.9c. Unlike zeolite domain size, a significant variation in the activity is observed across the three FCC particles. FCC1 shows a significantly lower average zeolite activity (average TEFL intensity: 2.3 ± 0.1 a.u.) compared to FCC2 (average TEFL intensity: 3.6 ± 0.3 a.u.) and FCC3 (average TEFL intensity: 5.9 ± 0.5 a.u.). This indicates that the Brønsted acidity varies significantly within the zeolite domains for the three FCC particles and is not necessarily related to the zeolite domain size (Fig. 5.9a). This is further substantiated by the plot of the areas of active zeolite domains versus their average TEFL intensity shown in Fig. 5.10. This plot indicates that the average TEFL intensity within the active zeolite domains measured in each FCC particle is independent of the domain size. A histogram of the total TEFL intensity measured in 47 zeolite domains across all three FCC particles is presented in Fig. 5.9d. The histogram reveals that 10 % of the most active zeolite domains have 3× higher TEFL intensity (6.4 ± 0.3 a.u.) compared to 10% of the least active zeolite domains (2.1 ± 0.1 a.u.), which points towards a significant inhomogeneity in the Brønsted acidity within these industrially used FCC particles.

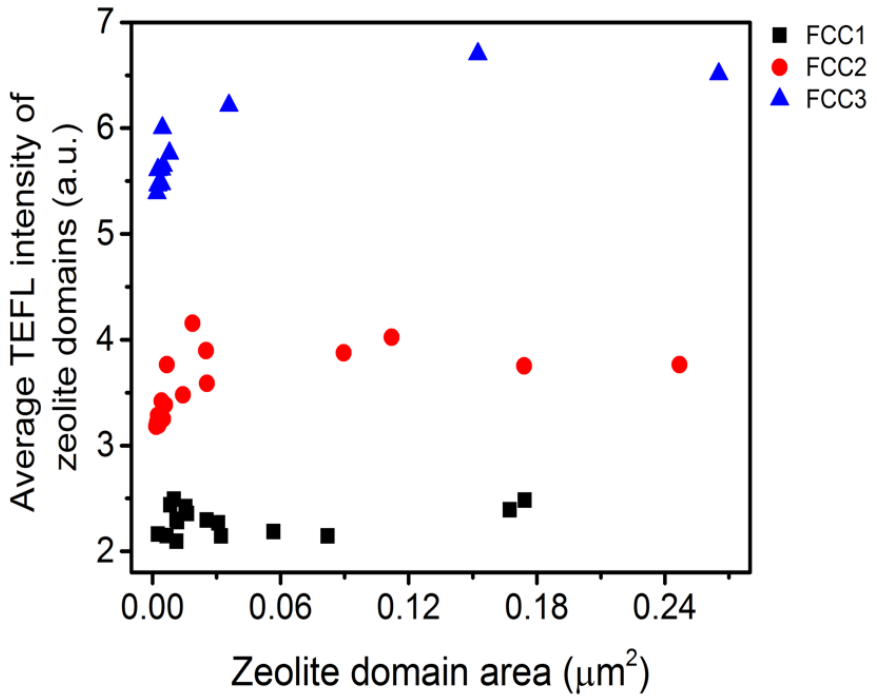

Fig. 5.10 Plot of the areas of active zeolite domains versus their average TEFL intensity within FCC particles 1 - 3.

Finally, we analysed the variation in the areas of active zeolite domains with respect to their position within the FCC particles. Fig. 5.11a shows a plot of the average area of active zeolite domains with respect to three different regions within FCC particles: centre, off-centre and edge. This plot reveals that the active zeolite domains located in the centre of the three FCC particles have a larger average size compared to the off-centre and edge regions. By contrast, the average TEFL intensity of the active zeolite domains is found to be largely independent of their location within the FCC particles (Fig. 5.11b). This suggests that zeolite deactivation within the FCC particles under study is not limited by mass transfer limitations or overall particle accessibility.

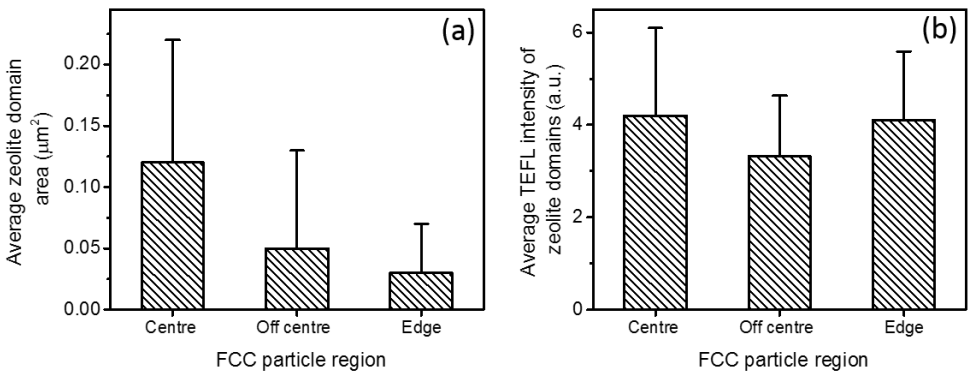

Fig. 5.11 Plots showing (a) the average area of active zeolite domains and (b) the average TEFL intensity of active zeolite domains with respect to the centre, off centre and edge regions of the three FCC particles.

5.4 Conclusions

We have presented the first application of TEFL microscopy in the field of heterogeneous catalysis. This has been accomplished by probing the acidity and reactivity of individual zeolite domains using a selective staining reaction within single FCC particles. The hyperspectral information gained from the TEFL maps revealed a spatial distribution of Brønsted acidity within the individual zeolite domains in different regions of the catalyst particles. We have also shown that sectioning of catalyst particles into thin layers is an effective strategy to investigate zeolite acidity in the central regions of the spherical particles, which are not easily accessible by super resolution fluorescence microscopy.[27] These results demonstrate that TEFL can be a powerful and sensitive characterisation tool to investigate industrially relevant single catalyst particles and reveal inter and intra-particle chemical variations with nanoscale spatial resolution. Such detailed insights into the variation in catalytic activity at nanometre length scales can help understand the degradation mechanisms of FCC particles used in an industrial

environment thereby facilitating the rational design of highly efficient and durable catalyst particles.

References

1. N. Mauser and A. Hartschuh, *Chem. Soc. Rev.*, 2014, **43**, 1248-1262.
2. S. Kawata and V. M. Shalaev, *Tip Enhancement*, Elsevier, Amsterdam, 2007.
3. T. Deckert-Gaudig, A. Taguchi, S. Kawata and V. Deckert, *Chem. Soc. Rev.*, 2017, **46**, 4077-4110.
4. P. Verma, *Chem. Rev.*, 2017, **117**, 6447-6466.
5. X. Wang, S.-C. Huang, T.-X. Huang, H.-S. Su, J.-H. Zhong, Z.-C. Zeng, M.-H. Li and B. Ren, *Chem. Soc. Rev.*, 2017, **46**, 4020-4041.
6. N. Kumar, S. Mignuzzi, W. Su and D. Roy, *EPJ Tech. Instrum.*, 2015, **2**, 9.
7. S. Najjar, D. Talaga, L. Schue, Y. Coffinier, S. Szunerits, R. Boukherroub, L. Servant, V. Rodriguez and S. Bonhommeau, *J. Phys. Chem. C*, 2014, **118**, 1174-1181.
8. S. Berweger, C. C. Neacsu, Y. Mao, H. Zhou, S. S. Wong and M. B. Raschke, *Nat. Nanotechnol.*, 2009, **4**, 496-499.
9. L. Xue, W. Li, G. G. Hoffmann, J. G. P. Goossens, J. Loos and G. de With, *Macromolecules*, 2011, **44**, 2852-2858.
10. X. Wang, D. Zhang, K. Braun, H. J. Egelhaaf, C. J. Brabec and A. J. Meixner, *Adv. Funct. Mater.*, 2010, **20**, 492-499.
11. E. M. van Schrojenstein Lantman, T. Deckert-Gaudig, A. J. G. Mank, V. Deckert and B. M. Weckhuysen, *Nat. Nanotechnol.*, 2012, **7**, 583-586.
12. R. Zhang, Y. Zhang, Z. C. Dong, S. Jiang, C. Zhang, L. G. Chen, L. Zhang, Y. Liao, J. Aizpurua, Y. Luo, J. L. Yang and J. G. Hou, *Nature*, 2013, **498**, 82-86.
13. Y. Okuno, Y. Saito, S. Kawata and P. Verma, *Phys. Rev. Lett.*, 2013, **111**, 216101.
14. W. Su and D. Roy, *J. Vac. Sci. Technol. B*, 2013, **31**, 041808.
15. A. J. Pollard, N. Kumar, A. Rae, S. Mignuzzi, W. Su and D. Roy, *J. Mater. Nanosci.*, 2014, **1**, 39-49.
16. W. Su, N. Kumar, S. Mignuzzi, J. Crain and D. Roy, *Nanoscale*, 2016, **8**, 10564-10569.
17. N. Kumar, A. Zoladek-Lemanczyk, A. A. Guilbert, W. Su, S. M. Tuladhar, T. Kirchartz, B. C. Schroeder, I. McCulloch, J. Nelson and D. Roy, *Nanoscale*, 2017, **9**, 2723-2731.
18. F. M. Huang, F. Festy and D. Richards, *Appl. Phys. Lett.*, 2005, **87**, 183101.
19. J. M. Gerton, L. A. Wade, G. A. Lessard, Z. Ma and S. R. Quake, *Phys. Rev. Lett.*, 2004, **93**, 180801.
20. C. Xie, C. Mu, J. R. Cox and J. M. Gerton, *Appl. Phys. Lett.*, 2006, **89**, 143117.
21. W. Vermeiren and J.-P. Gilson, *Top. Catal.* , 2009, **52**, 1131-1161.
22. E. T. C. Vogt and B. M. Weckhuysen, *Chem. Soc. Rev.*, 2015, **44**, 7342-7370.
23. I. L. C. Buurmans, J. Ruiz-Martínez, W. V. Knowles, D. van der Beek, J. A. Bergwerff, E. T. C. Vogt and B. M. Weckhuysen, *Nat. Chem.*, 2011, **3**, 862-867.
24. I. L. C. Buurmans, J. Ruiz-Martínez, S. L. van Leeuwen, D. van der Beek, J. A. Bergwerff, W. V. Knowles, E. T. C. Vogt and B. M. Weckhuysen, *Chem. Eur. J.*, 2012, **18**, 1094-1101.
25. C. Sprung and B. M. Weckhuysen, *Chem. Eur. J.*, 2014, **20**, 3667-3677.
26. G. T. Whiting, F. Meirer, D. Valencia, M. M. Mertens, A.-J. Bons, B. M. Weiss, P. A. Stevens, E. De Smit and B. M. Weckhuysen, *Phys. Chem. Chem. Phys.*, 2014, **16**, 21531-21542.
27. Z. Ristanović, M. M. Kerssens, A. V. Kubarev, F. C. Hendriks, P. Dedecker, J. Hofkens, M. B. J. Roeffaers and B. M. Weckhuysen, *Angew. Chem. Int. Ed.*, 2015, **54**, 1836-1840.
28. F. C. Hendriks, F. Meirer, A. V. Kubarev, Z. Ristanović, M. B. J. Roeffaers, E. T. C. Vogt, P. C. A. Bruijnincx and B. M. Weckhuysen, *J. Am. Chem. Soc.*, 2017, **139**, 13632-13635.
29. F. C. Hendriks, S. Mohammadian, Z. Ristanović, S. Kalirai, F. Meirer, E. T. C. Vogt, P. C. A. Bruijnincx, H. C. Gerritsen and B. M. Weckhuysen, *Angew. Chem. Int. Ed.*, 2018, **57**, 257-261.

30. J. Van Loon, K. P. F. Janssen, T. Franklin, A. V. Kubarev, J. A. Steele, E. Debroye, E. Breynaert, J. A. Martens and M. B. J. Roeffaers, *ACS Catal.*, 2017, **7**, 5234-5242.
31. S. C. Rasmussen, S. J. Evenson and C. B. McCausland, *Chem. Commun.*, 2015, **51**, 4528-4543.
32. N. Kumar, A. Rae and D. Roy, *Appl. Phys. Lett.*, 2014, **104**, 123106.
33. M. H. F. Kox, A. Mijovilovich, J. J. H. B. Sättler, E. Stavitski and B. M. Weckhuysen, *ChemCatChem*, 2010, **2**, 564-571.
34. S. Kalirai, P. P. Paalanen, J. Wang, F. Meirer and B. M. Weckhuysen, *Angew. Chem. Int. Ed.*, 2016, **55**, 11134-11138.

Chapter 6

Summary and Outlook

6.1 Summary

This PhD Thesis has primarily focussed on the further development of atomic force microscopy (AFM) based tip-enhanced Raman spectroscopy (TERS) as a robust analytical tool for heterogeneous catalysis research. Compared to the scanning tunnelling microscopy (STM) based TERS, which is limited by the requirement of a conductive substrate, AFM based TERS, in principle is far more versatile and could be used for nanoscale chemical characterisation of almost any sample surface and in any environment. Therefore, AFM based TERS is better poised for various applications in heterogeneous catalysis research. Most of the development undertaken during the course of this PhD project is related to the metal coated TERS probes – which are the very heart of a TERS experiment. A number of technical challenges regarding TERS probes were identified and addressed. In particular, we attempted to tackle scientific problems in the following areas:

1. **Understanding plasmonic degradation of TERS probes:** a) How quickly do Ag coated TERS probes undergo plasmonic degradation? b) Can this degradation be controlled? c) What is the mechanism of degradation?
2. **Enhancing stability of TERS probes in a liquid environment:** a) How can Ag coated TERS probe be made more stable in a liquid environment? b) How does the plasmonic signal enhancement of a TERS probe inside a liquid environment compare with the ambient? c) Do the TERS probes provide similar plasmonic signal enhancement on different substrates in a liquid? d) Why do TERS probe behave differently in liquid? e) Is it possible to perform nanoscale chemical imaging at a solid-liquid interface using TERS?
3. **Extending the plasmonic lifetime of TERS probes:** a) Is it possible to extend the plasmonic lifetime of TERS probes? b) Is it possible to improve the chemical inertness of TERS probes for monitoring of catalytic reactions? c) Is it possible to carry out nanoscale chemical mapping of a catalytic reaction on a heterogeneous catalyst substrate in a liquid environment using TERS?
4. **Applying tip-enhanced signal enhancement to real life catalysts:** a) Is it possible to enhance fluorescence signals using localised surface plasmon resonance (LSPR) at a metal coated AFM probe? b) Can this enhancement be used for investigation of real life (industrially used) catalysts?

Rapid degradation of TERS probes, especially those coated with Ag, is a major bottleneck to the widespread uptake of this technique and severely prohibits the success of many TERS experiments. A better understanding of the plasmonic degradation of TERS probes was gained in Chapter 2 by conducting a systematic time-series study of the plasmonic degradation of Ag coated TERS probes under

different environmental conditions for the first time. Plasmonic enhancement of Raman signals by the TERS probes was found to decrease rapidly within the first 4 h of exposure to the ambient environment, disappearing completely within 8 h. A significant improvement in the plasmonic lifetime of TERS probes, from a few hours to a few months, was observed under a low oxygen (< 1 ppm) and a low moisture (< 1 ppm) environment. The cause of the plasmonic degradation was identified using time-series X-ray photoelectron spectroscopy (XPS) measurements on Ag nanoparticles. A rapid oxidation occurring on the surface of Ag nanoparticles within 4 h of exposure to the ambient environment was revealed, which correlated negatively with the plasmonic enhancement of TERS tips under similar conditions. No sulphur was detected in any of the XPS spectra indicating that oxide film formation is the dominant cause of rapid plasmonic degradation of Ag coated TERS probes. Based on the results of this study, practical strategies were developed for the maximum preservation of the plasmonic activity of TERS probes during storage and use.

For *in situ* monitoring of catalytic reactions, TERS has to work in both air and liquid environments. However, current metal coated TERS probes are unsuitable for operation in the liquid phase due to the lack of structural stability. Furthermore, because of the lack of robust TERS probes, the plasmonic enhancement of Raman signals in a liquid environment on both metal (gap mode) and dielectric substrates (non-gap mode) is poorly understood. These issues were addressed in Chapter 3, where we successfully developed highly stable TERS probes in a liquid environment utilising a unique multi-layer metal coating strategy. Using these novel probes, we have carried out the first comparative study of TERS signal enhancement in air and liquid environment on both dielectric and metal substrates. Plasmonic enhancement was found to decrease in an aqueous environment compared to air in both gap mode and non-gap mode TERS configurations. To understand the cause of TERS signal in a liquid environment we performed numerical simulations, which revealed a negative correlation between electric field enhancement at the TERS probe-apex and the refractive index of the surrounding medium. Finally, using the highly robust TERS probes we demonstrated sub-30 nm resolution chemical mapping in a liquid environment using TERS for the first time with single wall carbon nanotubes as a model system, thereby bringing TERS a step closer to being used as routine analytical tool for nanoscale characterisation of catalytic reactions in both air and liquid environments.

In order to monitor catalytic reactions effectively, TERS probes need to be chemically inert and robust enough to withstand harsh chemical environments. Furthermore, the lifetime of the TERS probes should be long enough for them to be used for an extended period of time. These issues were addressed in Chapter 4, where we developed a unique method of protecting TERS probes with an ultrathin

(1 nm - 5 nm) coating of zirconia. The zirconia protection led to more than 850-fold increase in the lifetime of TERS probes together with a drastic improvement in their structural stability in water. The pinhole free zirconia coating effectively blocked the contact of silver with oxygen and moisture from the ambient environment thereby persevering the plasmonic activity of TERS probes while at the same time rendering them chemically inert for the investigation of catalytic reactions. Finally, we demonstrated the potential of TERS for spatially resolved mapping of a catalytic reaction over a heterogeneous catalyst substrate in a liquid environment using pATP → DMAB as a model reaction for the first time. The reaction products were mapped with a nanoscale spatial resolution demonstrating the high chemical sensitivity and spatial resolution of TERS for monitoring catalytic reactions. With a dramatic improvement in the probe lifetime and structural and chemical stability, this work paves the way for using AFM-TERS as a non-destructive, label-free analytical tool for nanoscale molecular characterisation of almost any catalyst surface and within any environment.

In Chapter 5, we explored if in addition to the Raman signals, fluorescence signals could also be enhanced in the near-field of a Ag coated AFM probe thereby introducing tip-enhanced fluorescence (TEFL) microscopy as a new tool for heterogeneous catalysis research. Industrially spent multicomponent fluid catalytic cracking (FCC) catalyst was used a showcase to demonstrate the potential of TEFL microscopy for investigation of catalytic activity in real life catalyst samples. We showed that sectioning of FCC particles into thin layers is an effective strategy to investigate zeolite acidity in the central regions of solid spherical FCC particles, which are not easily accessible by other super-resolution fluorescence microscopy techniques. Using selective staining of Brønsted acidity in thin sections of FCC samples with thiophene oligomerisation as a probe reaction, we performed high-resolution TEFL mapping of different regions of the FCC catalysts. Hyperspectral information gained *via* TEFL microscopy revealed a hierarchical distribution of Brønsted acidity within individual zeolite domains in different regions of a single FCC catalyst particle. The comparison of TEFL measurements from different FCC particles showed a significant intra- and inter-particle heterogeneities in zeolite domain size and activity, which demonstrated that TEFL microscopy is a powerful and sensitive tool to investigate distribution of zeolite acidity at nanometre length-scales within real-life FCC particles with direct industrial relevance.

6.2 Outlook

With the substantial progress in the plasmonic lifetime, chemical inertness and stability in a liquid environment of the TERS probes and the associated case

studies of model and real life catalytic systems demonstrated in this PhD project, TERS is now ready to be used as a more routine analytical tool for heterogeneous catalysis research. A number of TERS applications to study catalytic systems could now be envisaged.

As the case study of the nanoscale characterisation of pATP → DMAB using TERS in Chapter 4 has demonstrated, the strong localised surface plasmon resonance in the nanogap between a TERS probe and metal substrate can open up possibilities of studying molecular transformations on single catalyst particles with different shapes, sizes and crystal orientations placed at a TERS probe-apex in both air and liquid environments. The LSPR generated at the TERS probe-apex can act as a sensitive probe to monitor the structural changes of adsorbed reactants elucidating structure-performance relationships for efficient catalytic conversion and rational catalyst design.

To correlate structure of catalytic particles with their catalytic activity, spatially resolved TERS studies of more defined catalytic systems could be undertaken. The spatial resolution of chemical imaging using TERS has been shown to reach a few nm under ambient conditions. Therefore, catalyst particles with a size spanning the entire nanoscale range (1 nm - 100 nm) could be investigated using TERS.

The TERS probes developed in this work have proved to be highly robust even under harsh chemical environments. Therefore, nanoscale monitoring of catalytic reactions using TERS under operando conditions could be performed. The TERS probe and the excitation laser could be enclosed in a specially designed reaction cell and catalytic reactions under high temperature/pressure and different gas and liquid flow conditions could be monitored with high chemical sensitivity.

The spatial resolution of TERS imaging of the catalytic and non-catalytic systems undertaken in this PhD Thesis has been limited by the pixel size. As mentioned above, TERS imaging with spatial resolution reaching a few nm is now becoming rather routine. Therefore, very high-resolution characterisation of catalytic systems is possible using sub-nm pixel size.

As demonstrated in the last chapter of this PhD Thesis, TEFL microscopy is a powerful tool to investigate real life catalysts such as FCC particles. TERS/TEFL studies of similar multicomponent catalytic systems could be undertaken which can provide significant insights into the catalytic heterogeneity of such systems at nanometer length-scales. Furthermore, comparative studies of catalysts used in the industrially units with the fresh catalysts using TERS/TEFL microscopy could enhance the understanding of their degradation mechanisms.

Chapter 7

Samenvatting en Vooruitblik

7.1 Samenvatting

Het onderzoek beschreven in dit proefschrift richt zich voornamelijk op de ontwikkeling van atoomkrachtmicroscopie (AFM)-gebaseerde tip-versterkte Raman spectroscopie (TERS) als een robuuste analytische methode voor onderzoek aan heterogene katalysatoren. Vergeleken met scanning tunneling microscopie (STM)-gebaseerde TERS is AFM-gebaseerde TERS in principe veelzijdiger, aangezien er geen geleidend substraat nodig is waardoor AFM-TERS gebruikt zou kunnen worden voor chemische onderzoek op de nanoschaal van bijna elk oppervlak en in bijna elke omgeving. De meeste ontwikkelingen die gedaan zijn in dit proefschrift betreffen de metaal-gecoate naalden waarop TERS experimenten gebaseerd zijn. Een aantal technische uitdagingen met betrekking tot deze scherpe naalden zijn beschreven en daarna aangepakt. In het bijzonder hebben we de volgende wetenschappelijke vraagstukken onderzocht:

1. **Het begrijpen van de plasmonische degradatie van de TERS naalden:** a) Hoe snel ondergaan Ag-gecoate TERS naalden plasmonische degradatie? b) Kan deze degradatie gecontroleerd worden? en 3) Wat is het onderliggende degradatiemechanisme?
2. **Verbeteren van de stabiliteit van TERS naalden in vloeistoffen:** a) Hoe kunnen Ag-gecoate TERS naalden stabieler gemaakt worden in vloeistoffen? b) Hoe verhoudt de plasmonische signaalversterking zich in vloeistoffen tot die in de lucht? c) Verschaffen TERS naalden vergelijkbare plasmonische signaalversterking op verschillende substraten in een vloeistof? d) Waarom gedragen TERS naalden zich anders in vloeistoffen? e) Is het mogelijk om met behulp van TERS nanoschaal chemische beeldvorming te verrichten op vast-vloeibaar grensvlakken?
3. **Verlengen van de plasmonische levensduur van de TERS naalden:** a) Is het mogelijk om de plasmonische levensduur van TERS naalden te verlengen? b) Is het mogelijk om de TERS naalden chemisch inert te maken zodat ze toegepast kunnen worden voor katalytische reacties? c) Kunnen TERS naalden gebruikt worden om een katalytische reactie op een katalysatoroppervlak in een vloeistof te kunnen volgen?
4. **Toepassen van tip-enhanced signaalversterking op echte katalysatoren:** a) Is het mogelijk om fluorescentiesignalen te versterken aan een metaal-gecoate TERS naald? b) Kan deze versterking gebruikt worden voor onderzoek aan realistische katalysatormaterialen?

Snelle degradatie van TERS naalden, en in het bijzonder die gemaakt van zilver, is een van de knelpunten voor de wijdverspreide toepassing van TERS en verhindert het succes van menig TERS experiment. Beter begrip van de

plasmonische degradatie van TERS naalden is verkregen in Hoofdstuk 2 door voor de eerste keer een systematische tijdserie studie uit te voeren van de plasmonische degradatie van zilver-gecoate naalden in verschillende omgevingen. De plasmonische versterking van de TERS naalden verslechterde erg snel binnen 4 uur na blootstelling aan de omgevingslucht en verdween helemaal binnen 8 uur. Een significante verbetering in de plasmonische levensduur van TERS naalden werd geobserveerd voor naalden die onder een laag zuurstofgehalte (< 1 ppm) en laag vochtgehalte (< 1 ppm) bewaard werden. De oorzaak van de plasmonische degradatie werd geïdentificeerd met behulp van tijdseries Röntgen fotoelectrospectroscopie (XPS) metingen aan zilver nanodeeltjes. Deze ondergingen degradatie aan het oppervlak binnen 4 uur na blootstelling aan de omgeving, wat negatief correleert met de plasmonische versterking van TERS naalden onder vergelijkbare condities. In geen enkel TERS spectrum werd zwavel gedetecteerd, wat betekent dat het vormen van een oxidefilm de belangrijkste oorzaak is van de snelle plasmonische degradatie van zilver-gecoate TERS naalden. Gebaseerd op deze resultaten konden er praktische strategieën ontwikkeld worden om de plasmonische activiteit van de TERS naalden maximaal te behouden tijdens het bewaren en het gebruik.

Om *in situ* katalytische reacties te kunnen volgen moet de TERS techniek werken in zowel lucht alsook in vloeistoffen. Door het gebrek aan structurele stabiliteit is dit echter niet mogelijk met de huidige metaal-gecoate TERS naalden. Verder is er door het gebrek aan robuuste TERS naalden weinig kennis over de plasmonische versterking van Raman signalen in vloeistoffen op zowel metaal (*gap mode*) als dielektrische substraten (*non-gap mode*). Deze zaken worden bestudeerd in Hoofdstuk 3, waarin we laten zien dat we door middel van een multilaagse metaalcoating strategie succesvol TERS naalden hebben ontwikkeld voor gebruik in vloeistoffen. Met deze naalden hebben we vervolgens de eerste vergelijkende studie uitgevoerd van TERS signalen in lucht en water in zowel *gap mode* als *non-gap mode* opstellingen. Om het TERS signaal in een vloeistof te kunnen verklaren hebben we numerieke simulaties uitgevoerd, die lieten zien dat er een negatieve correlatie is tussen de versterking van het elektrische veld in het puntje van de naald en het omringende medium. Als laatst hebben we laten zien dat we met deze robuuste TERS naalden *single wall carbon nanotubes* in een vloeistof chemisch in kaart hebben kunnen brengen met een resolutie van minder dan 30 nm. Dit brengt het gebruik van TERS als routine analysetechniek voor nanoschaal karakterisatie in zowel lucht als water een stap dichterbij.

Om katalytische reacties te kunnen volgen, moeten de TERS naalden chemisch inert en robuust genoeg zijn om agressieve chemische milieus te kunnen weerstaan. Verder moet de levensduur van de TERS naalden zodanig zijn dat ze gebruikt kunnen worden over langere periodes. Deze problemen zijn aangepakt in

Hoofdstuk 4. In dit hoofdstuk hebben we een unieke methode ontwikkeld om TERS naalden te beschermen door middel van een ultradunne (1 nm - 5 nm) laag zirconia. De zirconiabescherming leidt tot een 850-voudige verlenging van de levensduur, die gepaard gaat met een drastische verbetering in de structurele stabiliteit in water. De homogene laag van zirconia blokkeert effectief het contact van zilver met zuurstof en vocht uit de omgeving, zodat de plasmonische activiteit behouden blijft, en bovendien ervoor zorgt dat de naalden chemisch inert zijn. Zodoende kan TERS dus gebruikt kunnen worden in katalytische reacties. Als laatst demonstreren we de mogelijkheden van TERS door de modelreactie pATP → DMAB voor de eerste keer in kaart te brengen op een heterogeen katalysatoroppervlak in een waterige omgeving. De reactieproducten konden bestudeerd worden met een resolutie van < 15 nm, wat de hoge chemische gevoeligheid en spatiële resolutie van TERS om katalytische reacties te kunnen volgen demonstreert. De enorme verbetering van de levensduur, structurele stabiliteit en chemische stabiliteit van de TERS naalden maken het mogelijk om de AFM-TERS methodiek te gebruiken als een niet-destructieve, labelvrije analytische methode om vrijwel elk katalysatoroppervlak in vrijwel elk medium op nanoschaal te karakteriseren.

In Hoofdstuk 5 hebben we onderzocht of we naast Raman signalen ook fluorescentie signalen konden versterken met TERS naalden en op die manier hebben we tip-versterkte fluorescentie (TEFL) microscopie geïntroduceerd als een nieuwe karakteriseringstechniek in het domein van de heterogene katalyse. Industrieel gebruikte *fluid catalytic cracking* (FCC) katalysatoren, die zeolieten bevatten, zijn gebruikt als voorbeeldmateriaal om de mogelijkheden van TEFL microscopie in onderzoek naar de katalytische activiteit in industriële katalysatoren te demonstreren. We hebben laten zien dat het snijden van FCC deeltjes in dunne secties een effectieve manier is om de zuurheid van een zeoliet in de centrale regio's van een FCC deeltje te onderzoeken, wat slechts mogelijk is met andere superresolutie fluorescentie microscopietechnieken. Door het selectief markeren van de Brønsted zuurheid in deze dunne secties via thiopheen oligomerisatie konden we met TEFL microscopie de verschillende gebieden van de FCC katalysatoren in kaart brengen. Hyperspectrale informatie verkregen met TEFL microscopie onthulde een hiërarchische distributie van Brønsted zuurheid in individuele zeolietdomeinen in verschillende regio's van een enkel FCC katalysatordeeltje. Vergelijking van de TEFL metingen tussen de verschillende FCC deeltjes liet zien dat er belangrijke intra- en interdeeltje heterogeniteiten bestaan in zowel de zeolietdomeingrootte als de activiteit van deze zeolietdomeinen. Dit bewijst dat TEFL microscopie niet enkel een krachtige, maar ook een gevoelige manier is om op de nanometerschaal zuurheid van zeolietdomeinen in een FCC deeltje te onderzoeken.

7.2 Vooruitblik

Met de grote voortgang in de plasmonische levensduur, chemische inertheid en stabiliteit in de vloeistoffen van de scherpe naalden voor TERS en de daarmee geassocieerde voorbeeldstudies van zowel modelkatalysatoren als meer realistische katalysatorsystemen, die beschreven worden in dit proefschrift, is TERS nu klaar om als standaard analytische techniek in heterogene katayse gebruikt te worden. Een aantal voorbeelden worden genoemd voor de toepassing van TERS in het onderzoeksdomein van katalyse.

Zoals de voorbeeldstudie in Hoofdstuk 4 heeft laten zien door de pATP → DMAB reactie op nanoschaal te karakteriseren, kan de versterking in een nanoholte tussen een TERS naald en een metaal substraat de mogelijkheid geven om moleculaire omzettingen op enkele katalysatordeeltjes met verschillende vormen, groottes en kristaloriëntaties te bestuderen door deze deeltjes onder de naald te leggen, zowel in lucht als water. Het gelokaliseerd plasmon resonantie effect, dat gegenereerd kan worden op het uiteinde van de scherpe TERS naald kan als gevoelige sensor gebruikt worden om structurele veranderingen van geadsorbeerde reactanten te volgen, wat structuur-activiteitsrelaties kan ophelderen om efficiënte katalytische conversie en rationeel ontwerp van katalysatoren te bewerkstelligen.

Om de structuur van katalysatordeeltjes te correleren aan hun katalytische activiteit, kunnen goed gedefinieerde katalytische systemen onderzocht worden met plaats-opgeloste TERS metingen. We hebben laten zien dat de spatiële resolutie voor chemische beeldvorming in de lucht met TERS slechts een aantal nanometer kan bedragen. Dat betekent dat katalysatoren met afmetingen over de hele nanoschaal (1 nm - 100 nm) onderzocht kunnen worden met de TERS techniek.

We hebben in dit onderzoekswerk ook bewezen dat de ontwikkelde TERS naalden robuust zijn en gebruikt kunnen worden onder agressieve chemische omstandigheden. Dat betekent dat we deze ook kunnen gebruiken voor het volgen van *operando* katalytische processen op de nanoschaal. De TERS naald en de excitatielaser zouden in een speciaal daarvoor ontworpen reactiecel geplaatst kunnen worden, waardoor katalytische reacties onder hoge temperatuur/druk en met verschillende gassen en vloeistof stroomcondities gevolgd kunnen worden met hoge chemische gevoeligheid.

De spatiële resolutie van TERS beeldvorming van katalytische en niet-katalytische systemen bediscussieerd in dit proefschrift was beperkt door de *pixel* grootte van het TERS systeem. Zoals eerder genoemd wordt de TERS beeldvorming met een resolutie van slechts enkele nanometers inmiddels routine. Daardoor zou de karakterisering met ultrahoge resolutie mogelijk worden als een systeem met subnanometer *pixel* grootte gebruikt wordt.

Zoals gedemonstreerd in het laatste hoofdstuk van dit proefschrift kan TEFL

microscopie gebruikt worden als een krachtige meettechniek om praktisch gebruikte katalysatoren zoals FCC deeltjes te karakteriseren. TERS/TEFL studies kunnen belangrijke nieuwe inzichten verschaffen in de katalytische heterogeniteit op de nanoschaal van vergelijkbare katalytische systemen die uit meerdere componenten bestaan. Verder kunnen reeds gebruikte katalysatoren uit de chemische industrie vergeleken worden met verse katalysatoren door middel van TERS/TEFL om hun degradatiemechanisme te ontrafelen.

Publications and Presentations

PhD Publications in Peer-Reviewed Scientific Journals

"Tip-enhanced Raman spectroscopy: Principles and Applications" **N. Kumar**, S. Mignuzzi, W. Su, D. Roy, *EPJ Tech. Instrum.* 2015, 2, 9 (Chapter 1)

"Nanoscale Mapping of Catalytic Activity using Tip-enhanced Raman Spectroscopy" **N. Kumar**, B. Stephanidis, R. Zenobi, A. J. Wain, D. Roy*, Nanoscale* 2015, 7, 7133-7137 (Chapter 1)

"Surface- and Tip-Enhanced Raman Spectroscopy in Catalysis" T. Hartman, C. S. Wondergem, **N. Kumar**, A. van den Berg and B. M. Weckhuysen *J. Phys. Chem. Lett.* 2016, 7, 1570-1584 (Chapter 1)

"Extending the Plasmonic Lifetime of Tip-enhanced Raman Spectroscopy Probes" **N. Kumar**, S. J. Spencer, A. J. Wain, D. Imbraguglio, A. Rossi, B. M. Weckhuysen, D. Roy, *Phys. Chem. Chem. Phys.* 2016, 18, 13710-13716 (Chapter 2)

"Nanoscale Chemical Imaging of Solid-liquid Interfaces using Tip-enhanced Raman Spectroscopy" **N. Kumar**, W. Su, M. Veselý, B. M. Weckhuysen, A. J. Pollard, A. J. Wain, *Nanoscale*, 2018, 10, 1815-1824 (Chapter 3)

"*In Situ Nanoscale Mapping of Catalytic Reactions in the Liquid Phase using Tip-enhanced Raman Spectroscopy*" **N. Kumar**, C. S. Wondergem, A. J. Wain, B. M. Weckhuysen, 2018, submitted for publication (Chapter 4)

"*Nanoscale Chemical Imaging of a Single Catalyst Particle with Tip-enhanced Fluorescence Microscopy*" **N. Kumar**, S. Kalirai, A. J. Wain, B. M. Weckhuysen, *ChemCatChem*, 2018, DOI: 10.1002/cctc.201801023 (Chapter 5)

Other Publications in Peer-Reviewed Scientific Journals

"*Simultaneous Topographical, Electrical and Optical Microscopy of Optoelectronic Devices at the Nanoscale*" **N. Kumar**, A. Zoladek-Lemanczyk, A. Gilbert, S. M. Tuladhar, T. Kirchartz, B. C. Schroeder, I. McCulloch, J. Nelson, D. Roy, F. A. Castro, *Nanoscale*, 2017, 9, 2723-2731

"*Nanoscale Mapping of Newly-synthesised Phospholipid Molecules in a Biological Cell using Tip-enhanced Raman Spectroscopy*" **N. Kumar**, M. M. Drozdz, H. Jiang, D. M. Santos, D. J. Vaux, *Chem. Commun.,* 2017, 53, 2451-2454

"*Nanoscale Mapping of Excitonic Processes in Single-layer MoS_2 using Tip-enhanced Photoluminescence Microscopy*" W. Su*, **N. Kumar***, S. Mignuzzi, J. Crain, D. Roy, *Nanoscale,* 2016, 8, 10564-10569 (*Equal contribution)

"*Nanoscale Chemical Mapping of Intrinsic Defects in Graphene using Tip-enhanced Raman Spectroscopy*" W. Su*, **N. Kumar***, N. Dai, D. Roy, *Chem. Commun*., 2016, 52, 8227-8230 (*Equal contribution)

"*Probing Individual Point Defects in Graphene via Near-field Raman Scattering*" S. Mignuzzi, **N. Kumar**, B. Brennan, I. S. Gilmore, D. R. Richards, A. J. Pollard, D. Roy, *Nanoscale*, 2015, 9, 19413-19418

"*Transforming Bilayer MoS_2 into Single-layer with Strong Photoluminescence using UV-ozone Oxidation*" W. Su, **N. Kumar**, S. J. Spencer, N. Dai, D. Roy, *Nano Res.,* 2015, 8, 3878-3886

"*Accurate Measurement of Enhancement Factor in Tip-enhanced Raman Spectroscopy through Elimination of Far-field Artefacts*" **N. Kumar**, A. Rae and D. Roy, *Appl. Phys. Lett.,* 2014, 104, 123106

"*Tip-enhanced Raman Spectroscopy – An Interlaboratory Reproducibility and Comparison Study*" C. Blum, L. Opilik, J. M. Atkin, K. Braun, S. B. Kämmer, V. Kravtsov, **N. Kumar**, S. Lemeshko, J. F. Li K. Luszcz, T. Maleki, A. J. Meixner, S. Minne, M. B. Raschke, B. Ren, J. Rogalski, D. Roy, B. Stephanidis, X. Wang, D. Zhang, J. H. Zhong and R. Zenobi, *J. Raman Spectrosc.,* 2014, 45, 22-31

"*Nanoscale Spectroscopy: An Emerging Tool for the Characterisation of 2D Materials*" A. J. Pollard, **N. Kumar**, A. Rae, S. Mignuzzi, W. Su, D. Roy, *J. Mater. Nanosci*., 2014, 1, 39-49

Oral Presentations on the Topics Covered in this PhD Thesis

N. Kumar, W. Su, M. Veselý, B. M. Weckhuysen, A. J. Pollard, A. J. Wain "*Nanoscale Chemical Imaging of Solid-liquid Interfaces using Tip-enhanced Raman Spectroscopy*", The 26th International Conference on Raman Spectroscopy, Jeju, Korea, August 2018

N. Kumar, A. Wain, C. S. Wondergem, S. Kalirai, B. M. Weckhuysen "*Application of Tip-enhanced Optical Spectroscopy in Nanoscale Characterisation of Catalytic Activity*", 13th European Congress on Catalysis, Florence, Italy, August 2017

N. Kumar, A. Wain, C. S. Wondergem, S. Kalirai, B. M. Weckhuysen "*Nanoscale Mapping of Catalytic Activity using Tip-enhanced Raman Spectroscopy*", North American Catalysis Society Meeting, Denver, USA, June 2017

N. Kumar, S. Kalirai, B. M. Weckhuysen, A. J. Wain "*Nanoscale Mapping of Activity in Heterogeneous Catalysts using Tip-enhanced Optical Spectroscopy*", UK Catalysis Conference, Manchester, January 2017 – **Keynote Presentation**

N. Kumar, S. J. Spencer, D. Imbraguglio, A. Rossi, A. J. Wain, B. M. Weckhuysen, D. Roy *"Extending the plasmonic lifetime of tip-enhanced Raman spectroscopy probes"*, The 25th International Conference on Raman Spectroscopy, Fortaleza, Brazil, August 2016

N. Kumar, B. Stephanidis, R. Zenobi, A. J. Wain, D. Roy *"Nanoscale Mapping of Catalytic Activity Using Tip-enhanced Raman Spectroscopy"*, 5th International Conference on Tip-Enhanced Raman Spectroscopy, Osaka, Japan, October 2015

Other Oral Presentations

N. Kumar "*Molecular Mapping beyond Diffraction Limit using Tip-enhanced Raman Spectroscopy*", Raman Workshop, ETH Zurich, Switzerland, June 2018 – **Invited talk**

N. Kumar, A. Zoladek-Lemanczyk, F. A. Castro *"Simultaneous Topographical, Chemical and Electrical Surface Imaging at the Nanoscale"*, European Material Research Society Spring Meeting, Strasbourg, France, May 2017

N. Kumar, A. Rae, D. Roy *"Accurate Measurement of the Enhancement Factor in Tip-enhanced Raman Spectroscopy"*, The 24th International conference on Raman spectroscopy, Jena, Germany, August 2014

Acknowledgements

I must begin by thanking my PhD advisor, Professor **Bert Weckhuysen**, for giving me the opportunity to pursue my PhD research in his group. Thank you for having faith in me that even after being based mostly off-campus, I would be able to carry out cutting edge scientific research under your supervision. I have learnt so much in all my interactions with you. Perhaps most importantly that science is not just a profession, it's a way of life; it's not just about experiments and data, it's about the joy and passion of exploring innovative ideas, finding creative solutions to interesting problems and discovering new things. Our catch-up meetings were most inspiring for me and I almost always came out of them with a sense of excitement and enthusiasm. I am going to use your advice on both scientific and non-scientific matters for the rest of my professional career.

I want to thank the students, post-docs and support staff of the Inorganic Chemistry and Catalysis group at Utrecht University, who made my PhD experience most memorable. In particular, I have to acknowledge **Katinka Wondergem** for her cheerful company in the labs at Utrecht, for her thoroughness in the scientific experiments and discussions, for her great help with the data analysis, manuscript writing (Chapter 4) and the Dutch translation of my thesis summary. **Sam Kalirai**, for his enthusiasm for the FCC work, promptly sending samples to me, for exciting scientific discussions and help with the data analysis and manuscript writing (Chapter 5). **Martin Veselý**, for his great help with the data analysis (Chapter 3), **Özgun Attila**, for some memorable evenings and for paying for my lunches at Utrecht and for great scientific discussions. **Thomas Hartman**, for giving me a taste of some fine Dutch beverages and cuisine and for exploring different scientific ideas with me. They may not have always worked out but it was most fun to try. **Zoran Ristanovic**, **Joel Schmidt** and **Donglong Fu** for insightful discussions, scientific or otherwise.

At NPL, I want to thank my colleagues in the Surface and Nanoanalysis and Electrochemistry groups for their enthusiastic support both in and out of the lab over the years. In particular, I must thank **Debdulal Roy** for giving me the opportunity to work in his team, for sharing his TERS experience and knowledge with me and for valuable guidance and mentorship in the early stages of my scientific career. **Andy Wain**, for the enthusiastic and insightful scientific discussions during the course of several exciting projects, supporting for my research ideas and for demonstrating how to express complex scientific ideas most clearly and succinctly. **Fernando Castro**, for great collaboration in TERS research, for insightful scientific discussions and a refreshing sense of humour. **Andy Pollard**, for supporting my research work

at NPL, for insightful scientific discussions and for all the great evenings in the pub. **Alex Shard**, for insightful scientific discussions. My managers **Helen Sharman**, **Alice Harling, Rob Reid** and **James Hendry** for their great support for my research work, for letting me explore new ideas and for always supporting my professional development.

I must also thank my friends and colleagues, past and present, **Steve Spencer, Elizabeth Legge, David Cant, Natalie Belsey, Dimitrios Tsikritsis, Ali Rae, Sandro Mignuzzi, Kwasi Kwakwa, Tara Salter, Rasmus Havelund, Barry Brennan, Ian Gilmore, Jean-Luc Vorng, Mariavitalia Tiddia, Seb Wood, James Blakesley, Alina Zoladek-Lemanczyk, Srinath Rajagopal, Neelam Kumarswami, Arun Asokan, Soraya Caixeiro, Jianding Zhu, Tiantian Bai, Daniela Santos** and **Ameer Shaikh** who have shared their enthusiasm for science/life with me and supported me and my work both inside and/or outside NPL over the years.

I must thank **Weitao Su** for a great friendship and scientific collaboration over the years. Your passion for science has been most inspiring to me.

Thanks to my sister, **Richa Sharma** and my brother, **Rakesh Kumar Gautam** for their love, support and faith in me.

Don't think I can thank my partner, **Jiaqi Song** enough for her boundless love, patience, positivity and exuberance, for always believing in me and for putting up with all the late evenings and weekends spent in the lab. You have been the biggest pillar of support in my life for the last 7 years.

And finally, my thanks to my late mother**, Bala Devi** and my father, **Karan Singh** for their unconditional love, for always supporting my choices, for letting me explore the world, for their unshakable faith in me and for being the icons of hard work, cheerfulness, morality and spirituality for me – to whom I dedicate this PhD Thesis.

Curriculum Vitae

Naresh Kumar was born on the 20th of December 1982 in Panipat, Haryana, India. After completing his senior secondary education at Sainik School Kunjpura, Karnal, he obtained a Bachelor of Science (BSc) in Economics with 1st class honours from London School of Economics in 2007. For his academic achievement, he was conferred the Award of Academic Excellence from University of London in 2005. Naresh enrolled for a second undergraduate degree in Bachelor of Technology (BTech) in Engineering Physics at Indian Institute of Technology Delhi and graduated with a Bachelor's thesis entitled, "Deposition and Characterisation of Silver Nanoparticles on Patterned Silicon/Glass Substrates", under the supervision of Prof. J. P. Singh in 2010. During his undergraduate degree, Naresh worked as a guest researcher at University of Muenster, Germany in 2008 and 2009 and carried out molecular dynamics study of the interaction of organic molecules with supported lipid membranes under the supervision of Dr. Michael Hirtz and Prof. Lifeng F. Chi. Naresh enrolled at King's College London for his Master of Research (MRes) degree in Physics at the Nanoscale and graduated in 2011 with a mark of distinction and a Master's thesis entitled, "Nanoscale Chemical Characterisation of Polymer-blends using Tip-enhanced Raman Spectroscopy" under the supervision of Dr. Debdulal Roy and Prof. David Richards.

Naresh joined the National Physical Laboratory (NPL), UK as a Research Scientist in 2011 and has worked on the development and applications of tip-enhanced Raman spectroscopy (TERS) since then. During this time, he set up an AFM-TERS system at NPL and worked on a range of inter-disciplinary projects utilising TERS to solve problems in different areas of scientific research including heterogeneous catalysis, organic solar cells, polymer blends, small molecules within biological cells, nanoscale chemical imaging of solid-liquid interfaces and 2D materials such as graphene and single-layer MoS_2. He also carried out underpinning metrology research to improve reproducibility of the TERS measurements, extend plasmonic enhancement, lifetime, robustness and chemical inertness of TERS probes and developed a methodology to measure the plasmonic signal enhancement of TERS probes more accurately. For his professional achievements, Naresh was awarded the Rayleigh Early Career Award by NPL in 2016 and promoted to Higher Research Scientist in 2017. Naresh was admitted as a member of the Institute of Physics (MInstP) and the Royal Society of Chemistry (MRSC) and awarded the Chartered Physicist (CPhys) status in 2017.

Naresh joined the group of Inorganic Chemistry and Catalysis, Utrecht University, The Netherlands as a PhD candidate in April 2015 and began his PhD

project entitled, “Development of Tip-enhanced Raman spectroscopy and its Application to Heterogeneous Catalysis Research” under the supervision of Prof. dr. ir. Bert M. Weckhuysen. The key results of this project are described in this PhD thesis and were published as peer-reviewed articles in scientific journals and presented as oral contributions at international scientific conferences.